

TRANSPORT OVER A BUBBLE MATTRESS

the influence of interface geometry on effective slip and mass transport

Master thesis

in partial fulfilment of the
requirements for the degree of
Master of Science in Chemical Engineering

A.S. (Sander) Haase

May 16, 2012

Soft matter, Fluidics and Interfaces

Faculty of Science and Technology

University of Twente

7500 AE Enschede

The Netherlands



UNIVERSITY OF TWENTE.

Keywords: effective slip length, bubble mattress, bubble surface, gas/liquid interface, geometry, interfacial mass transfer enhancement, micro-particle image velocimetry (μ PIV)

Graduation committee

Prof. dr. ir. R.G.H. (Rob) Lammertink	Chairman (Soft matter, Fluidics and Interfaces)
Dr. C. (Chao) Sun	External member (Physics of Fluids)
Dr. P.A. (Peichun Amy) Tsai	Member (Soft matter, Fluidics and Interfaces)
E. (Elif) Karatay MSc	Mentor (Soft matter, Fluidics and Interfaces)

This work has been performed at

Soft matter, Fluidics and Interfaces
Faculty of Science and Technology
University of Twente
P.O. Box 217
7500 AE Enschede
The Netherlands

TABLE OF CONTENTS

NOTATION	V
1 INTRODUCTION	1
1.1 Background	1
1.2 Objective.....	5
1.3 Current study	6
1.3.1 <i>Bubble mattress in a chip</i>	6
1.3.2 <i>Numerical study</i>	7
1.3.3 <i>Micro-PIV</i>	8
1.4 Content of report	10
2 METHOD OF RESEARCH	11
2.1 Mathematical model.....	11
2.1.1 <i>Governing equations</i>	11
2.1.2 <i>Boundary/inlet conditions</i>	12
2.1.3 <i>Effective slip length</i>	14
2.1.4 <i>Mass transport enhancement</i>	16
2.2 Numerical approach.....	17
2.2.1 <i>COMSOL Multiphysics</i>	17
2.2.2 <i>Geometry and meshing</i>	18
2.2.3 <i>COMSOL model</i>	18
2.2.4 <i>Solver configuration and convergence</i>	19
2.3 Experimental approach	19
2.3.1 <i>Chip fabrication</i>	19
2.3.2 <i>Hydrophobisation</i>	20
2.3.3 <i>Micro-PIV</i>	21
3 NUMERICS – RESULTS AND DISCUSSION	27
3.1 Introduction.....	27
3.2 Model development.....	29
3.2.1 <i>COMSOL models</i>	29
3.2.2 <i>Geometry considerations</i>	30
3.3 Protrusion angle.....	30

3.4	Pressure gradient	31
3.5	Surface porosity	32
3.5.1	<i>Slip length</i>	32
3.5.2	<i>Mass transfer enhancement</i>	34
4	EXPERIMENTAL – RESULTS AND DISCUSSION	41
4.1	Introduction	41
4.2	Bubble mattress	41
4.3	Raw images	42
4.4	Image pre-processing	43
4.5	Correlation.....	44
4.6	Vector fields	47
4.7	Slip length calculation	50
4.8	Effective slip length	53
5	CONCLUSIONS	57
6	RECOMMENDATIONS	59
6.1	Numerical.....	59
6.2	Experimental	59
6.3	Future applications.....	60
7	REFERENCES.....	61
	ACKNOWLEDGEMENTS.....	65
A	DERIVATION OF SLIP LENGTH EQUATIONS.....	67
A.1	From average shear rate	67
A.2	From fluid flux.....	67
B	COMSOL MODEL	71
B.1	Parameterisation of bubble surface	71
B.2	Entrance/outlet domain length.....	72
C	SUPPORTING NUMERICAL DATA	73
C.1	Meshing.....	73
C.2	Model development.....	74
C.3	Concentration and velocity profiles	75
C.4	Surface porosity	76
D	ERROR ANALYSIS.....	77
E	SUPPORTING EXPERIMENTAL DATA	79

NOTATION

Symbol	Unit	Description	Equation
<i>Latin symbols</i>			
A, B, C	–	Coefficients of second-order polynomial	(41)
A_I^{ImD}	m^2	Area of interrogation domain in image domain	
b	m	Slip length	(1)
b^*	–	Dimensionless (effective) slip length	(2)
$\langle c \rangle$	$mol\ m^{-3}$	Flow-averaged outlet concentration	(33)
C_p	m^{-3}	Number of particles per unit volume	
Ca	–	Capillary number	(43)
d_p	m	Particle diameter	
D	$m^2\ s^{-1}$	Diffusion coefficient	
D	m	Channel depth	
E^ψ	–	Solute flux enhancement	(34)
E^c	–	Flow-averaged outlet concentration enhancement	(35)
$f_\infty^\#$	–	Infinity-corrected aperture number	(10)
h	m	Height of calculation line	
H	m	Height of liquid channel	
I	–	Dimensionless intensity function	
K	$m^{-1}\ s^{-1}$	Pressure gradient divided by viscosity	
L	m	Bubble unit length	
L_g	m	Side channel width	
L_s	m	Solid wall width	
m, n	m	Displacement in interrogation domain	
M	–	Image/objective magnification	
n_0	–	Index of refraction	
N	–	Number of bubble units	
N_{IP}	–	Number of image pairs	
N_I	–	Particle image density	(11)

N_{el}	–	Effective particle image density	(12)
NA	–	Numerical aperture	
P	Pa	Pressure	
Pe	–	Péclet number	(44)
Q_c	m	Cross-correlation function	(45)
R	m	Radius	
R, S	–	Coefficients of first-order polynomial	(39)
R_c	m	Average correlation function	(46)
Re	–	Reynolds number	
s	–	Standard deviation	
t	s	Time	
u	m s^{-1}	Liquid velocity in x -direction	
v	m s^{-1}	Liquid velocity in y -direction	
V_{fr}	–	Volume fraction	
W	–	Ratio of solid wall length to gas channel width	(5)
y_H	m	y -coordinate of slip wall	

Greek symbols

γ	s^{-1}	Shear rate	
δ_{pix}	m	Pixel size	
δz_c	m	Correlation depth	(9)
δz_f	m	Focal depth	
ΔP	–	Laplace pressure	(7)
ε	–	Wall porosity	(4), (6)
ϑ_{PR}	°	Protrusion angle	
λ	m	Wavelength	
μ	Pa s	Dynamic fluid viscosity	
ρ	kg m^{-3}	Fluid density	
σ	N m^{-1}	Surface tension	
ϕ	$\text{m}^3 \text{m}^{-2} \text{s}^{-1}$	Fluid flux	(32)
ψ	$\text{mol m}^{-2} \text{s}^{-1}$	Solute flux	(31)

1 INTRODUCTION

1.1 Background

For macroscopic flow systems, the assumption of a no-slip boundary for viscous fluids flowing along a solid wall has been proven to be highly accurate, and hence the no-slip boundary condition (BC) is commonly used [1-3]. It is only recently that controlled experiments in the (sub)micrometre range have demonstrated that the no-slip BC may not be entirely valid anymore for a Newtonian fluid flowing over a solid surfaces [3, 4].

Because of their small dimensions, often large pressure drops are encountered in micro- and nanofluidic devices. For a fluid flowing in a device with cross-sectional scale a , the pressure gradient ∇P scales with $1/a^4$ [4]. Maintaining the same flow rate with decreasing length scales therefore requires a sharp increase in ∇P . As a result, enhanced slippage is considered to be highly beneficial for delivering liquids through narrow microfluidic channels [4-6]. Hence there exists a growing interest in slip flow, and in the characterisation of wall slip for various surfaces in micro- and nanofluidic devices [7].

Slippage is characterised by a slip length b , and the classical definition of slip goes back to 1823 when Navier, and later also proposed by Maxwell, introduced the linear boundary condition: the component of the fluid velocity tangent to the surface is proportional to the shear rate at the surface. For a pure shear flow, the slip length b can be interpreted as the fictitious distance below the surface where the liquid velocity equals zero, i.e. where the no-slip boundary condition (BC) is valid again [3, 4]. This is schematically shown in Figure 1.1.

In a 2-dimensional system, where y is the axis perpendicular to the slip surface, u is the bulk liquid velocity, and u_s is the liquid velocity at slip surface, the slip length b is generally given by the following expression [5, 8-10]:

$$u_s = b \left. \frac{\partial u}{\partial y} \right|_{y=0} \quad (1)$$

Three types of slip flow can be distinguished [3]:

1. molecular or intrinsic slip: liquid molecules slip against solid molecules (Figure 1.1A);
2. apparent slip: e.g. a liquid flowing over a lubricating gas layer on which the liquid slips, while on the solid wall underneath the gas layer the no-slip BC is valid (Figure 1.1B);
3. effective slip: this type of slip is obtained by averaging molecular or apparent slip over a certain length scale (often for flow over complex and heterogeneous surfaces such as bubble mattresses).

On normal hydrophobic surfaces, intrinsic slip lengths are in the order of 20 nm to about 1 μm [3, 5, 7]. However, measured (apparent or effective) slip lengths on micro-patterned hydrophobic substrates are in the range from $10^0 - 10^2 \mu\text{m}$ [5].

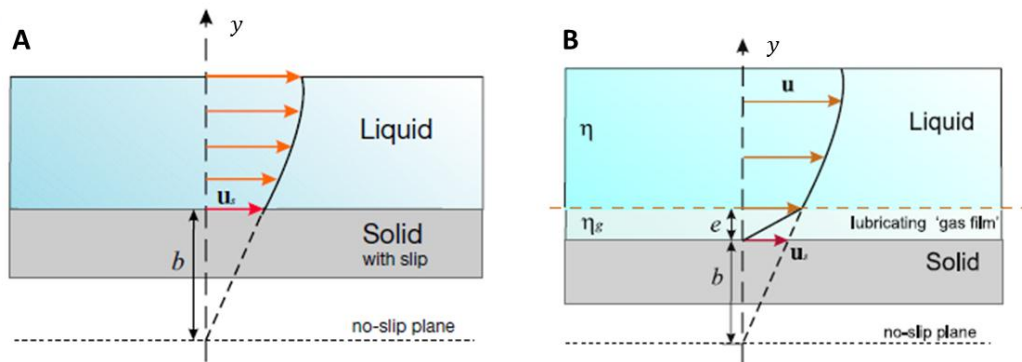


Figure 1.1 Schematic drawing a parabolic velocity profile for fluid flow along a slip wall with intrinsic slip (A) and apparent slip (B). The slip length b can be calculated from the slip velocity u_s and the velocity gradient or shear rate $\partial u/\partial y$ at the wall [3].

Various techniques have been used to measure slip experimentally [8, 11]. Choi *et al.* [1] obtain slip lengths by correlating the applied pressure gradients to the final flow rates through both hydrophilic and hydrophobic channels. Steinberger *et al.* [12] used a dynamic surface force apparatus to investigate effective slippage on superhydrophobic surfaces with a square lattice of cylindrical holes. Tretheway and Meinhart [2] have used micro-particle image velocimetry (μ PIV) to measure fluid slip for water flowing through hydrophilic and hydrophobic microchannels. μ PIV is also used by Ou and Rothstein [13], and by Tsai *et al.* [14] to investigate slip flow over a micro-patterned surface exhibiting partial slip conditions. Choi and Kim [7] obtained slip lengths for nano-engineered superhydrophobic surfaces by torque measurements utilising a rheometer.

Wall slippage can be increased significantly by micro-structuring or -patterning of the surface with the introduction of posts, grooves (transverse, longitudinal, oblique), and cavities [4, 5, 9, 14]. As gas is entrapped in these structures, the liquid is in contact with a mixed solid/gas interface characterised by partial slip conditions. Another way of reducing friction in micro-channels is by exploiting structured superhydrophobic surfaces [4, 9, 15]. There, the surface transitions from a Wenzel state, where the fluid fills the grooves, to a Cassie state, where the liquid cannot enter the grooves, and thus rests partly on the solid and partly on the gas [4, 10]. Being in the Cassie state, the gas phase in the grooves may form a lubricating layer on which the liquid flows. Such phenomena can occur at both the nanometre and micrometre scale. Such surfaces, characterised by an alternating gas/solid wall pattern, are often referred to as bubble mattresses.

In particular for these bubble mattresses, although also for other micro-structured surfaces, effective slippage has been investigated in numerous numerical studies [5, 9, 12, 13, 15] using modelling techniques like lattice Boltzmann, finite elements, and computational fluid dynamics. In the numerical studies reported here only Couette flow is considered, in which the upper boundary is moving relative the lower boundary (the bubble mattress), resulting in a linear velocity profile. Such linear flow profiles facilitate the evaluation of slip lengths, following the definition given in equation (1).

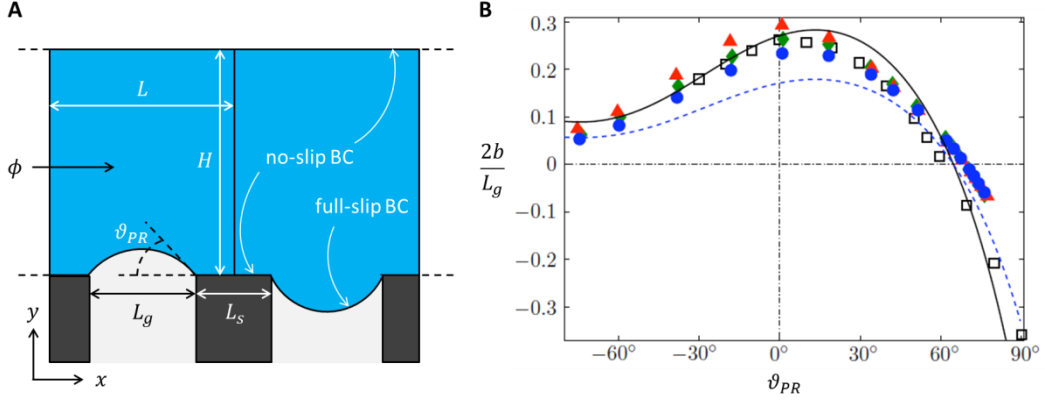


Figure 1.2 In (A) a schematic drawing of a bubble mattress is given: a fluid is flowing over a collection of bubbles. The bubble mattress is characterised by the bubble protrusion angle ϑ_{PR} , the side channel width L_g , and the surface porosity $\epsilon = L_g/L$. The graph in (B) shows the dependency of the dimensionless slip length on the protrusion angle. The data points are obtained from various numerical studies. The solid and dashed lines are calculated for a surface porosity of respectively $\epsilon = 0.68$ and $\epsilon = 0.43$. (B) is copied from [4].

Several analytical correlations have been derived that give the effective slip length as function of the slip surface geometry [4, 16-18]. According to these correlations, the slip generated by structured surfaces is a geometrical property, and does not depend on process conditions like fluid velocity, pressure gradient and fluid viscosity.

It has been shown that the exact position of the gas/liquid interface is an important factor in the final slip characteristics [4, 5, 9, 15]. Bubble mattress-like geometries (see Figure 1.2A) having moderate bubble protrusion angles ϑ_{PR} show a reduction in friction. However, when the gas bubbles are protruding very deep into in the liquid, flow lines are distorted and hence effective wall slip is reduced. Even negative slip lengths have been reported for high bubble protrusion angles [4, 9, 12].

Davis and Lauga theoretically studied two-dimensional shear flow over an array of rigid bubbles as schematically shown in Figure 1.2A [4]. For this type of bubble mattresses, they derived an analytical expression for the dimensionless slip length $2b/L_g$ as function of the surface porosity $\epsilon = L_g/L$, and the bubble protrusion angle ϑ_{PR} (for the definitions see Figure 1.2A):

$$\frac{2b}{L_g} = \pi \left(\frac{L_g}{L} \right) \int_0^\infty A(s) ds \quad (2)$$

$$A(s) = \frac{s}{\sinh 2s(\pi - \vartheta_{PR}) + s \sinh 2\vartheta_{PR}} \times \left[\cos 2\vartheta_{PR} + \frac{s \sinh 2\vartheta_{PR} \cosh s\pi + \sinh s(\pi - 2\vartheta_{PR})}{\sinh s\pi} \right] \quad (3)$$

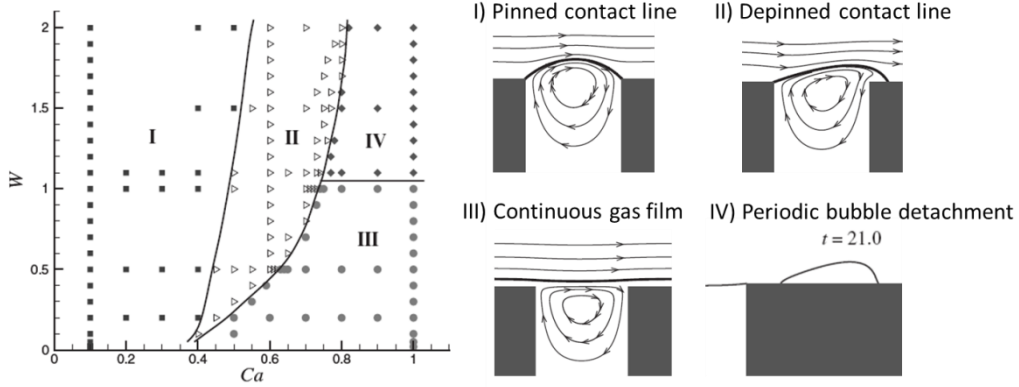


Figure 1.3 The 4 flow regimes as defined by Gao and Feng [5]. The capillary number is the ratio of the viscous forces exerted by the flowing fluid and of the surfaces forces caused by the bubble surface tension: $Ca = \mu L_g \dot{\gamma} / \sigma$.

Slip lengths calculated using this expression have proven to be in good agreement with the results of previously published 3-dimensional numerical simulations [4]. This analytical model is valid in the dilute limit, i.e. when the surface coverage by bubbles is small. It gives good quantitative predictions up to $\varepsilon \approx 0.35$, although even for very large porosities the predictions are qualitatively correct [19]. For $\varepsilon > 0.35$, the Davis-model underestimates the effective slip for bubble mattresses [19].

Evaluation of the dimensionless slip length $2b/L_g$ for various bubble protrusion angles ϑ_{PR} results in a slip length profile as shown in Figure 1.2B. The profile shows that slip only becomes negative beyond a critical protrusion angle of approximately 65° . For all protrusion angles smaller than 65° , friction towards fluid flow is reduced. The slip length profile in Figure 1.2B also shows that the dependency of effective slip on protrusion angle is much stronger for convex bubbles ($\vartheta_{PR} > 0^\circ$) than for concave bubbles ($\vartheta_{PR} < 0^\circ$).

Finally, as equation (2) shows, for a given protrusion angle ϑ_{PR} the dimensionless slip length $2b/L_g$ is proportional to the surface porosity ε :

$$\varepsilon = \frac{L_g}{L} \quad (4)$$

This implies that intrinsic or porosity-corrected dimensionless slip length profiles are constant. Furthermore, this means that profiles for bubble mattresses with different porosities cross each other in the point where $b = 0$, i.e. at the critical protrusion angle ϑ_C . This is indeed observed for the profiles shown in Figure 1.2B.

Obviously, the assumption of a rigid, spherical bubble surface is not always valid. The geometry of the bubble surface also depends on the shear rate at the gas/liquid interface. Gao and Feng [5] defined 4 different flow regimes, shown in Figure 1.3, each characterised by a certain gas/liquid interface geometry.

In regime I, the gas/liquid contact line is pinning on the sharp corners of the solid. Only for relatively high shear flows, depinning of the contact line will occur. In regime II, the contact line depins downstream of the bubble and moves further downstream. For even higher shear

rates, either the depinned bubble merges with the next gas bubble, resulting in a continuous gas film, or the gas film becomes unstable and a time-periodic bubble flow is observed. This depends on the surface porosity ε and the capillary number $Ca = \mu L_g \gamma / \sigma$. When going from regime I to III, the effective slip length increases by about one order of magnitude. For regime IV, this increase is approximately a factor 3. Presently, no experimental data or observations exist on how the interfacial morphology affects the apparent slip for the various flow regimes.

Next to reduced pressure gradients or increased flow rates, another benefit of slip flow can be a significant enhancement of interfacially driven transport phenomena, even for slip lengths in the order of nanometres [20]. In a recent commentary, the further quantification of the impact of surfaces exhibiting slip properties on surface and bulk transport phenomena is identified as an opportunity in this field [21]. And although there are already some publications on the influence of a surfaces with interfacial slip characteristics on e.g. electro-osmotic flows [22], thin film evaporation phenomena in rectangular channels [23], or thermal transport in a constant temperature channel with perpendicular alternating micro-ribs and cavities [24], to the best of our knowledge there exist no systematic studies after the influence of the exact interface geometry on transport phenomena for fluid flow over bubble mattress-like geometries.

1.2 Objective

The research described in this thesis is motivated by the following observations:

- the lack of any experimental data regarding the dependency of effective slip on the interface geometry, i.e. bubble protrusion angle, for bubble mattress-like geometries;
- the fact that the vast majority of the numerical studies published so far concern only Couette flow, while in practice primarily parabolic velocity profiles are encountered;
- that, to our knowledge, mass transport across bubble mattress-like geometries has not been investigated before, neither numerically nor experimentally.

Based on these issues, the aim of this study has been formulated. The objective is

to investigate the influence of bubble mattress interface geometry on both momentum and mass transport by quantification of effective slip length and mass transport enhancement.

This study is conducted by approaching the research question in two manners:

- numerically using COMSOL Multiphysics;
- experimentally using micro-particle image velocimetry.

In the numerical part of this study, the slip and mass transfer characteristics for transport over a bubble mattress are investigated. The numerical model used in the simulations is designed such, that it resembles the microfluidic devices that are used in the experiments. In the experimental part of this study, the velocity fields have been determined for various interface geometries, which are subsequently used to compute the effective slip lengths. The experimental results are compared with the slip length profiles obtained from numerical simulations.

1.3 Current study

1.3.1 Bubble mattress in a chip

To investigate the fluid slip characteristics along bubble mattresses experimentally, microfluidic devices have been designed and fabricated that enable the formation of an alternating gas/liquid and liquid/solid interface, i.e. a bubble mattress (see Figure 1.4A and C). These devices are made from silicon wafers. After finishing the etching of the micro-channels, the open channels are confined by an unstructured sheet of glass. Multiple silicon chips have been fabricated, characterised by different channel heights H and solid wall to side channel width ratios W (see Figure 1.4B). W is defined as:

$$W = \frac{L_s}{L_g} \quad (5)$$

The ratio W is directly related to the surface porosity ε , as the following equations shows:

$$\varepsilon = \frac{1}{1 + W} \quad (6)$$

In the fabricated silicon chips, gas and liquid phase are contacted by flowing a liquid through the upper main channel, while a gas is supplied to the lower main channel, which is connected via side channels to the upper channel (Figure 1.4A and C). By careful balancing of gas and liquid pressure, a stable bubble mattress can be established in the chip (Figure 1.4B).

Untreated silicon surfaces are wetted by most liquids, as they are high-energy surfaces having a surface tension σ of about 150 mN/m [25]. This implies that water ($\sigma = 72$ mN/m), which is used in the experiments, will fully wet the channel walls. In order to prevent the filling of the side channels with water, the gas pressure has to overcome the Laplace pressure ΔP exerted by the wetting liquid [26]. This Laplace pressure is a function of the surface tension σ of the wetting liquid, the contact angle β of the wetting liquid with the solid substrate, and the radii of curvature R_1 and R_2 :

$$\Delta P = \sigma \cos \beta \left(\frac{1}{R_1} + \frac{1}{R_2} \right) \quad (7)$$

Although a bubble mattress could be obtained by balancing gas and liquid pressure, it will be unstable because of small fluctuations in gas pressure in the device. This causes immediate filling of the side channels, as wetting of untreated silicon surfaces is spontaneous ($\beta \approx 0^\circ$).

In order to have precise control over the geometry of the bubble surface, i.e. over the bubble protrusion angle ϑ_{PR} (see Figure 1.4B), and to enhance the stability of the formed bubble mattress, all microfluidic devices are hydrophobised by covalent bonding of fluorinated silane monomers to the silicon surfaces [25]. These hydrophobic molecules form a planar network, characterised by a very low surface tension. The surface becomes hydrophobic, showing large contact angles for water ($\beta > 90^\circ$). As a result, wetting of the side channels is

prevented (ΔP changes its sign, see equation (7)). This promotes the establishment of a stable bubble mattress.

1.3.2 Numerical study

COMSOL Multiphysics is utilised for numerical investigation of slip and mass transfer characteristics for transport over a bubble mattress. More specifically, the influence of bubble protrusion angle, operating conditions, and bubble mattress geometry on effective slip and mass transfer enhancement is investigated.

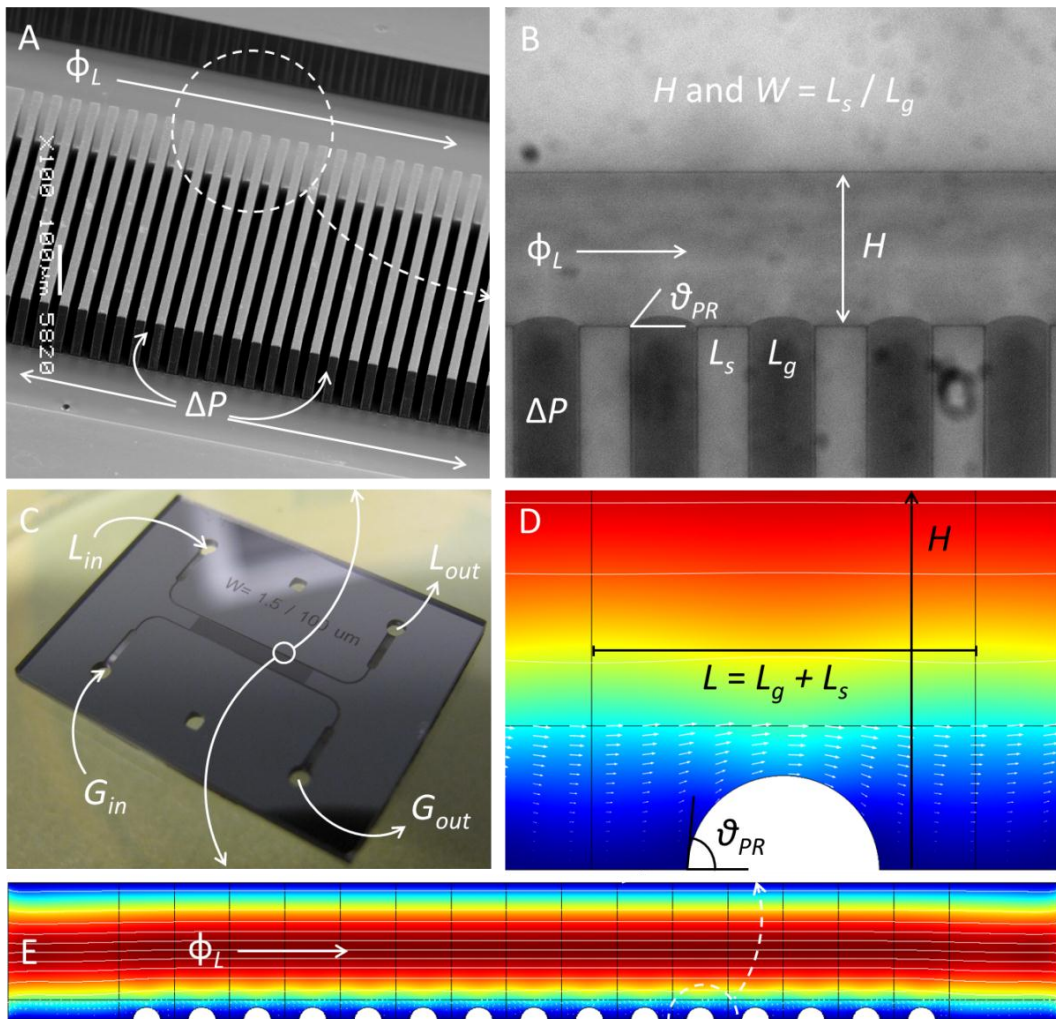


Figure 1.4 In (C), a picture of a microfluidic device is shown that is used for experimental investigation of the effective slip length for fluid flow over a bubble mattress. Gas and liquid phase are brought in contact with each other by flowing a liquid through the upper main channel, while a gas is supplied to the lower main channel, which enters the side channels (A). By balancing gas and liquid pressure, a stable bubble mattress can be formed in the chip (B). Based on the devices as shown in (C), a 2-dimensional non-periodic COMSOL model is developed having the same geometric characteristics (D and E).

As the numerical study is performed to support experimental investigations, the 2-dimensional model used in the simulations resembles the microfluidic devices that are used in the experiments (compare Figure 1.4C with Figure 1.4D and E). Accordingly, all simulations concern non-periodic pressure-driven flow. In the COMSOL model, the gas/liquid interface is assumed to be rigid ($Ca < 0.1$); i.e. fluid flow is in regime I with pinned contact lines (see Figure 1.3).

As our simulations concern parabolic velocity profiles, contrary to the linear velocity profiles in most other numerical studies, an equation has been derived that gives the effective slip length b as function of macroscopic quantities such as fluid flux and pressure gradient. As far as we know, this type of equation has not been used before in other numerical studies (experimentally it is used before [1, 6]). Commonly the slip length is obtained by calculation of the shear rate at the slip wall.

1.3.3 Micro-PIV

To investigate the slip properties of bubble mattresses experimentally, micro-particle image velocimetry (μ PIV or micro-PIV) is used. In the last decade, μ PIV has become the standard technique for quantitative measurements of fluid velocity in micro channels [27]. In this non-intrusive method, particle distributions are recorded on two or more successive images A and B, separated by a specified and suitable time delay Δt (see Figure 1.5A) [28]. These particle patterns are spatially correlated. This is utilised to calculate the average displacement of small groups of particle distributions over time by cross-correlation [27-29].

Prior to correlation, the particle images are divided in regularly spaced windows. The size of these so-called interrogation windows should be small enough to ensure the particle displacement is homogeneous, but at the same time large enough to ensure the interrogation windows contain a sufficiently high number of particles to perform the correlation [27]. By statistically comparing the particle patterns in image A and B for each interrogation window, the local (average) particle displacement $\Delta \mathbf{x}$ is obtained from the largest cross-correlation peak (see Figure 1.5A). As the time delay Δt between image A and B is known, the local velocity vector \mathbf{u} can be calculated:

$$\mathbf{u} = \frac{\Delta \mathbf{x}}{\Delta t} \quad (8)$$

Because the particle distributions are recorded in a two-dimensional plane with a finite thickness ($\sim 3 \mu\text{m}$), this ultimately results in a two-dimensional velocity field.

A schematic drawing of a typical μ PIV setup is shown in Figure 1.5B. In this inverted epi-fluorescent microscope, all optics for illumination and images are located at the bottom side of the microfluidic chip [29]. Since commonly high image magnifications $M \gg 1$ are used in μ PIV, the focal depth is much smaller than the depth of illumination. Hence it is common to illuminate the entire flow volume, for which generally a double-pulsed Nd:YAG or Nd:YLF laser is used that emits pulses of green light ($\lambda = 532 \text{ nm}$) [27-30]. To avoid over-exposure of the camera sensor, small fluorescent particles with a typical diameter d_p of $0.2 - 2 \mu\text{m}$ can be used. With appropriate optical components and sensors, only the fluorescent light of the particles is then recorded.

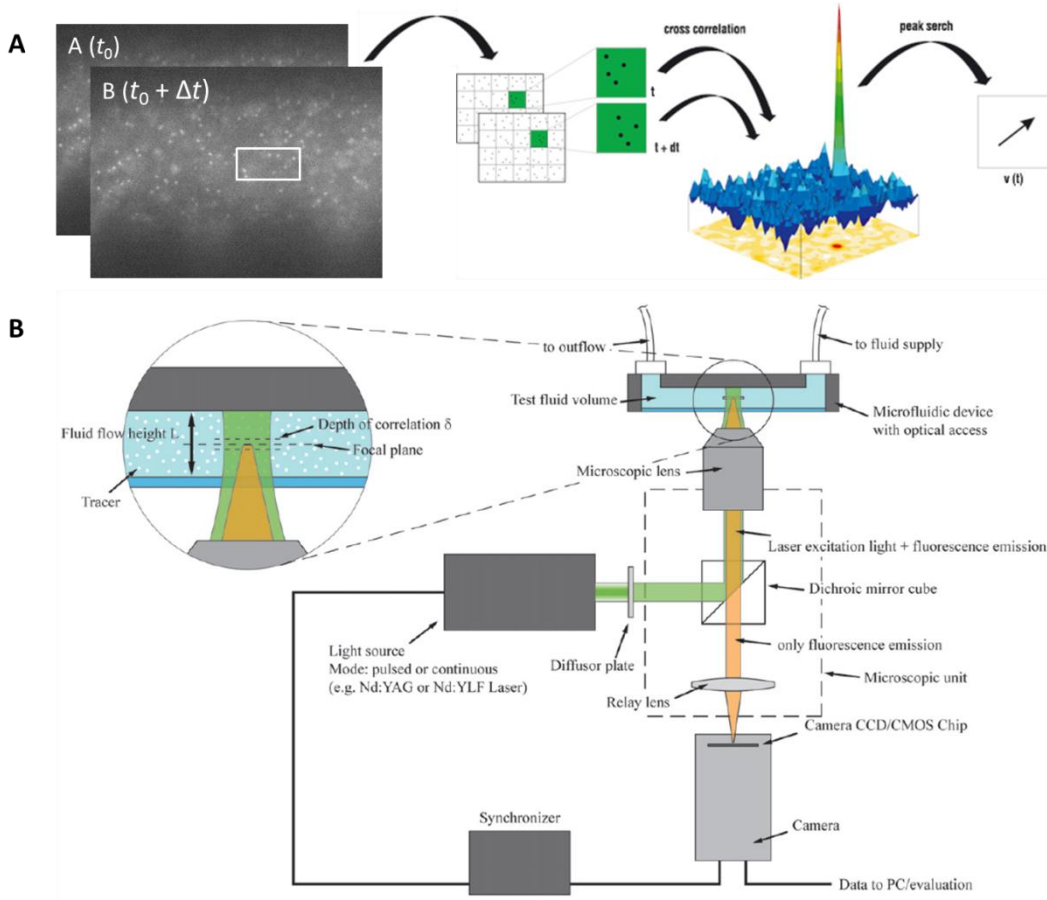


Figure 1.5 In (A) the cross-correlation of particle patterns in order to obtain the local average particle displacements is displayed (schematic taken from [31]). A schematic drawing of a typical epi-fluorescent micro-PIV setup is given in (B) (image taken from [27]).

An important parameter in μ PIV is the correlation depth δz_c , i.e. the depth over which the particles contribute to the measured particle displacements (see Figure 1.5B). The correlation depth is larger than the focal depth δz_f , as also particles slightly out of focus contribute to the correlation. δz_c can be calculated using the following equation [29, 30]:

$$\delta z_c = 2 \left[\frac{(1 - \sqrt{\varepsilon})}{\sqrt{\varepsilon}} \left(f_\infty^{\#2} d_p^2 + \frac{5.95(M + 1)^2 \lambda^2 f_\infty^{\#4}}{M^2} \right) \right]^{1/2} \quad (9)$$

ε is a specific parameter related to the correlation procedure, and M the objective magnification. $f_\infty^\#$ is the infinity-corrected aperture number of the microscope lens, as given by the following equation [28, 29]:

$$f_\infty^\# = \frac{1}{2} \left[\left(\frac{n_0}{NA} \right)^2 - 1 \right]^{1/2} \quad (10)$$

Here, n_0 is the index of refraction, and NA is the numerical aperture of the used objective.

Because of the high magnification, in μ PIV the effective image density is generally very low. The image density N_I is the mean number of particles per interrogation volume, and can be expressed as follows [29]:

$$N_I = \frac{C_p A_I^{ImD} \delta z_c}{M^2} \quad (11)$$

Here, C_p is the number of particles per unit volume, and A_I^{ImD} is the area of the interrogation window in the image domain. To avoid the problem of low image density, ensemble correlation (also referred to as correlation averaging) is commonly used to compute the particle displacements from N_{IP} image pairs [27-30], as according to the following expression, ensemble correlation increases the effective particle density N_{eI} :

$$N_{eI} = N_{IP} N_I \quad (12)$$

The increased effective image density allows reducing the size of the interrogation window, which improves the spatial resolution of the ultimate vector fields. Obviously, the flow needs to be at steady state to use ensemble correlation [28, 29].

1.4 Content of report

The method of research is described in chapter 2, which consists of three parts. The first part gives the underlying mathematical model of the numerical study. Also two methods of slip length calculation, and the three references models for calculation of mass transfer enhancement are explained. In respectively the second and third part, the numerical and experimental approach is described.

In chapter 3 the results of the numerical study are discussed. The model development is shortly described, as is the influence of the applied pressure gradient on both effective slip length and mass transfer. The effects of the precise gas/liquid interface geometry on the transport phenomena over a bubble mattress are elaborately discussed.

The μ PIV experiments, the image pre-processing, the calculation of the vector fields by multigrid ensemble correlation, and the extraction of the slip length from the vector fields are described in chapter 4. The experimentally determined effective slip lengths are discussed and compared with numerically obtained slip length profiles.

The conclusions and recommendations can be found in respectively chapter 5 and 6.

2 METHOD OF RESEARCH

2.1 Mathematical model

The influence of bubble protrusion angle, operating conditions, and bubble mattress geometry on effective slip and mass transfer is numerically investigated using computational models that resemble the microfluidic devices. It is emphasised that only the liquid flow is simulated.

In order to simulate fluid flow over and mass transport across a bubble mattress, a mathematical model is required that describes these phenomena. The Navier-Stokes equations of motion, which are based on the conservation of momentum, form the basis of the numerical model built in this study. These equations are coupled with convection-diffusion equations describing mass transport. The governing equations, described in section 2.1.1, are expressed in Cartesian coordinates. Section 2.1.2 gives the boundary conditions that used in the numerical model.

The obtained flow fields and solute concentration distributions are used to calculate respectively the effective slip length and mass transport enhancement for the geometry under consideration. The methods of computing effective slip and mass transport enhancement, which are used in both the numerical and experimental part of this study, are described in respectively section 2.1.3 and 2.1.4.

2.1.1 Governing equations

2.1.1.1 Momentum transport

The Navier-Stokes equations form the starting point for model development. In vector-form, the Navier-Stokes equation for incompressible flow and constant density can be written as follows (there are no body forces present):

$$\rho \left(\frac{\partial \mathbf{u}}{\partial t} + \mathbf{u} \cdot \nabla \mathbf{u} \right) = -\nabla P + \mu \nabla^2 \mathbf{u} \quad (13)$$

Here, ρ is the fluid density, \mathbf{u} the velocity vector, t time, P pressure, and μ fluid viscosity. For incompressible fluid flow the density is constant. The mass continuity equation now simplifies to (which is more specifically a statement that the volume is constant) [32]:

$$\rho \nabla \cdot \mathbf{u} = 0 \quad (14)$$

In this study, only 2-dimensional simulations in the xy -domain are performed. Before solving the Navier-Stokes equations, the following assumptions are made:

- the system is stationary;
- the system is isothermal, i.e. a constant liquid temperature;

- the fluid is incompressible, i.e. a constant density;
- the fluid viscosity is constant.

Now, the following Navier-Stokes equations (expressed in Cartesian coordinates) are solved:

$$\rho \left(u \frac{\partial u}{\partial x} + v \frac{\partial u}{\partial y} \right) = - \frac{\partial P}{\partial x} + \mu \left(\frac{\partial^2 u}{\partial x^2} + \frac{\partial^2 u}{\partial y^2} \right) \quad (15)$$

$$\rho \left(u \frac{\partial v}{\partial x} + v \frac{\partial v}{\partial y} \right) = - \frac{\partial P}{\partial y} + \mu \left(\frac{\partial^2 v}{\partial x^2} + \frac{\partial^2 v}{\partial y^2} \right) \quad (16)$$

The left-hand side terms of above equations describe local convection. The terms at the right-hand side are the pressure and viscous (diffusion) terms, respectively. As the flow is stationary, these equations do not contain acceleration terms.

2.1.1.2 Mass transport

Not only the wall slip characteristics, but also the effect of a bubble mattress on mass transfer is investigated in this study. The bubbles are considered to be formed by a pure gas. Some important assumptions are made:

- the system is at steady state;
- the gas phase is a pure substance, i.e. the solute concentration at the bubble surface is constant;
- gas and liquid molecules do not react with each other;
- temperatures are constant for both phases, i.e. an isothermal system;
- the liquid properties remain constant.

Transport into the liquid phase is caused by both convection and diffusion. To obtain the solute concentration profile, the following mass balance needs to be solved:

$$u \frac{\partial c}{\partial x} + v \frac{\partial c}{\partial y} = D \left(\frac{\partial^2 c}{\partial x^2} + \frac{\partial^2 c}{\partial y^2} \right) \quad (17)$$

In above equation c is the solute concentration, and D the diffusivity of the solute in the fluid.

2.1.2 Boundary/inlet conditions

The computational domain is provided in Figure 2.1. In order to solve the governing equations describing this steady state system, boundary conditions (BC) need to be defined. Numerically, fluid flow is driven by a set pressure gradient $\Delta P/\Delta x$ over the computational domain. This results in following boundary conditions for the in- and outlet:

$$P = P_0 \text{ at } x = -2L \quad (18)$$

$$P = P_1 \text{ at } x = (N + 2)L \quad (19)$$

Accordingly, P_0 is given by the following expression (for a flow in the positive x -direction, $\Delta P/\Delta x$ is negative):

$$P_0 = P_1 - (N + 4)L \frac{\Delta P}{\Delta x} \quad (20)$$

Furthermore, the viscous stress is set to 0 at both in- and outlet:

$$[\mu \nabla \mathbf{u} + (\nabla \mathbf{u})^T] \mathbf{n} = 0 \text{ at } x = -2L \text{ and } x = (N + 2)L \quad (21)$$

This ‘pressure, no viscous stress’ boundary condition is physically equivalent to ‘a boundary that is adjacent to a large container (inlets) or exiting into a large container (outlets)’ (COMSOL Multiphysics).

A no-slip BC is applied to the solid walls between the bubbles, and to the upper wall:

$$\mathbf{u} = 0 \text{ at } y = 0 \text{ (for } x \text{ coinciding } L_s) \text{ and at } y = H \quad (22)$$

The gas/liquid interface is a full fluid slip surface ($b = \infty$), meaning that there are no viscous effects on the surface (i.e. the viscosity of the gas is neglected) [3]. Now, the BC’s are (where \mathbf{I} is the 2×2 identity matrix for 2-dimensional flow):

$$\mathbf{u} \cdot \mathbf{n} = 0 \text{ at } y = 0 \text{ (for } x \text{ coinciding } L_g) \quad (23)$$

$$[-P\mathbf{I} + \mu(\nabla \mathbf{u} + (\nabla \mathbf{u})^T)] \mathbf{n} = 0 \quad (24)$$

At the inlet the solute concentration equals 0:

$$c = 0 \text{ at } x = -2L \quad (25)$$

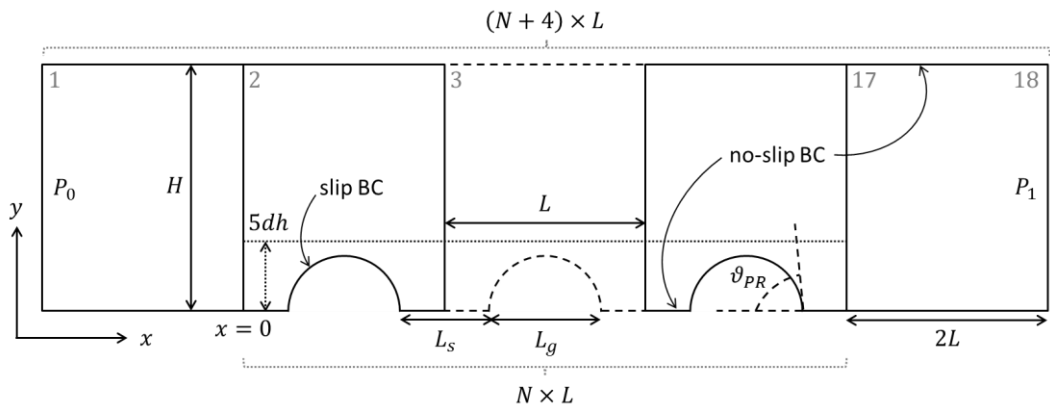


Figure 2.1 The standard non-periodic pressure-driven model as used in COMSOL Multiphysics. The pressure gradients are calculated over the middle $(N - 4)$ bubble units. Periodic models correspond to one bubble unit N .

Furthermore, the solute concentration at the bubble surface needs to be defined:

$$c = c_0 \text{ at } y = 0 \text{ (for } x \text{ coinciding } L_g) \quad (26)$$

It is assumed that the solute flux at the outlet is dominated by convective transport, which results in the following BC:

$$\mathbf{n} \cdot (-D\nabla c) = 0 \text{ at } x = (N + 2)L \quad (27)$$

Finally, there is no flux of solute through the lower wall for x coinciding L_s , and through the upper wall:

$$\frac{\partial c}{\partial y} = 0 \text{ at } y = 0 \text{ (for } x \text{ coinciding } L_s) \text{ and at } y = H \quad (28)$$

2.1.3 Effective slip length

2.1.3.1 Slip length from shear rate

b is commonly calculated from the shear rate γ in the y -direction at the upper wall. This is based on the definition of slip length as given in equation (1):

$$u_s = b \left. \frac{\partial u}{\partial y} \right|_{y=0} = b\gamma|_{y=0} \quad (1)$$

The relation between the local slip length b and the local liquid velocity u_s at the wall is also schematically shown in Figure 2.2. For bubble-mattress like geometries, the protruding bubble may complicate calculation of the shear rate at the lower wall. Hence Couette flow is often used for studies after b , because the velocity profile is linear, meaning that $\partial u/\partial y$ is approximately constant in the y -direction [1, 15]. However, for periodic velocity profiles this is not the case. Therefore, the velocity gradient is calculated at a calculation line h , where the minimum value of h is determined by the maximum protrusion depth of the bubbles. As derived in appendix A.1, the effective slip length now can be calculated as follows, where for γ and the liquid velocity u the average value over a certain calculation line is taken (standard at $y = h = 5dh$ over the middle 11 bubble units, see Figure 2.1 and Figure 2.2):

$$b = \left(\frac{\partial y}{\partial u} \right) \Big|_{y=h} - h \quad (29)$$

Note that the slip length obtained by using this method, if $h > 0$, gives an overestimation of the actual slip length, as for parabolic velocity profiles the shear rate decreases from the wall towards the middle of the channel (see Figure 2.2). However, when evaluating the shear rate and liquid velocity at the same calculation line over the whole length of mattress, it cannot be avoided that $h > 0$, because the bubble protrusion depth is always larger than 0.

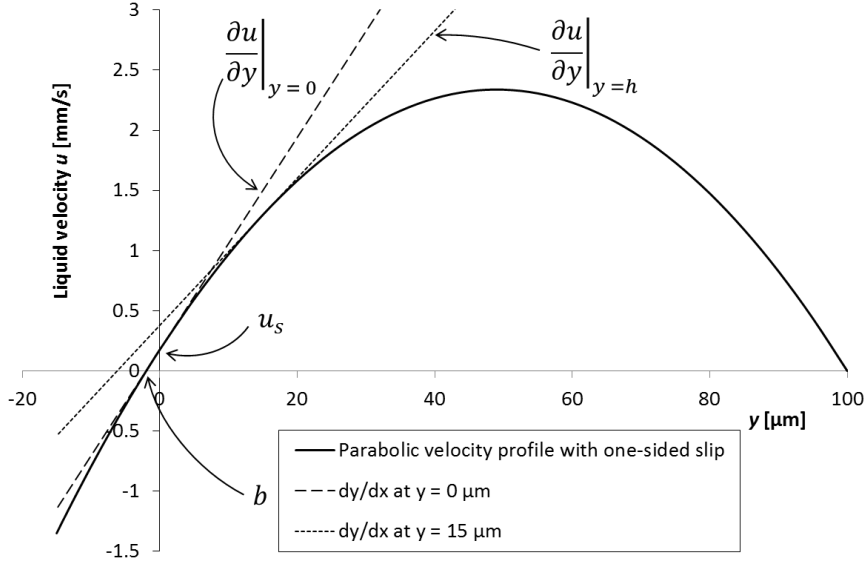


Figure 2.2 Example of a velocity profile for pressure driven flow with at $y = 0$ a full-slip BC with (here) $b = 2 \mu\text{m}$, and at $y = H$ a no-slip BC. When the shear rate is calculated at $y = h > 0$, the slip length obtained by using equation (29) is an overestimation of the actual slip length.

2.1.3.2 Slip length from fluid flux

Calculation of the slip length b from the shear rate for different bubble protrusion angles is difficult when dealing with non-linear velocity profiles, as for a proper comparison the height at which the shear rate γ is evaluated should be constant. For studies with pressure-driven flow, this line is positioned in a highly non-linear section of the velocity profile (see also Figure 2.2). This asks for another method to evaluate the effective slip length b .

For pressure-driven flow it is assumed that the flow is purely x -directional; i.e. the flow is not disturbed by the bubbles protruding in the liquid. Actually, to obtain the effective slip length, it is assumed that there is slip flow everywhere at $y = 0$. Based on these assumptions, an equation is derived that gives the velocity profile for pressure-driven flow with one-sided effective wall slip. An example of such a velocity profile is provided in Figure 2.2. Extrapolation of the velocity gradient at $y = 0$ through $u = 0$ returns the effective slip length b . In the numerical models however, the calculated profile can deviate from the one showed here, especially for higher protrusion angles.

Subsequently, assuming profiles as in Figure 2.2, an expression is derived that gives the effective slip length as function of the local pressure gradient $\partial P/\partial x$ (calculated over the middle $(N - 4)$ bubbles), the macroscopic fluid flux ϕ , and the channel height H :

$$b = \frac{-\phi - \frac{H^2}{12\mu} \frac{\partial P}{\partial x}}{\frac{\phi}{H} + \frac{H}{3\mu} \frac{\partial P}{\partial x}} \quad (30)$$

The derivations are provided in appendix A.2.

It is important to note that both calculation methods (the shear rate method and the macroscopic method) are based on the definition of the slip length as given in equation (1). The

shear rate method uses local fluid properties to obtain the slip length, while the fluid flux method uses macroscopic properties to compute the slip length.

2.1.4 Mass transport enhancement

The mass transfer characteristics for fluid flow over a bubble mattress, where a solute is transported from the gas to liquid phase, are evaluated by calculating the mass transport enhancement E with respect to the three reference models depicted in Figure 2.3 (which correspond to the numbers below).

1. Usually a constant solute concentration is assumed at a permeable wall for calculating the solute flux [33]. For systems with very small L or L_g (e.g. in membranes), this assumption holds reasonably well. However, for the bubble mattresses in this study, characterised by large L and L_g , the assumption of a constant solute concentration at the lower wall does not hold. To account for this, which is in particular important when varying the porosity, in reference 1 the solute is only present at patches with width L_g , on which a no-slip BC is applied.
2. The effect of increasing protrusion angle on mass transfer is examined by comparing the mass transfer for each ϑ_{PR} to the mass transport obtained for $\vartheta_{PR} = 0^\circ$. As such the mass transfer enhancement in reference 2 is a only result of a different protrusion angle.
3. To investigate the influence of a full-slip BC at the gas/liquid interface, the geometry for reference 3 is similar to the bubble mattress model for each protrusion angle (i.e. reference 3 varies with protrusion angle), except that the slip BC is changed into a no-slip BC. The enhancement then only originates from the wall slip at the bubble surface.

The mass transfer enhancement for a given system is commonly calculated using the solute flux at the outlet of the system. The solute flux ψ at the outlet of the bubble mattress is given by the following expression:

$$\psi = \frac{\int_0^H (uc) dy}{H} = \phi \langle c \rangle \quad (31)$$

The fluid flux ϕ and flow-averaged or mixing cup outlet solute concentration $\langle c \rangle$ are given by respectively equations (32) and (33):

$$\phi = \frac{\int_0^H u dy}{H} \quad (32)$$

$$\langle c \rangle = \frac{\int_0^H (uc) dy}{\int_0^H u dy} \quad (33)$$

The solute flux enhancement E^ψ is defined as the ratio of the solute flux at the outlet of the bubble mattress ψ_b to the solute flux in the reference model under consideration $\psi_\#$, keeping all other variables (e.g. applied pressure gradient, channel height) constant:

$$E^\psi = \frac{\psi_b}{\psi_\#} \quad (34)$$

As can be seen from equation (31), the outlet flux ψ is the product of the fluid flux ϕ and the flow-averaged or mixing-cup outlet concentration $\langle c \rangle$. To investigate mass transfer enhancement in more detail, in this study also the flow-averaged solute outlet concentration enhancement E^c is considered. E^c is defined as the ratio of the flow-averaged outlet concentration of the bubble mattress $\langle c \rangle_b$ to the flow-averaged outlet concentration in the reference model under consideration $\langle c \rangle_\#$, keeping all other variables constant:

$$E^c = \frac{\langle c \rangle_b}{\langle c \rangle_\#} \quad (35)$$

Here, # represents one of the 3 reference situations. These two definitions of mass transfer enhancement enables us to trace the major source of mass transport enhancement, being either positive or negative.

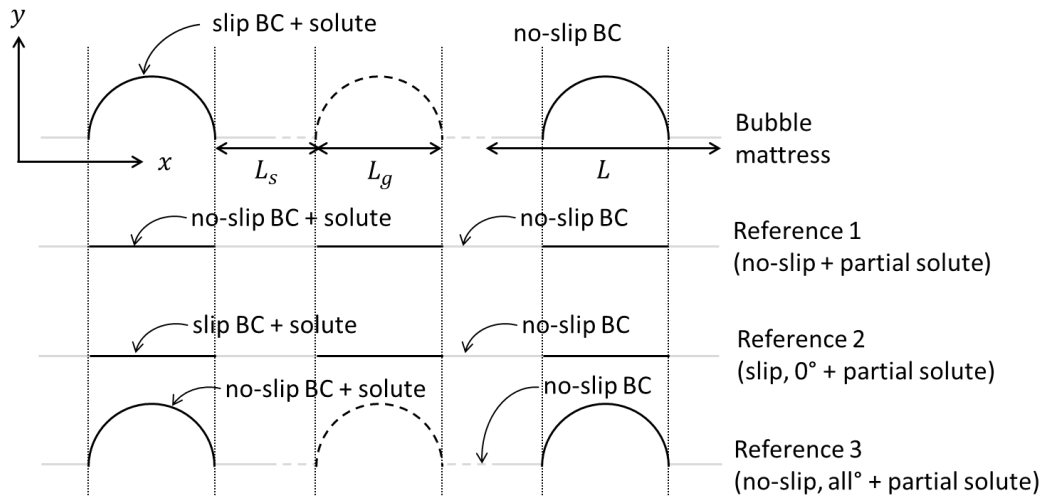


Figure 2.3 3 reference situations for determining the solute flux enhancement, determined from the flow averaged concentration calculated directly after the last bubble unit.

2.2 Numerical approach

2.2.1 COMSOL Multiphysics

For modelling fluid flow over a bubble mattress, together with mass transfer from gas to liquid phase, the finite difference software COMSOL Multiphysics (version 4.1) is employed. This commercially available software consists of various physics packages, all containing the required equations for solving the model. The packages that are used and combined in this study are the following:

- laminar flow;
- transport of diluted species.

2.2.2 Geometry and meshing

In order to facilitate the numerical validation of the effective slip length for varying protrusion angles, the rigid, perfectly spherical bubble surface geometry is parameterised. The derivation is provided in appendix B.1. The equations describing the bubble surface are functions of the geometry and protrusion angle under consideration, where equation (37) should be multiplied with -1 for negative ϑ_{PR} :

$$x = \frac{L_b}{2} + \frac{L_b}{2} \frac{\cos s}{\sin \vartheta_{PR}} \quad (36)$$

$$y = -\frac{L_b}{2} \frac{\cos \vartheta_{PR}}{\sin \vartheta_{PR}} + \frac{L_b}{2} \frac{\sin s}{\sin \vartheta_{PR}} \quad (37)$$

$$s = \left[\frac{\pi}{2} - \vartheta_{PR}, \frac{\pi}{2} + \vartheta_{PR} \right] \quad (38)$$

2.2.3 COMSOL model

The COMSOL model is a non-periodic geometry, in which fluid flow is pressure-driven (see Figure 1.4E). This model is obtained by gradual development, starting from periodic Couette flow models. Subsequently the flow type is changed to pressure-driven flow, and non-periodicity is introduced in the models. Also, the two methods of calculating the slip length as described in section 2.1.3 are compared with each other. The differences between the various models and the calculation methods are described in a previous report [34]. This thesis only describes the numerical results obtained from a non-periodic, pressure driven model with, unless otherwise indicated, the specifications listed in Table 2.1.

Meshing of the numerical models is performed automatically, where the element size is optimised for fluid dynamics. The size of the elements depend on the overall size of the model, and thus varies for e.g. $H = 50; 100; 500 \mu\text{m}$. For the latter model height, it is found that the accuracy is negatively affected by the model size. In all models, the element size is set to *extra fine* and near all boundaries to *extremely fine*. An example of a mesh is given in Figure C.1. The number of mesh elements is about 3×10^5 for a model with $H = 50 \mu\text{m}$, and about 2×10^5 for a $H = 100 \mu\text{m}$ model. For respectively a $H = 50 \mu\text{m}$ and $H = 100 \mu\text{m}$ model, the maximum element sizes are globally $6.5 \times 10^{-7} \text{ m}$ and $1.3 \times 10^{-6} \text{ m}$, and near the boundaries $6.7 \times 10^{-7} \text{ m}$ and $3.4 \times 10^{-7} \text{ m}$.

In periodic COMSOL models only a pressure difference can be used for simulating flow in a channel. For a proper comparison between periodic and non-periodic models (in the model development phase), it was therefore imperative that, instead of fixing the flow rate, also in non-periodic models a pressure difference is applied to drive the flow.

The embedded operators *aveop* and *intop* in COMSOL were utilised for respectively averaging and integration over boundaries or domains.

Table 2.1 Overview of the variables and their values in the standard COMSOL model.

Variable	Value	Comments
ρ	10^3 kg m^{-3}	
μ	10^{-3} Pa s	
L_g	$20 \text{ }\mu\text{m}$	
L	$40 \text{ }\mu\text{m}$	$L = L_g + L_s$
ϑ_{PR}	$\pm[1,9, \dots, 81,89]^\circ$	Angle increments of 8°
N	15	Obviously not valid for periodic models.
dh	$3 \text{ }\mu\text{m}$	Calculation line for shear rate-based slip at $5dh$
W	1	$W = L_s/L_g$
H	$100 \text{ }\mu\text{m}$	
$\Delta P/\Delta x$	-1800 Pa m^{-1}	For parabolic profile: $u_{av} = 1.5 \text{ mm/s}$
c	40 mol m^{-3}	Concentration of a pure gas at $\sim 1 \text{ atm}$
D	$10^{-9} \text{ m}^2 \text{ s}^{-1}$	Typical diffusivity of solute in liquid phase

2.2.4 Solver configuration and convergence

Flow fields and concentration profiles are computed sequentially in two study steps. This is possible, as the flow field is not affected by solute transport in these studies. For solving the models, the PARDISO solver is used. A parametric sweep is employed to investigate the effective slip and mass transfer enhancement for different protrusion angles ($-90^\circ < \vartheta_{PR} < 90^\circ$).

To ensure the COMSOL models are converging, the standard solver configuration is adjusted.

- The relative tolerance is set to 0.01 (standard this is 0.0001). This is a less desirable but effective step to reach a converged solution. For these studies, decreasing the relative tolerance does not affect the results significantly.
- A very fine mesh is used to reach convergence with a high relative tolerance. A finer mesh means that the computation time increases, and that more calculation steps are required for obtaining a converged solution.

2.3 Experimental approach

2.3.1 Chip fabrication

For experimental parametric investigation of the effective slip length for a bubble mattress, microfluidic devices (as shown in Figure 1.4C) with various channel dimensions and wall porosities are supplied. Micro-channels on silicon wafers were fabricated by standard photolithography techniques followed by dry ion etching. In order to obtain straight channel walls and to prevent tapering off the walls, a suitable etching recipe was selected. The via-holes for the fluidic connections were etched by dry ion etching. The fabrication is completed by anod-

ic bonding of an unstructured glass wafer to the processed silicon wafer in order to confine the micro-channels.

Available chips have main channel heights H of 50, 100, and 500 μm . The (gas-filled) side channel width L_g is kept constant at $L_g = 20 \mu\text{m}$. For each (liquid-filled) main channel height, 3 chips are available characterised by a different solid wall to side channel width ratio $W = L_s/L_g$, i.e. a different surface porosity. These ratios W are 0.5, 1, and 1.5. The etching depth of both main and side channels is 100 μm .

2.3.2 Hydrophobisation

In order to obtain a bubble mattress, i.e. stable gas/liquid interfaces, hydrophobisation of the microfluidic devices is required. The hydrophobisation protocol is based on the procedure described by Maboudian *et al.* [35]. Trichloro-(1H,1H,2H,2H-perfluorooctyl)-silane (FOTS, 97%, Sigma-Aldrich) is used as a hydrophobisation agent.

Before hydrophobising the devices, they are cleaned by immersing them in 65% HNO_3 for about 8 hours. Concentrated HNO_3 removes all organic molecules from the chip, and oxidises the silicon surface (formation of Si-OH groups). After rinsing the devices thoroughly with deionised water, devices are placed in a chip holder, and connected to e.g. syringe or pressure controller via dimethylpolysiloxane capillaries (180 μm inner diameter) and PEEK tubings (see Figure 2.5B). Whatman SPARTAN 0.2 μm RC/PP syringe filters (GE Healthcare Bio-Sciences, USA) are utilised to avoid entrance of particles or FOTS-agglomerates in the micro-channels. Finally, the chips are hydrophobised by the following protocol.

- First, the devices are flushed with subsequently deionised water, 2-propanol, and n -hexane. This sequence is necessary to ensure water is removed from the hydrophilic silicon surface as much as possible, even though water is required for the hydrophobisation (see Figure 2.4). The presence of too much water initiates polymerisation of FOTS-monomers [35-37].
- Then n -hexane is replaced with the FOTS-solution (5 mM FOTS in dried n -hexane). The solution is kept inside the devices for 25 – 30 min to let the reaction take place. Exposure of the various solutions to water should be avoided as much as possible, as water will initiate the polymerisation of FOTS. A schematic drawing of the reaction is provided in Figure 2.4 [36-38]. First, the polar Si- CCl_3 -head group of the FOTS-molecules is hydrolysed by the formation of Si-C-OH bonds. These groups are strongly attracted by the oxidised silicon surface. These hydroxyl groups condensate with both the Si-OH groups on the silicon surface and the silanol groups from other FOTS-molecules, thereby producing covalent siloxane (Si-O-Si) bonds. The speed of FOTS-monolayer formation on the silicon surface depends on the concentration, but it takes a few minutes up to several hours [35].
- Excess FOTS-solution and formed hydrochloric acid are removed by rinsing the device with subsequently n -hexane, 2-propanol, and deionised water. Finally, after predrying with nitrogen, the devices are placed in an oven at 120 $^\circ\text{C}$ for about 2 hours. Baking speeds up the formation of a covalent siloxane network by in-plane polymerisation of FOTS [35].

In hydrophobised devices, static water contact angles in the range of 80 $^\circ$ – 100 $^\circ$ are observed under a microscope.

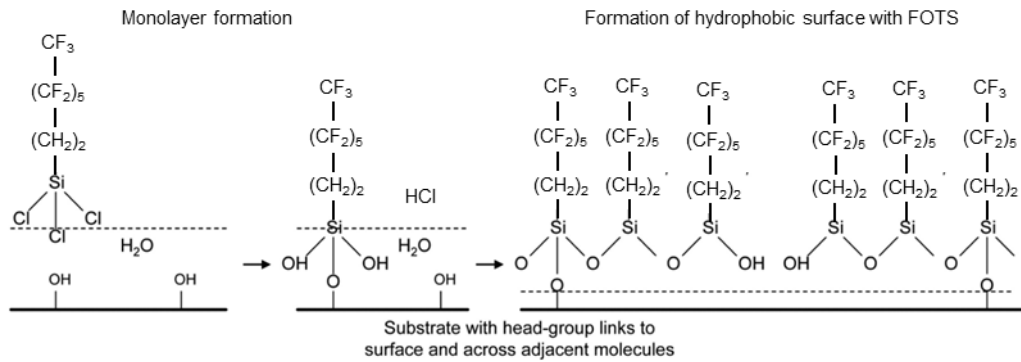


Figure 2.4 Schematic overview of the hydrophobisation of silicon microfluidic devices using FOTS. Figure adjusted from [38].

2.3.3 Micro-PIV

2.3.3.1 Setup

The experimental setup as used in the μ PIV experiments is shown in Figure 2.5. A Carl Zeiss Axiovert 40 CFL microscope with a Zeiss EC Plan-Neofluor 40 \times objective (NA = 0.75) forms the basis of the setup. For illumination of the particles in the microfluidic channels a dual cavity flashlamp-pumped Nd:YAG laser (Solo PIV, Solo III 15 Hz, New Wave Research, USA) is used. The laser emits two pulses of light with a wavelength $\lambda = 532$ nm and a pulse duration of about 6 ns. A beam expander (2 \times , Edmund Optics 532 nm 2-8 \times NT64-418) and diffuser plate between laser head and microscope are used to widen of the laser beam for more homogeneous channel illumination. Image pairs (1376 \times 1040 pixels) are recorded with a cooled charge coupled device (CCD) PCO Sencicam qe 670 KD double-shutter camera (PCO, Germany). The images are captured in approximately the middle of the channels by manual adjustment of the focal plane.

Red fluorescing (optimum excitation/emission wavelengths are 542/612 nm) polystyrene particles with a diameter $d_p = 1.0$ μ m are used to improve the quality of the μ PIV recordings (Fluoro-Max particles, Thermo Fisher Scientific, USA) [27]. These particles have a density close to water ($\rho = 1.05$ g/cm³), and a refractive index of 1.59 at 589 nm (25 $^\circ$ C). An optical filter (reflector module FL P&C, Zeiss, Germany) between objective and camera is used to reflect light at illumination wavelength and transmit fluorescent light at longer wavelengths.

Laser flash lamps and camera are triggered independently with a BNC model 555 pulse/delay generator (Berkeley Nucleonics Corporation, USA). The camera and pulse generator are connected to each other via the computer. The laser Q-switches are triggered internally. Synchronisation is done such that the first laser flash comes at the end of the first image recording. The time of the second pulse then comes in the second recording. This enables full control of the time interval Δt between the two images [27]. In total 5 \times 39 image pairs are recorded. About 5 min are required to record 195 image pairs.

Fluid flow rates are set with a Harvard PHD2000 syringe pump (Harvard Apparatus, USA). The μ PIV particle solutions are supplied from a gastight 23 mm diameter 25 mL glass syringe. The syringe is shielded from light to ensure the reusability of the particles. The nitrogen gas pressure in the lower main channel and side channels is controlled using an EL-PRESS digital pressure controller, operated via a FLOW-BUS (Bronkhorst High-Tech, The

Netherlands). Microfluidic devices are placed in a chip holder, and connected to syringe and pressure controller via dimethylpolysiloxane capillaries (180 μm inner diameter) and PEEK tubings (see Figure 2.5B).

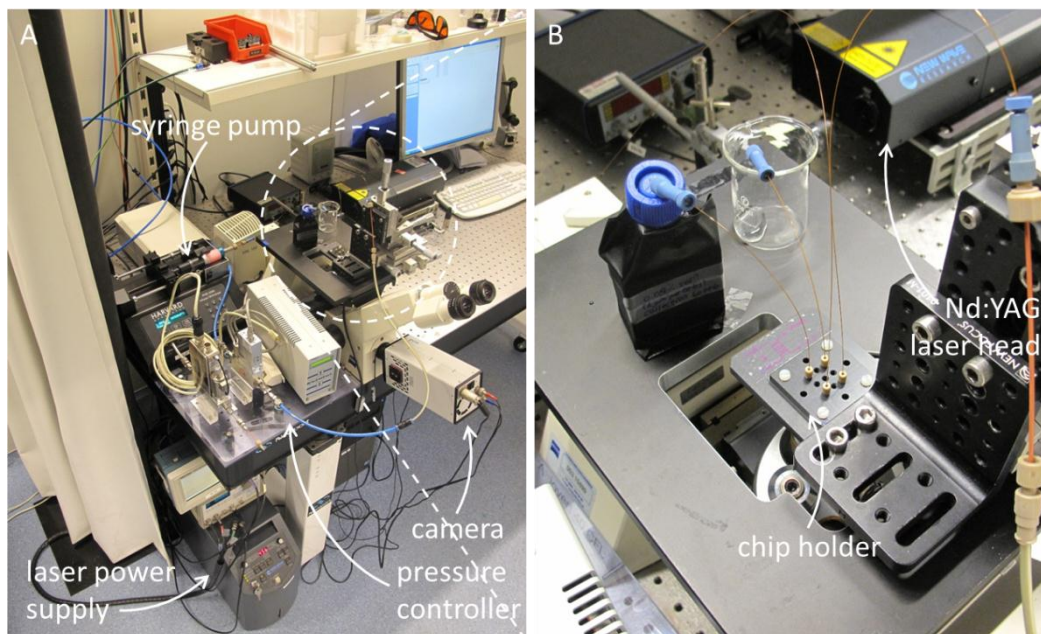


Figure 2.5 The setup as used for the micro-PIV experiments.

2.3.3.2 Experiments

Three microfluidic devices with different porosities are used in order to determine experimentally effective slip lengths as function of the protrusion angle. For each chip, a set of experiments is performed in which the protrusion angle is varied. Stable gas/liquid interfaces are obtained by balancing the gas pressure in the side channels to the pressure of the liquid flowing through the upper main channel. For each angle, 195 images pairs are captured, from which the flow field is obtained. From these flow fields, the effective slip can be calculated.

Since for the calculation of the velocity vector field multiple image pairs are utilised, having a stable and steady state flow, and a stable gas/liquid interface is of great importance. Before performing the experiments, the particle solution is degassed in order to promote a stable bubble mattress. After stabilisation of the gas/liquid interfaces, the bubble protrusion angle is varied by slowly changing the gas pressure. The flow rate of the particle solution is fixed for all angles in a set of experiments.

For a precise determination of the image magnification, a calibration grid was used. Each pixel (with a size of $6.45 \times 6.45 \mu\text{m}^2$) corresponds to $0.161 \times 0.161 \mu\text{m}^2$ on the images. This gives a magnification $M = 40.1$, which corresponds to the specified objective magnification. For each experiment, also various reference images (with bright field illumination) are captured. These images are focussed on or slightly above the bottom of the channels (the glass side of the chips). They are used to determine the exact geometry of the microfluidic devices. Furthermore, they are utilised to determine the average protrusion angle in each experiment

by employing DropSnake [39], a plug-in in ImageJ [40]. The average angle is calculated from at least 8 individual bubble protrusion angles for each experiment.

Important experimental settings and variables are provided in Table 2.2. The time difference Δt between two successive images is calculated using the given chip specifications ($H = 50 \mu\text{m}$; $D = 100 \mu\text{m}$), using the average liquid velocity and a loss of correlation of 20% due to out-of-window movement in the x -direction.

Table 2.2 Important settings and variables for the μPIV experiments.

Operational settings			Timing/triggering settings		
Variable	Value	Unit	Variable	Value	Unit
Set flow rate ϕ	45	$\mu\text{L}/\text{min}$	Time difference Δt	7	μs
Reynolds number Re	10	–	First shutter opening	0 – 1000	μs
Particle diameter d_p	1.0	μm	Triggering laser flash LF1	804	μs
Particle volume fraction V_{fr}	0.1	%	Triggering Q-switch QS1	1000	μs
Number of image pairs N_{IP}	195	–	Triggering laser flash LF2	812	μs
Depth of field δz_f	0.79	μm	Triggering Q-switch QS2	1007	μs
Correlation depth δz_c	3.1	μm			
Pixel size δ_{pix}	0.161	μm			

2.3.3.3 Image pre-processing

Pre-processing is generally performed to improve the interrogation process, and to improve the validity of the obtained velocity field. The quality of the raw images and their processing after acquisition determines the overall performance of the μPIV results. As the quality of our raw μPIV images is very high, image processing is relatively straightforward, using the methods given below [29, 41]. Since the laser intensity is different for image A and B, the captured A- and B-images are processed separately.

The image pre-processing scheme consists of the steps listed below, and is performed in MATLAB (version 2011b). Both image pre-processing scheme and interrogation algorithm are developed in the Physics of Fluids research group at the University of Twente, The Netherlands.

1. Cropping of the images because our region of interest, which are the microfluidic channels, forms only a minor part the acquired images.
2. Image blurring by low pass spatial filtering. Filtering of images is generally performed to remove random noise [29, 42].
3. Calculation of the spatial-averaged mean intensity image (the background image) from either all images A or B. Individual particles are not visible anymore on the image background, as they are averaged out for a large number of images.
4. Subtraction of the background image from all processed images to remove background light originating from unfocussed particles.

5. Addition of 5 successive images to increase the particle density artificially. The steady state flow over the bubble mattress makes this step is feasible. A higher particle density ultimately can improve the resolution of the vector field.

2.3.3.4 Interrogation

A conventional multigrid ensemble interrogation approach is utilised to calculate the flow field for each experiment from the corresponding pre-processed images [27, 29].

First, the images are divided in uniformly spaced interrogation windows (IWs). The overlap of the interrogation windows equals 50% in all interrogation passes. The fluid flow through the channel is mainly in the x -direction, where the x -directional velocity u is varying above the wall exhibiting alternating slip conditions at $y = H$ (see Figure 2.6). The liquid velocities in the x -direction are three orders of magnitude larger than those in the y -direction. For determination of the slip length, only the $u(y)$ -velocity profiles are utilised. As this improves the resolution in the y -direction, while simultaneously loss of correlation in the x -direction is reduced, the interrogation windows are longer in the x -direction.

The multigrid interrogation procedure consists of three passes, where the size of the interrogation windows is decreased each pass. The displacements calculated in the first pass are used in the second pass for pre-shifting of the interrogation window in image B, as this reduces loss of correlation due to out-of-window movement. Similarly, the displacements obtained in the second pass are utilised in the final pass. The interrogation window sizes ($x \times y$) for pass 1, 2, and 3 are respectively 128×64 pix, 64×32 pix, and 32×16 pix.

2.3.3.5 Slip length extraction

From the calculated vector fields, the effective slip length for that specific experiment can be calculated. Prior to slip length calculation, all data points which are outside the channel or inside the bubbles are removed from the velocity field. In the slip length calculation, only the liquid velocities in the x -direction are considered.

The slip length is calculated from the vector fields following two different approaches, which are schematically represented in Figure 2.6. The concept of these approaches is similar to the shear rate and fluid flux method as used for numerical evaluation of the slip (section 2.1.3).

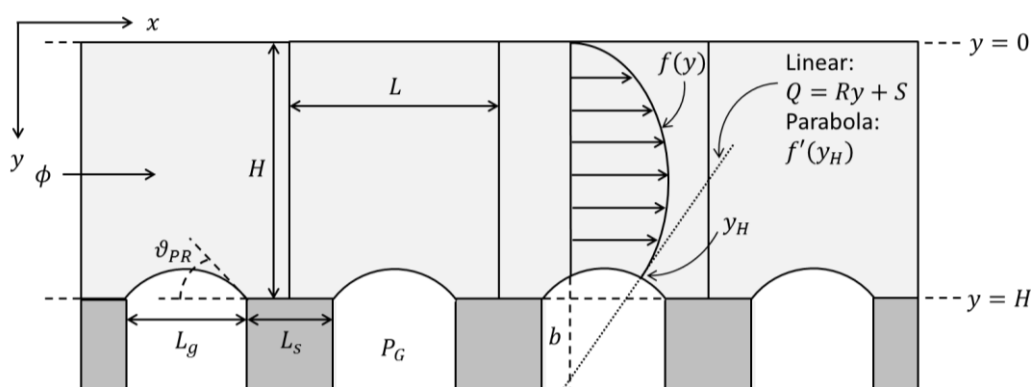


Figure 2.6 Schematic drawing of the coordinate system for the μ PIV plots. Also the two approaches for extracting the slip length from the vector plots are represented.

The first approach is a linear approximation, where a straight line is fitted through the last 5 data points in each vector column (a vector field has vector rows in the x -direction, and vector columns in the y -direction). Mathematically, this line is described by:

$$Q = Ry + S \quad (39)$$

Here, R is the slope of the line, corresponding to the approximate shear rate du/dy at that particular position (see Figure 2.6). It should be noted that in the micro-PIV vector plots, $y = 0$ corresponds to the upper no-slip wall, and $y = H$ corresponds to the lower slip wall. Now, the following expression is derived that gives the slip length at a particular x -position as function of slope R , y -intercept S , and channel height H :

$$b = -\left(\frac{S}{R} + H\right) \quad (40)$$

Subsequently the effective slip length is obtained by averaging the slip lengths obtained for all vector columns.

The second approach is the parabola approximation, where a second-order polynomial is fitted through to x -directional velocities u in each vector column. Although the system design suggests to fit a polynomial going through $(y, u) = (0, 0)$ at the upper wall (i.e. $C = 0$ in equation (38)), because of the uncertainty in the location of upper and lower wall (and hence in the removal of velocity vectors not located in the liquid phase) this constraint is not used in fitting the parabola:

$$u(y) = f(y) = Ay^2 + By + C \quad (41)$$

Having defined the lowest y -position at the bubble mattress side y_H (where $y_H < H$ above a bubble), and knowing both shear rate ($du/dy = f'(y_H)$) and liquid velocity ($u = f(y_H)$) at that position, easily an equation can be derived that gives the slip length as function of the polynomial coefficients A , B , and C , of y_H , and of the channel height H :

$$b = y_H - \left(\frac{f(y_H)}{f'(y_H)} + H\right) = y_H - \left(\frac{Ay_H^2 + By_H + C}{2Ay_H + B} + H\right) \quad (42)$$

Obviously, this equation is based on the slip length definition as given in equation (1). By averaging the slip lengths obtained for all vector columns the effective slip length is obtained.

The calculation of the error in the slip length b is described in more detail in appendix D.

3 NUMERICS – RESULTS AND DISCUSSION

3.1 Introduction

This chapter describes the main results of the numerical part of this study. All results are obtained from simulations with a non-periodic model in which fluid flow is pressure-driven. However, in the model development also Couette flow is considered, as are periodic geometries. The differences between these models and the resulting slip length profiles are elaborately discussed in a previous report [34]. The most important considerations regarding the model development are given in section 3.2.

All results in this thesis are discussed by using plots in which the slip length is given as function of the bubble protrusion angle. A typical slip length profile is discussed in section 3.3.

Characteristic Reynolds numbers in microfluidic devices are $Re < 1$ [43], but also a range of $1 < Re < 1000$ has been reported [44]. In our experimental work, typical flow rates are in the range of 20 – 100 $\mu\text{L}/\text{min}$, corresponding to Reynolds numbers in the range of approximately 5 to 25. It is important to investigate the influence of the applied pressure gradient (i.e. the flow rate) on effective slip and mass transfer. This is performed by simulating slip flow for 6 different overall pressure gradients. The results are described and discussed in section 3.4.

One of the assumptions in this model is a rigid gas/liquid interface; i.e. no deformation of the bubble surface by the fluid flow. However, as Gao and Feng [5] pointed out, with high flow rates very high shear forces can be present in the liquid that can deform the bubble surface. The ratio of viscous forces exerted by the flowing fluid and surface forces caused by the bubble surface tension is given by the capillary number Ca [9]:

$$Ca = \frac{\mu L_g \gamma}{\sigma} \quad (43)$$

The constraint of $Ca < 0.1$ [5, 9] is strictly maintained to ensure the assumption of a rigid gas/liquid interface is valid. For parabolic fluid flow, it can be calculated that this condition (for a surface tension of $\sigma = 0.072 \text{ N/m}$; water in contact with air) is fulfilled when $|\partial P/\partial x| < 14 \times 10^5 \text{ Pa m}^{-1}$. For all pressure gradients listed in Table 3.1 for which effective slip and mass transport have been investigated, the requirement that $Ca < 0.1$ holds.

For the experimental part, multiple chips are fabricated with different dimensions and bubble mattress porosities. To investigate the influence of the chip geometry on effective slip length and mass transfer, numerical studies are performed in which the main channel height ($H = 50; 100; 250; 500 \mu\text{m}$) and bubble unit length ($L = 30; 40; 50 \mu\text{m}$) are varied. The values of H and L correspond essentially to the experimentally available chip geometries. However, no influence of these geometric variables on effective slip is found [34] (see Figure C.2). This is expected, as slip length is considered to be a surface property, independent from operating conditions or system dimensions [4, 17, 18].

Table 3.1 Pressure gradients used in the simulations.

$-\Delta P/\Delta x$	Re	u_{av}	ϕ
[Pa m ⁻¹]	[-]	[mm s ⁻¹]	[μ L min ⁻¹]
120	0.01	0.1	0.06
240	0.02	0.2	0.12
600	0.05	0.5	0.3
1800	0.15	1.5	0.9
12000	1	10	6
120000	10	100	60

Finally, the influence of surface porosity ε , or in other words the coverage of the lower wall by bubbles, is investigated. The surface porosity is related to the ratio of solid wall to side channel length $W = L_s/L_g$, which is used to characterise the microfluidic devices, by the following equation:

$$\varepsilon = \frac{1}{1 + W} \quad (6)$$

Experimentally, three values of W are available: $W = 0.5; 1; 1.5$. But in order to have equally spaced porosities, slip flow is simulated for geometries characterised by the porosities ε given in Table 3.2. The mass transfer enhancement for these geometries is computed with respect to the 3 different reference models described in section 2.1.4. The results are described and discussed in section 3.5.

Table 3.2 Bubble mattress porosities ε used in simulations.

ε	W	L_g	L_s
[-]	[-]	[μ m]	[μ m]
$\frac{1}{3}$	2	$13\frac{1}{3}$	$26\frac{2}{3}$
$\frac{1}{2}$	1	20	20
$\frac{2}{3}$	$\frac{1}{2}$	$26\frac{2}{3}$	$13\frac{1}{3}$

Finally, the results are compared to slip lengths given by the analytical model developed by Davis and Lauga [4], which is provided in equations (2) and (3). According to this equation, slip lengths are linearly dependent on the surface porosity ε . In line with that, for our numerical results also the intrinsic or porosity-corrected slip lengths b_b (see appendix A.2) are computed to examine if they are constant for varying W .

3.2 Model development

3.2.1 COMSOL models

The greater majority of numerical studies published so far concern periodic Couette flow [4, 9, 12]. However, in practice generally parabolic flow profiles are encountered. The velocity profiles in the microfluidic devices used in this study are also parabolic. Furthermore, the devices are of finite length, i.e. non-periodic. Hence all results described in the next sections are obtained from simulations with non-periodic pressure-driven flow models.

In order to create a model that describes the experimental devices properly, model development was performed gradually. Periodic Couette flow models were used as a starting point, as these models can be validated with recent work in literature. Subsequently the flow type is changed to pressure-driven flow, and non-periodicity is introduced in the models. Furthermore, the two methods of calculating the slip length as described in section 2.1.3 are compared with each other.

For both calculation methods, the slip length profiles of all models are in qualitative agreement with $b(\vartheta_{PR})$ -profiles published before [4, 9, 12]. Quantitatively the curves are considerably different, however. For an elaborate discussion is referred to a previous report [34]. Here, only the most important differences are listed.

- When comparing Couette flow and pressure-driven flow models, slip lengths are larger in the latter models. These differences are observed for both slip length calculation methods, irrespective of model periodicity.
- For both types of flow, dimensionless effective slip lengths are larger in periodic models than in non-periodic models. It is hypothesized that these differences originate from the loss of momentum in the x -direction in non-periodic models, which contain both an entrance and outlet domain (see Figure 2.1), when the fluid starts to flow over the bubble mattress (energy is required to re-establish the flow profile).
- The differences between periodic and non-periodic models are more pronounced when using the fluid flux method for calculating the slip length. Likely this is a result of the calculation method. The slip length b obtained using the fluid flux method depends on the fluid flux ϕ , the average pressure gradient $\delta P/\delta x$ over the middle $(N - 4)$ bubble units, the height of the model H , and the liquid viscosity μ . All these variables are macroscopic properties, which are dependent on the overall model geometry. However, when b is calculated from the shear rate, local flow conditions are considered only above the middle $(N - 4)$ bubble units, which are averaged to obtain the effective slip length. The use of macroscopic or local flow conditions for calculating the slip length may give rise to small differences.
- When using the shear rate method to compute the effective slip, the height of the calculation line directly influences the obtained slip length (see Figure C.3 in appendix C). According to the definition of b , the velocity gradient should be calculated at $y = 0 \mu\text{m}$ (equation (1)). However, the lowest value is limited by the maximum protrusion depth of the bubble. As this depth is always larger than 0, the shear rate method overestimates the actual slip length (see also Figure 2.2).

3.2.2 Geometry considerations

Having a developed flow profile before entering the bubble mattress section is highly desirable. Setting the flow profile is no option, as for making a proper comparison between periodic and non-periodic models flow needs to be pressure-driven (in COMSOL, periodic models can only be pressure-driven). An entrance/outlet domain is therefore necessary in non-periodic models. And although the length of these domains does influence the pressure gradient and fluid flux over the mattress section, slip length profiles are unaffected [34]. For both in- and outlet domain, $2L$ is selected as the standard length (see also appendix B.2).

For non-periodic models, it is important that the bubble mattress is sufficiently long to ensure the transition to fully developed flow profile is completed when the fluid leaves the entrance domain and enters the bubble mattress section. Therefore slip length profiles were calculated for different bubble mattress lengths ($N = 5; 10; 15; 30; 60$) [34]. No influence of mattress length N on the effective slip length b is found [34]. For all N investigated, $b(\vartheta_{PR})$ -curves are similar. Hence the selection of the standard bubble mattress length is based on practical considerations: in a very short model, possible side effects may easily influence the results, whereas a very long model would unnecessarily lead to very long simulation times. Hence $N = 15$ is chosen as the standard bubble mattress length.

Furthermore, it is important to know the length over which the flow is developing, as entrance effects and a developing flow profile can affect adversely the obtained effective slip length for a certain surface geometry. Comparison of pressure gradient profiles over the middle $(15 - 2n)$ bubble units, where n is an integer where $2 < 2n < (15 - 1)$, reveals that the length of the transition zone (the length required for obtaining a fully developed flow profile after entering the first bubble unit) is 2 bubble units [34]. Hence for models with $N = 15$, the pressure gradient is calculated over the middle 11 bubble units.

3.3 Protrusion angle

A typical slip length profile is given in Figure 3.1 (solid line), in which the dimensionless slip length is plotted as function of the bubble protrusion angle. The slip length profile ($b(\vartheta_{PR})$ -profile) can be divided into two sections, separated by a critical protrusion angle ϑ_C . Here, this angle is $\vartheta_C = 55^\circ$. For $\vartheta_{PR} < \vartheta_C$ the slip length is positive, i.e. reduced friction towards fluid flow; for $\vartheta_{PR} > \vartheta_C$ slip lengths are negative, i.e. increased friction. The critical protrusion angle observed here is lower than found in other studies, which are in the range $62^\circ - 69^\circ$ [4, 9, 12]. However, all these studies concern Couette flow, which is fundamentally different from pressure-driven flow. Actually, for our periodic Couette flow simulations also a critical angle of 62° is found [34].

The $b(\vartheta_{PR})$ -profiles for pressure-driven flow reveal a qualitative difference between convex and concave gas bubbles. This is also observed by Davis and Lauga [4]. Only positive slip lengths are observed for concave bubbles ($P_L > P_G$), while (in the convex bubble domain) increasing the relative gas pressure P_G too much results in negative slip lengths, or an increased flow resistance. Apparently for $\vartheta_{PR} > \vartheta_C$ the extra resistance created by geometric obstruction of the liquid flow exceeds the reduction in friction by the full-slip bubble surface. The plateau (for $-90^\circ < \vartheta_{PR} < -60^\circ$) in the $b(\vartheta_{PR})$ -curve can be explained by considering that for very negative ϑ_{PR} the liquid inside the pockets becomes more or less stagnant, mean-

ing that the fluid in the main channel experiences an alternating ‘solid/liquid wall’ at $y = 0$. But because the internal liquid friction is lower than the friction between wall and liquid, b remains positive.

The relationship between effective slip and flow resistance is also reflected by a different pressure gradient $\partial P/\partial x$ and fluid flux ϕ for each protrusion angle (see Figure C.6). An increased absolute pressure gradient and a decreased fluid flux result in a lower effective slip length. As such, slip length profiles can be considered as fluid flux enhancement curves, where a positive/negative slip length indicates the relative increase/decrease in fluid flux with respect to a straight channel (having the same dimensions) with two no-slip walls.

3.4 Pressure gradient

For 4 of the pressure gradients given in Table 3.1 the calculated effective slip length profiles and flow-averaged outlet solute concentrations are plotted in Figure 3.1. From the $b(\vartheta_{PR})$ -profiles it immediately follows that the effective slip does not depend on the applied pressure gradient, as all profiles overlap each other. This is in line with theory, saying that the slip length is a function of only the surface geometry, see also equation (2) [4, 17, 18].

A higher applied pressure gradient $\Delta P/\Delta x$ results in a larger flow rate. As the concentration profiles in Figure 3.1 show, an increased flow rate reduces the flow-averaged outlet solute concentration $\langle c \rangle$. For each pressure gradient, the concentration becomes larger with increasing ϑ_{PR} . A higher protrusion angle means a larger solute exchange area (the bubble surface becomes larger), while simultaneously the length over which the solute has to diffuse to reach the upper channel wall is decreased (the bubble protrudes deeper into the liquid).

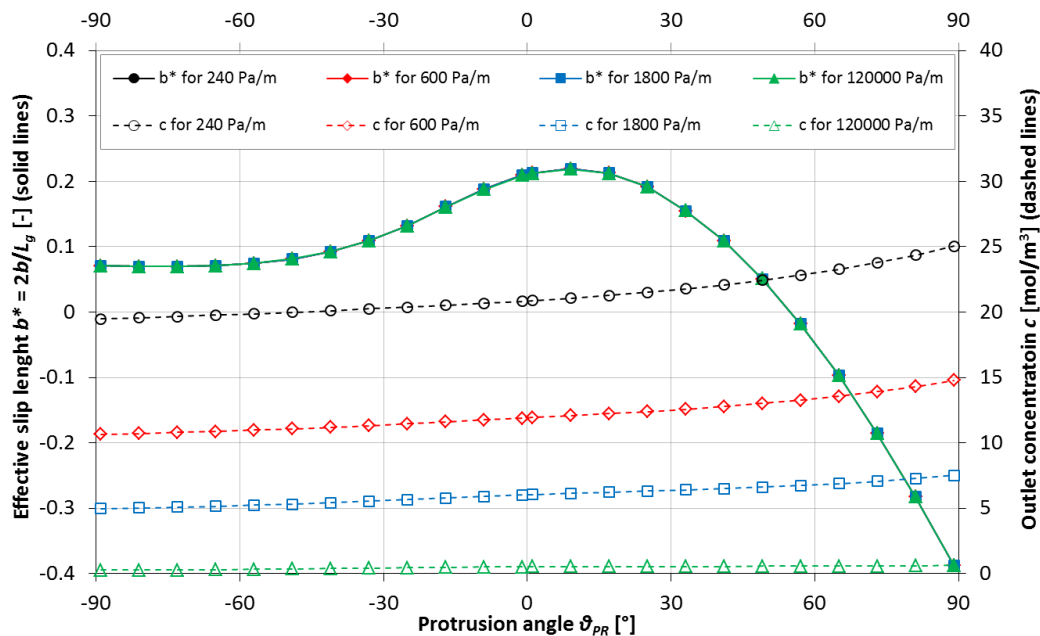


Figure 3.1 Non-periodic pressure driven flow: influence of applied pressure gradient on effective slip and flow-averaged outlet concentration. The outlet concentration is selected such that $c = 0$ for all ϑ_{PR} at $y = H$. For the $c(y)$ -profiles at line 17 (see Figure 2.1) is referred to Figure C.4.

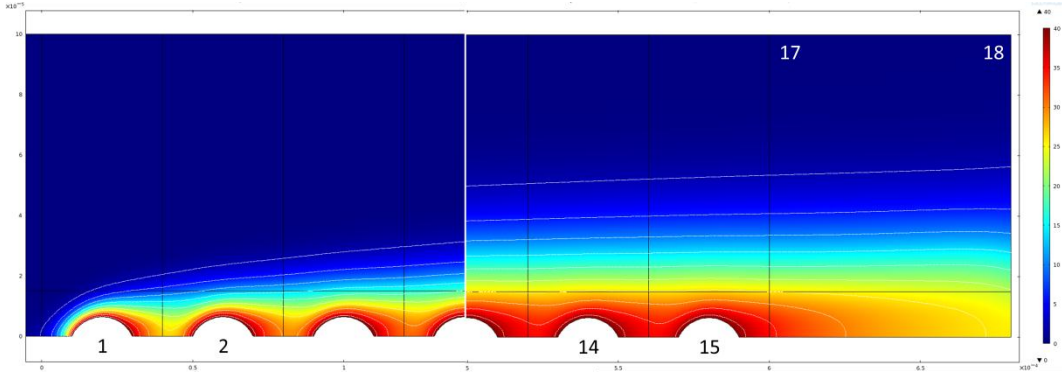


Figure 3.2 2D concentration profiles for non-periodic pressure-driven flow, $\Delta P/\Delta x = -1800$ Pa/m. Dark blue corresponds to $c = 0$ mol/m³; red to $c = 40$ mol/m³. In black, the number of the bubble unit is indicated. The concentration profiles at boundary 17 are provided in Figure C.4.

For investigating the effect of bubble mattress wall slip on mass transfer, a pressure gradient needs to be selected such, that other physical processes than slip flow are avoided that can increase mass transfer or obscure the calculated mass transfer. In this process, this could be the upper wall on which a no-flux BC is applied. In other words, the ratio of convective transport in the x -direction to diffusive transport in the y -direction needs to be high enough. This ratio is generally expressed by the Péclet number Pe :

$$Pe = \frac{Hu_{av}}{D} \quad (44)$$

The solute would then reach the upper wall when $x > (Pe \times H)$. Because the pressure gradient does not influence the slip length, the lowest pressure gradient has been selected for which (for all ϑ_{PR}) the concentration at the upper wall equals 0. This is $\Delta P/\Delta x = -1800$ Pa/m. For this pressure gradient, the 2D concentration surface plot is provided in Figure 3.2. The $c(y)$ -profiles at the outlet are given in Figure C.4. For $\Delta P/\Delta x = -1800$ Pa/m, the average liquid velocity u_{av} is about 1.5 mm/s, which gives $Pe = 150$. This number confirms that the concentration at the upper wall is negligible, as $x > 150 \times 10^{-4}$ m for the solute to reach the upper wall, while the length of the model is only 7×10^{-4} m.

3.5 Surface porosity

3.5.1 Slip length

In Figure 3.3 the $b(\vartheta_{PR})$ -profiles are plotted for various porosities ε . These profiles show that the effective slip length becomes larger with increasing surface porosity. This is expected, as with increasing ε the area of the full-slip gas/liquid interface at the lower wall becomes larger, which in turn reduces the friction towards fluid flow. For all porosity values (for all W), the maximum slip length is obtained for a protrusion angle of 9° . The profiles cross each other at $\vartheta_{PR} = 57^\circ (> \vartheta_C)$, where b is slightly negative. Finally, the relative increase in maximum slip length is not constant, but becomes larger with increasing porosity.

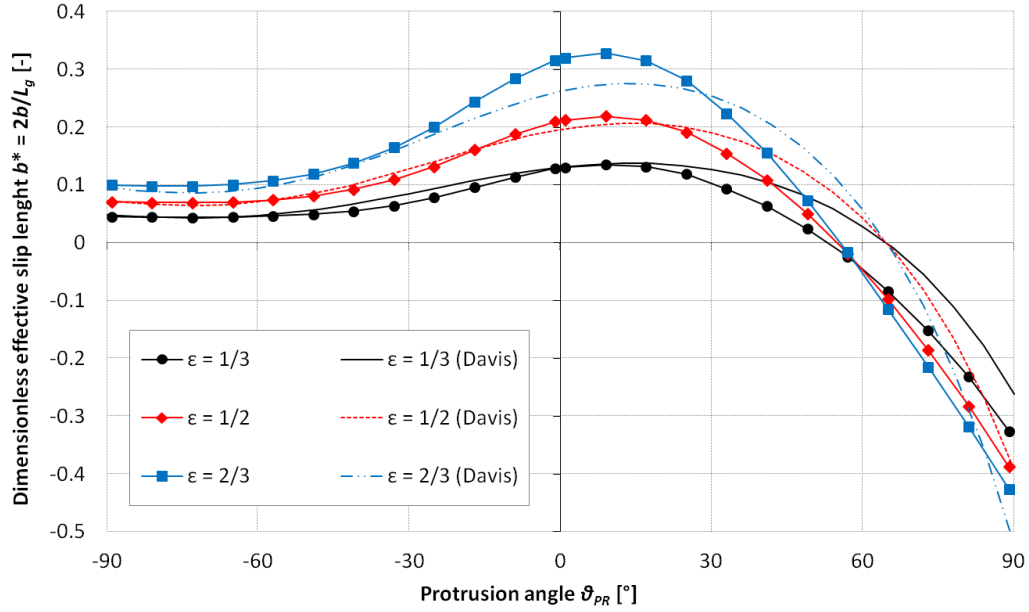


Figure 3.3 Slip length profiles obtained from simulations (lines with data points) and from the analytical model of Davis and Lauga [4] (lines without data points) for different W .

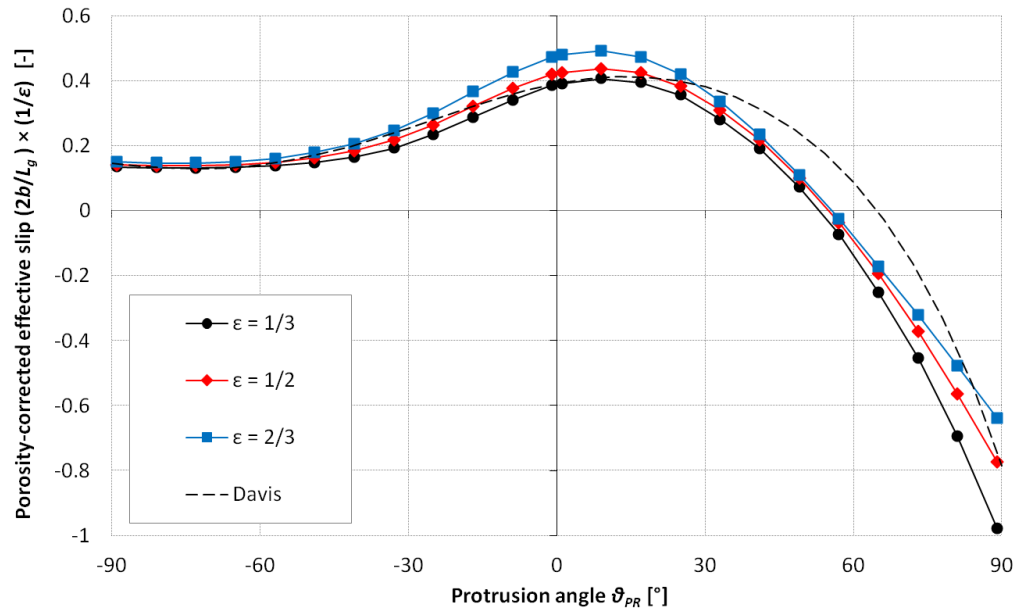


Figure 3.4 Porosity-corrected slip length profiles obtained from simulations (lines with data points) and from the analytical model of Davis and Lauga [4] (dashed line) for different W .

The latter observation is not predicted by the analytical slip length model from Davis and Lauga [4], which states that the slip length linearly depends on the porosity. The profile given by this model is also plotted in Figure 3.3. Especially for $\epsilon = 1/3$ and $\epsilon = 1/2$ the slip length magnitude is very close to that predicted by the analytical model. For larger porosities however, the dilute limit model of Davis and Lauga is shown to underestimate the effective slip [19]. Accordingly, the high surface porosity explains why for $-25^\circ < \vartheta_{PR} < 25^\circ$ the

simulated slip lengths for $\varepsilon = 2/3$ are larger than the analytically calculated slip lengths. The non-linear increase in slip for high ε is possibly explained by considering that for high surface porosities the liquid between the bubbles starts to become stagnant, i.e. the liquid starts to flow on top of the bubbles protruding into the liquid. As a result, the bulk liquid encounters a hypothetical lower wall with an alternating pattern of gas/liquid instead of gas/solid. As the internal liquid friction is lower than liquid/solid friction, flow resistance decreases faster than expected.

The different slip behaviour is also reflected by the intrinsic or porosity-corrected bubble slip $b_b(\vartheta_{PR})$ -profiles plotted in Figure 3.4. The profiles are obtained by dividing the slip length profiles in Figure 3.3 by the corresponding porosity. Whereas the porosity-corrected bubble slip is constant for the Davis-model, in our model the intrinsic slip still increases with increasing surface porosity. Again, this is a result of considering bubble mattress geometries which are not in the dilute limit anymore ($\varepsilon > 0.35$).

For $\vartheta_{PR} > 30^\circ$ the shape of the analytical $b(\vartheta_{PR})$ -profiles is considerably different from the simulated profiles. The latter curves show a stronger dependency on the protrusion angle. Furthermore, the Davis-profiles cross each other at $\vartheta_{PR} = 65^\circ$. The reason for this qualitatively different slip behaviour is not fully clear. Likely this is a result of both flow characteristics (Couette or pressure-driven flow), and the method used for calculating the slip length (the fluid flux or shear rate method), as the analytical model is derived for periodic Couette flow using the slip length definition given in equation (1). Indeed the shear rate-based slip length profiles obtained in Couette flow models resemble the analytical model better, as they are somewhat flatter and show a higher critical protrusion angle ($\vartheta_c \approx 62^\circ$) [34]. Despite these small differences, our results are in good agreement with the analytical model of Davis and Lauga [4], and with slip lengths found by others [9, 12], both quantitatively and qualitatively.

3.5.2 Mass transfer enhancement

Both solute flux enhancement E^ψ and flow-averaged outlet concentration enhancement E^c are calculated for the three reference models described in section 2.1.4. The resulting profiles are given in Figure 3.5, together with the slip length and the fluid flux profiles. Inspection of this figure shows that the enhancement profiles E^ψ and E^c are considerably different for all reference situations. This immediately reveals that the fluid flux is an important variable in the solute flux enhancement.

Before discussing the enhancement profiles for the 3 reference situations in more detail, it is important to note that the mass transfer enhancement for reference 1 is a result of (a combination of) the following factors:

1. the actual protrusion depth of the bubble, which depends on the protrusion angle;
2. the changing solute exchange area for in-/decreasing protrusion angle;
3. the presence of a full-slip gas/liquid interface.

This implies that from the $E(\vartheta_{PR})$ -profiles for reference 1 (Figure 3.5B), it is impossible to determine to what extent the protrusion angle or the full-slip boundary condition (BC) at the bubble surface influences mass transfer. The influence of varying protrusion angle on mass transfer enhancement can be observed from the profiles in Figure 3.5C, with corresponds to

reference 2. The effect of a full-slip bubble surface is investigated by calculating the mass transfer relative to reference 3. The corresponding profiles are given in Figure 3.5D.

3.5.2.1 Reference 1

The enhancement profiles for reference 1, which represents a straight channel with two no-slip walls having an alternating pattern of no solute and solute saturation concentration on the lower wall, are plotted in Figure 3.5B. For both types of enhancement, simultaneously mass transfer is enhanced and resistance towards fluid flow is decreased ($b > 0$) for $-30^\circ \lesssim \vartheta_{PR} < 55^\circ$. However, there are some considerable differences when comparing the solute flux and outlet concentration enhancement profiles.

- The solute flux enhancement E^ψ is considerably larger than the outlet concentration enhancement E^c , especially for angles $-20^\circ \lesssim \vartheta_{PR} < 30^\circ$ and large porosities.
- E^c becomes larger with increasing protrusion angle. Furthermore, the rate of increase in $\langle c \rangle$ becomes larger when ϑ_{PR} increases. Note that for reference 1 the outlet concentration is constant, as is the solute flux. Finally, the solute concentration in the fluid above the bubble mattress only becomes slightly larger when the porosity is increased, except for large protrusion angles.
- Compared to the concentration enhancement profiles, the E^ψ -profiles show next to a larger dependency of the enhancement on the porosity ε , also a declining enhancement with increasing protrusion angle.
- For large porosities, even an optimum E^ψ is observed. The solute flux is maximised by increasing the porosity and by establishing a bubble mattress with $20^\circ < \vartheta_{PR} < 40^\circ$. For the same applied pressure gradient (pumping power), solute flux enhancements up to 25% can be achieved.

The differences between E^ψ and E^c can be explained by considering the dependency of the fluid flux ϕ on the protrusion angle. As mentioned before, the $b(\vartheta_{PR})$ -profiles in Figure 3.5A in essence show the fluid flux enhancement over the bubble mattress with respect to reference 1. According to these profiles, fluid flow is significantly enhanced over a bubble mattress as a result of slippage, especially in the region $-30^\circ \lesssim \vartheta_{PR} \lesssim 45^\circ$. For larger angles, the friction towards flow increases significantly, resulting in a lower fluid flow (see also Figure C.6). Furthermore, the dependency of fluid flux on bubble protrusion angle becomes stronger for larger porosities.

Recalling that $\psi = \phi \langle c \rangle$, the simultaneously increased fluid flow and solute concentration explains why E^ψ is significantly larger than E^c for $-20^\circ \lesssim \vartheta_{PR} < 30^\circ$. For $\vartheta_{PR} < -20^\circ$ slip lengths gradually approach zero, explaining why E^ψ - and E^c -profiles overlap each other. For $\vartheta_{PR} > 30^\circ$, slip lengths are decreasing sharply, leading to lower fluid fluxes and hence lower E^ψ . For $\varepsilon > 0.5$ and large ϑ_{PR} , the decrease in ϕ is larger than the increase in $\langle c \rangle$, and as a result the corresponding E^ψ -profile shows a maximum solute flux enhancement.

3.5.2.2 Reference 2

The mass transfer enhancement with respect to reference 1 can originate from an increased protrusion angle, from the presence of a full-slip gas/liquid interface, or from both. By calculating the enhancement with respect to reference 2, the effect of varying protrusion angle on

mass transfer is isolated, as the porosity ε and the slip conditions are similar in bubble mattress and reference model for all ϑ_{PR} . The profiles are plotted in Figure 3.5C.

The outlet concentration enhancement E^c profiles show that the position of the gas/liquid interface directly influences E^c . A high ϑ_{PR} means a high bubble protrusion depth, thereby obstructing liquid flow at the slip surface (at $y = 0$). This implies that the fluid flow at the slip surface is reduced. As a result, the ratio of convective to diffusive transport, i.e. the Peclet number, becomes smaller at the wall. A higher protrusion depth also means the solute enters the liquid phase at a higher position. Both effects result in broader (less steep) concentration gradients in the channel. Moreover, the solute exchange area becomes larger when increasing ϑ_{PR} . As a result, a considerable concentration enhancement is observed when the protrusion angle increases. For $-30^\circ < \vartheta_{PR} < 30^\circ$ the enhancement does not considerably change when increasing the porosity. This is expected, as porosity and slip conditions are similar in both bubble mattress and reference.

The E^ψ and E^c enhancement profiles are qualitatively and quantitatively different. Qualitatively, as for positive angles the order of the E^ψ -profiles is the reverse of the E^c -profiles. Quantitatively, as except for angles close to 0° , the solute flux enhancement is smaller than the concentration enhancement. Again, these differences can be explained by considering the $\phi(\vartheta_{PR})$ -profiles. For $-5^\circ < \vartheta_{PR} < 20^\circ$, the fluid flux is approximately constant, so the enhancement is a result of only the increased solute concentration, i.e. $E^\psi = E^c$. For both lower and larger angles, the flux is much lower than in the reference situation, so $E^\psi < E^c$.

As mentioned before, for larger porosities the fluid flux decreases faster with increasing protrusion angle. Considering that the fluid flux in the reference corresponds to the flux over the bubble mattress for 0° , this explains why the order of the E^ψ -profiles is reversed for positive angles with respect to the E^c -profiles.

3.5.2.3 Reference 3

To investigate the effect of the presence of a full-slip gas/liquid interface on mass transfer enhancement, reference 3 is similar to the bubble mattress for all ϑ_{PR} , except the conditions at the bubble surface. In reference 3 a no-slip BC is applied to the bubble surface. The resulting $E(\vartheta_{PR})$ -profiles are plotted in Figure 3.5D, which show that the presence of a full-slip BC has a positive effect on mass transfer ($E \geq 1$) for essentially all protrusion angles. Furthermore, this effect becomes more pronounced when the surface porosity increases, in particular for E^ψ .

$E^\psi > E^c$ is a result of the large difference in fluid flux for bubble mattress and reference 3 for each protrusion angle. In the bubble mattress the flow obstruction by the protruding bubble is partially offset by the slip conditions at the gas/liquid interface. In reference 3 this geometric obstruction is accompanied by a no-slip bubble interface. This effect is amplified for increasing bubble mattress porosity. The differences in ϕ result in large solute flux enhancements E^ψ . For large porosities ($\varepsilon > 0.5$) and $\vartheta_{PR} > 30^\circ$, the decrease in E^ψ may be explained by the formation of stagnant liquid layers between the bubbles in reference 3 (L_s is relatively small) over which the liquid flows more easily. This implies that the increase in resistance towards fluid flow is less pronounced for reference 3 than for the bubble mattress. As a result, the relative difference in fluid flux for reference 3 and bubble mattress becomes lower, resulting in a decreasing solute flux enhancement E^ψ .

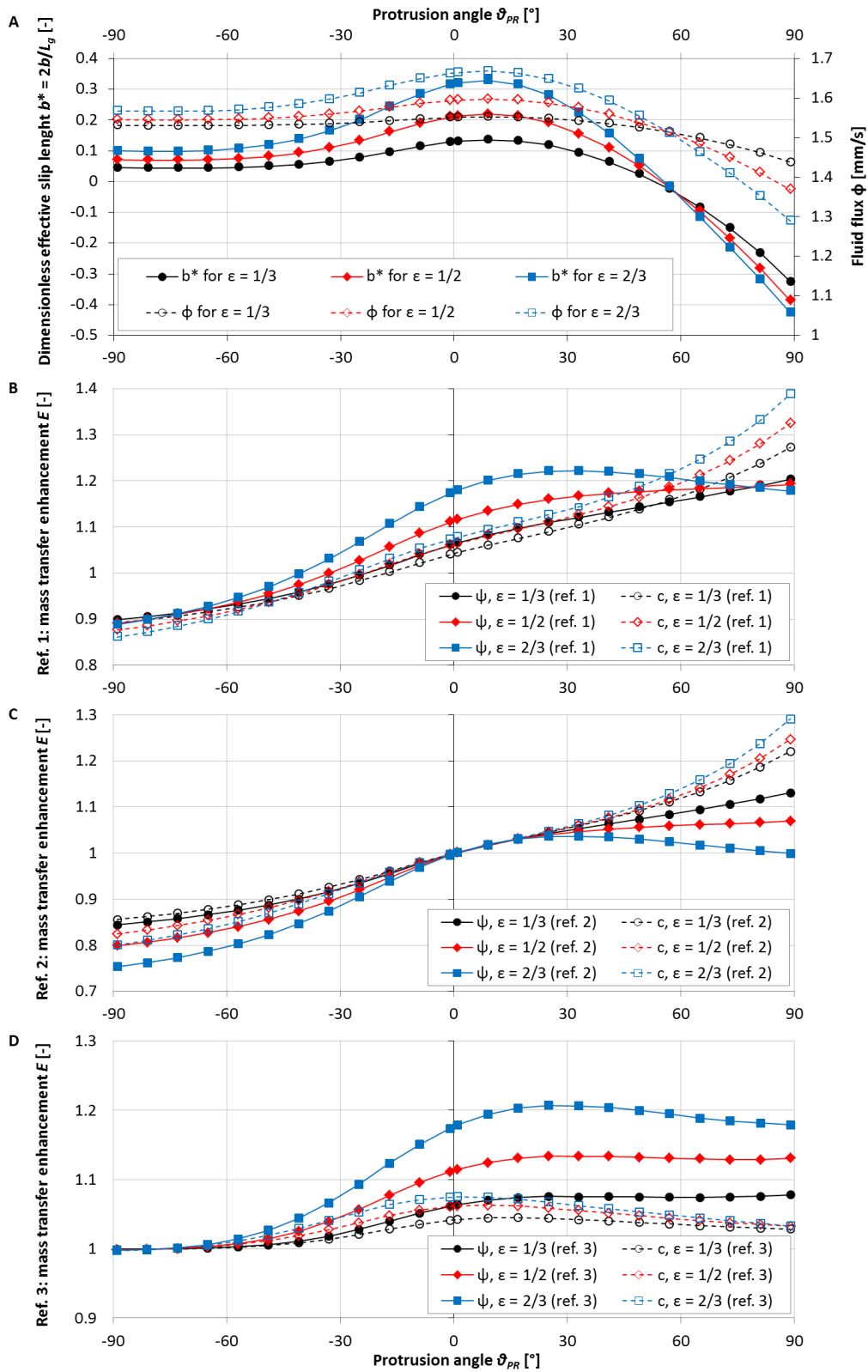


Figure 3.5 Slip length and fluid flux profiles are plotted in (A). The mass transfer enhancement profiles (based on both solute flux ψ and flow-averaged outlet concentration $\langle c \rangle$) are plotted in (B) for ref. 1, in (C) for ref. 2, and in (D) for ref. 3. The profiles are computed for three different porosities ϵ .

Apparently, the improvement in flow-averaged solute concentration between reference 3 and the bubble mattress is limited ($E^c < 1.08$). For both flows convective transport is mainly in the x -direction, meaning that diffusion plays a major role in y -directional solute transport. The slip gas/liquid surface in the bubble mattress possibly results in a kind of wake behind the bubble (see Figure 3.2), resulting in a reduced ratio of convective to diffusive transport (a reduced Pe-number). On the other hand, the alternating slip/no-slip pattern at the lower wall may induce secondary flows, which could increase the effective diffusivity of the solute. A larger diffusivity would result in a higher flow-averaged solute concentration in the channel. Both effects give higher concentrations $\langle c \rangle$, but the effect is limited. For high ε however, also in the bubble mattress the liquid flow close to the solid wall between becomes more stagnant, lowering $\langle c \rangle$ and thereby also E^c .

That the profiles overlap when making the bubble protrusion angle more negative can be explained by considering that for very negative ϑ_{PR} the liquid between the bubbles becomes more or less stagnant. In that situation, the presence of a full-/no-slip BC at the bubble interface does not matter anymore: the solute is only transported by diffusion. In that case, it must follow that $E^\psi = E^c$.

3.5.2.4 Major source of mass transport enhancement

Since the factors 1/2 (influence protrusion angle) and 3 (influence slip BC) mentioned on page 34 are mutually dependent, adding up the mass transfer enhancements for reference 2 and 3 will not exactly return the enhancement profiles for reference 1. In particular for positive protrusion angles, the difference in $\Delta(E) = E(\text{ref. 1}) - E(\text{ref. 2}) - E(\text{ref. 3}) + 1$ is very small ($|\Delta(E^\psi)| < 0.03$ and $|\Delta(E^c)| < 0.07$) as Figure C.7 shows. For very negative angles, the sum of the enhancements for references 2 and 3 does not always yield the overall enhancement. However, positive angles are of main interest in practical applications, and the low values of $\Delta(E)$ indicate that mass transport enhancement indeed results from a combination of the shape and size of solute exchange area, and the presence of a full-slip bubble surface.

As a comparison of the $E^c(\vartheta_{PR})$ -profiles in Figure 3.5C and D shows, it can be concluded that for low protrusion angles (roughly $-20^\circ < \vartheta_{PR} < 20^\circ$) the mass transfer enhancement mainly originates from the full-slip boundary condition, but that for all other protrusion angles ($\vartheta_{PR} < -20^\circ$ and $\vartheta_{PR} > 20^\circ$) the enhancement is mainly a result of the geometry of the gas/liquid interface. For $-20^\circ < \vartheta_{PR} < 55^\circ$, both mass transport and fluid flow are enhanced. For positive angles, a trade-off between solute concentration enhancement and effective slip is observed.

The solute flux enhancement E^ψ is the result of the interaction between solute outlet concentration and fluid flow.

- For low porosities ($\varepsilon \lesssim 0.4$) and $\vartheta_{PR} > 30^\circ$, E^ψ is strongly influenced by the position of the gas/liquid interface. In case $-30^\circ < \vartheta_{PR} < 30^\circ$, the slip BC dominates.
- Irrespective of porosity, the enhancement for $\vartheta_{PR} < -30^\circ$ is mainly determined by the bubble surface geometry (slip lengths approach zero).
- For high porosities ($\varepsilon \gtrsim 0.4$) and $\vartheta_{PR} > -30^\circ$, the full-slip gas/liquid interface is the major source of mass transport enhancement. The dominance of the slippery bubble surface becomes stronger with increasing porosity.

Even though the geometry of the bubble surface plays a significant role in E^ψ , for positive protrusion angles the overall enhancement is predominantly a result of the slip conditions, i.e. the enhancement in fluid flux. The larger the porosity, the larger the dependency of fluid flow and hence overall solute flux enhancement on the protrusion angle becomes. This explains why for large porosities $\varepsilon > 0.5$ even an optimum enhancement is observed (about 25° for $\varepsilon = 2/3$). The solute flux enhancement can be maximised by increasing the porosity and by establishing a bubble mattress with moderate protrusion angles, i.e. $20^\circ < \vartheta_{PR} < 40^\circ$. For the same applied pressure gradient (pumping power), solute flux enhancements up to 25% can be achieved.

4 EXPERIMENTAL – RESULTS AND DISCUSSION

4.1 Introduction

In this chapter the μ PIV experiments and the experimental results are discussed. The μ PIV experiments consist of image acquisition, image processing, and vector field calculation by ensemble correlation. The resulting vector fields are used to calculate the effective slip length in each experiment. Three microfluidic devices with different geometric characteristics are used. For each chip, multiple experiments are performed in which the bubble protrusion angle is varied. These experiments enable us to investigate the influence of chip geometry and protrusion angle on the effective slip length. As in our μ PIV experiments steady-state flow is desired, for each experiment a stable bubble mattress needs to be established. Some considerations on this are given in section 4.2.

The flow of fluorescent particles over the bubble mattress is captured by acquisition of many images pairs, each consisting of two images separated in time by a particular time delay. In section 4.3 these raw images, the output of the μ PIV experiments, are discussed. In order to improve the correlation procedure, the raw images are pre-processed to enhance the visibility of the particles. The image pre-processing scheme is discussed in section 4.4. Subsequently multigrid ensemble correlation is performed to obtain the particle displacements in the microfluidic channels, from which the vector fields can be calculated. The correlation algorithm is described in more detail in section 4.5. Typical vector fields are discussed in section 4.6.

The obtained vector fields are then used to calculate the effective slip for each experiment. The method how the effective slip length is extracted from the vector fields is described in section 4.7. In section 4.8 the final experimental results are discussed. First, the influence of both protrusion angle and chip geometry on effective slip length is examined. Furthermore, the experimental results and numerically computed slip length profiles are compared.

Unless otherwise indicated, all results shown in this chapter are obtained from the same experiment (chip 1, $\vartheta_{PR} = 38^\circ \pm 3^\circ$).

4.2 Bubble mattress

Prior to image acquisition, a stable bubble mattress needs to be established. This was obtained by carefully adjusting the gas pressure P_G , as the liquid flow rate is fixed in each experiment. The balance between liquid and gas pressure determines the bubble protrusion angle ϑ_{PR} . Experimentally, protrusion angles were obtained in a range of $-5^\circ < \vartheta_{PR} < 45^\circ$. Beyond this range of angles a stable bubble mattress could not be established. For negative angles (low P_G), depinning of the bubbles from the channel corners was observed, resulting in partial filling of the side channels, or even in leakage of the particle solution through the side channels to the gas main channel. For high protrusion angles, bubbles were periodically released from the side channel, or the main liquid channel was partially filled with gas.

For stable interfaces the observed protrusion angles were not constant over the whole length of the main liquid channel. Furthermore, determination of ϑ_{PR} is found to be difficult. Along the depth of the channel (the z -axis), the bubble surface is curved, meaning that the protrusion angle is not equal for different focal planes. Although the angle for the focal plane corresponding to the middle of the channel is valid, no sharp bubble surface is observed when taking a reference image in the middle of the channel. This is caused by the difference in refractive index for the gas/liquid phase. Hence the average ϑ_{PR} is calculated from reference images at or close to the bottom of the channels. Still, the gas/liquid interfaces on these images are somewhat blurred/not very sharp. The uncertainty in calculating the protrusion angles is reflected by the large standard deviations.

Both instability and inhomogeneity of the gas/liquid interface are promoted by (i) the relatively large liquid pressure drop compared to the gas pressure drop, and (ii) by an inhomogeneous FOTS-layer formed during the hydrophobisation of the devices. Often leakage or bubble growth starts from side channels with a thick FOTS-layer on the wall.

4.3 Raw images

A typical raw image pair as obtained in the μ PIV experiments is shown in Figure 4.1. The time delay Δt between image A and B is $7 \mu\text{s}$. The high visibility of the particles is a result of the relatively large particle diameter d_p (larger than $\sim 1\%$ of the characteristic fluid dynamics length scale, i.e. the hydraulic channel diameter [27, 45]), and the low particle image density $N_I = 0.078$. A low particle concentration reduces the background noise stemming from particles which are out of focus, and thus improves the particle visibility [27, 29, 30].

The images correspond to a field of view of $1376 \times 1040 \text{ pix} = 222 \times 167 \mu\text{m}^2$. Particles in focus have a diameter of about 7 pix in the image plane, which is in agreement with references stating that the minimum particle diameter should be at least 3 – 5 pix [28, 29]. The particle displacement ranges from approximately 3 pix near the walls to 12 pix in the middle of the channel, with a typical average displacement of 8 pix [29].

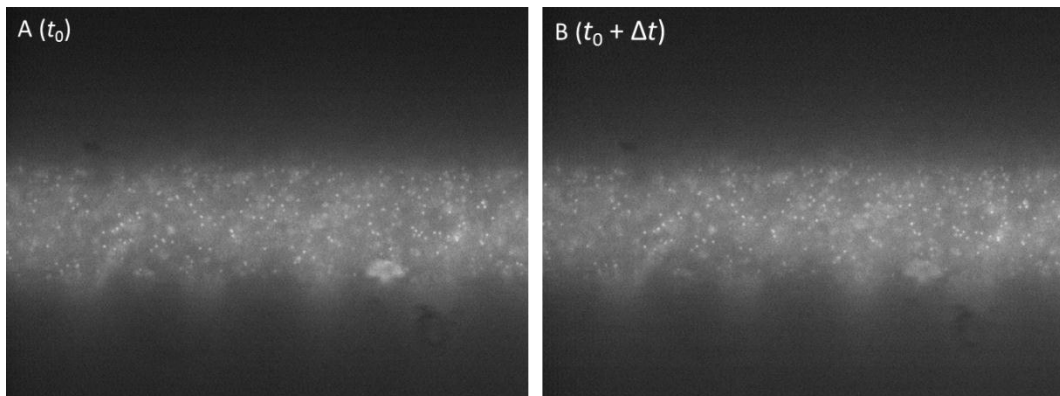


Figure 4.1 A typical example of a raw image pair with a time delay of $\Delta t = 7 \mu\text{s}$.

4.4 Image pre-processing

Image pre-processing is commonly used to enhance the particle visibility, and to reduce the noise in the images [29]. This often improves the quality of the final velocity vector fields, as these fields are obtained by spatial correlation of the particle patterns in image A and B. We also applied a pre-processing scheme to the raw particle images prior to the interrogation analysis.

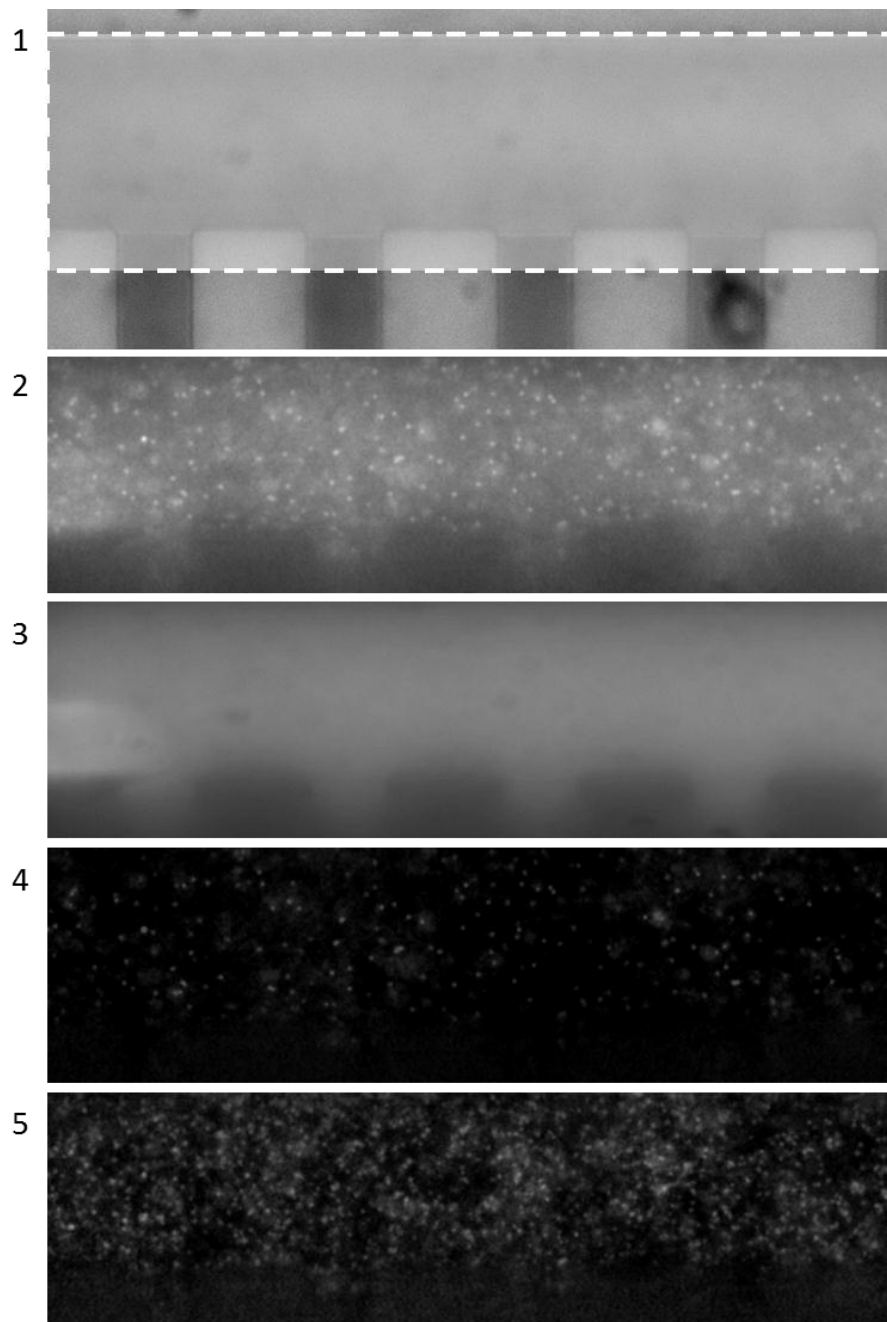


Figure 4.2 Image pre-processing improves the visibility of the particles and removes noise, thereby enhancing the cross-correlation. Here, pre-processing consists of various steps, which are cropping (1), filtering (2), background image calculation (3), background subtraction (4), and image addition (5).

The image pre-processing scheme consists of the steps listed below, where each step is illustrated in Figure 4.2. Due to a disparity in light illumination intensity between the images at t and $t + \Delta t$, images A and B are pre-processed separately.

1. Since our region of interest, which are the microfluidic channels, form only a minor part of the acquired images, the images are cropped. The size of the cropped images is 1376×384 pix. The size in the y -direction corresponds to an integer multiple of the y -component of the largest interrogation window (128×64 pix). This ensures the cropped image is interrogated for all y -coordinates. The top of the cropped image ($y = 0$ pix) corresponds to the no-slip upper wall of the main liquid channel.
2. After cropping of the images, the images are blurred by low pass spatial filtering. Filtering of images is generally performed to remove random noise [29, 42]. This noise can come from thermal effects in the CCD sensor array, or from reflections of light at the walls or within the imaging optics.
3. The cropped and blurred images are used to calculate the average mean intensity image A and B from respectively all images A and B. In the resulting two background images, individual particles are not visible anymore, as they are averaged out.
4. The background images obtained in the previous step are subtracted from the cropped and blurred images to remove background light originating from unfocussed particles. This leaves the image of essentially only the particles in focus, thereby improving the particle visibility considerably [30].
5. To increase the particle image density, processed images are added up following a consecutive sum of five images in row [30]. This is possible because the liquid flow is steady. The artificially increased particle density allows the use of smaller interrogation window sizes, which improves the resolution of the final vector field.

4.5 Correlation

After pre-processing the raw particle images, the particle displacements are determined by ensemble correlation of the particle patterns in images A and B (see Figure 4.3). Each image pair is spatially correlated. However, in μ PIV the effective image density (see equation (11)) is generally very low as a result of the high magnification. Therefore, the ensemble correlation algorithm (also referred to as correlation averaging) is commonly used to compute the displacement of the particles [27-30]. Ensemble correlation increases the effective particle density, and thereby allows reducing the size of the interrogation windows. This improves the spatial resolution of the ultimate vector fields.

The interrogation algorithm used for ensemble correlation of the processed images utilises the multigrid approach [29]. The images are repeatedly interrogated, where the size of the interrogation window is decreased in each interrogation pass. The displacements obtained in each pass are used to refine the offset of the interrogation window in the next pass. This shifting of interrogation window in image B increases the probability that the same particles are encompassed in both interrogation windows, i.e. it reduces the loss of correlation.

Here, the size of the interrogation windows (IWs) is longer in the x -direction, as the liquid flow is mainly x -directional. This reduces loss of correlation due to out-of-window movement in the x -direction, while simultaneously the resolution in the y -direction, which has

our main interest, is increased. The minimum size (in the y -direction) of the interrogation windows is 16 pix. A further reduction of the interrogation window size rarely improves the quality of the vector fields [29]. A commonly used 50% interrogation window overlap is applied to enhance the resolution of the vector fields [28, 29].

Now, the interrogation function Q_C for one interrogation window with size V and W in respectively x - and y -direction can be written as follows, where $I_A(x, y)$ and $I_B(x, y)$ are the intensity functions of respectively image A and B [28]:

$$Q_C(m, n) = \sum_{x=1}^V \sum_{y=1}^W I_A(x, y) I_B(x + m, y + n) \quad (45)$$

m and n are the displacements in the interrogation domain. By calculating and adding up of Q_C for all specified m and n , a spatial cross-correlation function is obtained. The highest peak in this cross-correlation function corresponds to the most probable match of the particle pattern in a specific interrogation window, and hence to the most probable particle displacement [29]. In ensemble correlation, the spatial correlations for all N_{IP} image pairs are added up, yielding the average correlation function R_C :

$$R_C(m, n) = \sum_{i=1}^{N_{IP}} Q_C^i(m, n) \quad (46)$$

This average correlation function R_C gives the average displacement-correlation peak, which is proportional to the effective image density N_{el} , as $N_{el} = N_{IP} N_I$ (see equations (11) and (12)).

The characteristics of the three passes in the multigrid interrogation procedure are provided in Table 4.1, together with the image density for 1 image and for 194 images for each pass. As the numbers show, even for the smallest interrogation domain a very high effective image density is obtained. Please note that all given image densities would be 5 times smaller when the last step in the image pre-processing would be omitted. In that case, the image density for the smallest interrogation window would have been $N_I = 0.078 \ll 1$, which is a common value for μ PIV [29].

Table 4.1 Characteristics of the three passes in the interrogation procedure.

Pass number	Interrogation window size		Image density N_I	
	pix	μm^2	1 image	194 images
1	128×64	20.6×10.3	6.2	1.2×10^3
2	64×32	10.3×5.2	1.6	3.0×10^2
3	32×16	5.2×2.6	0.39	7.5×10^1

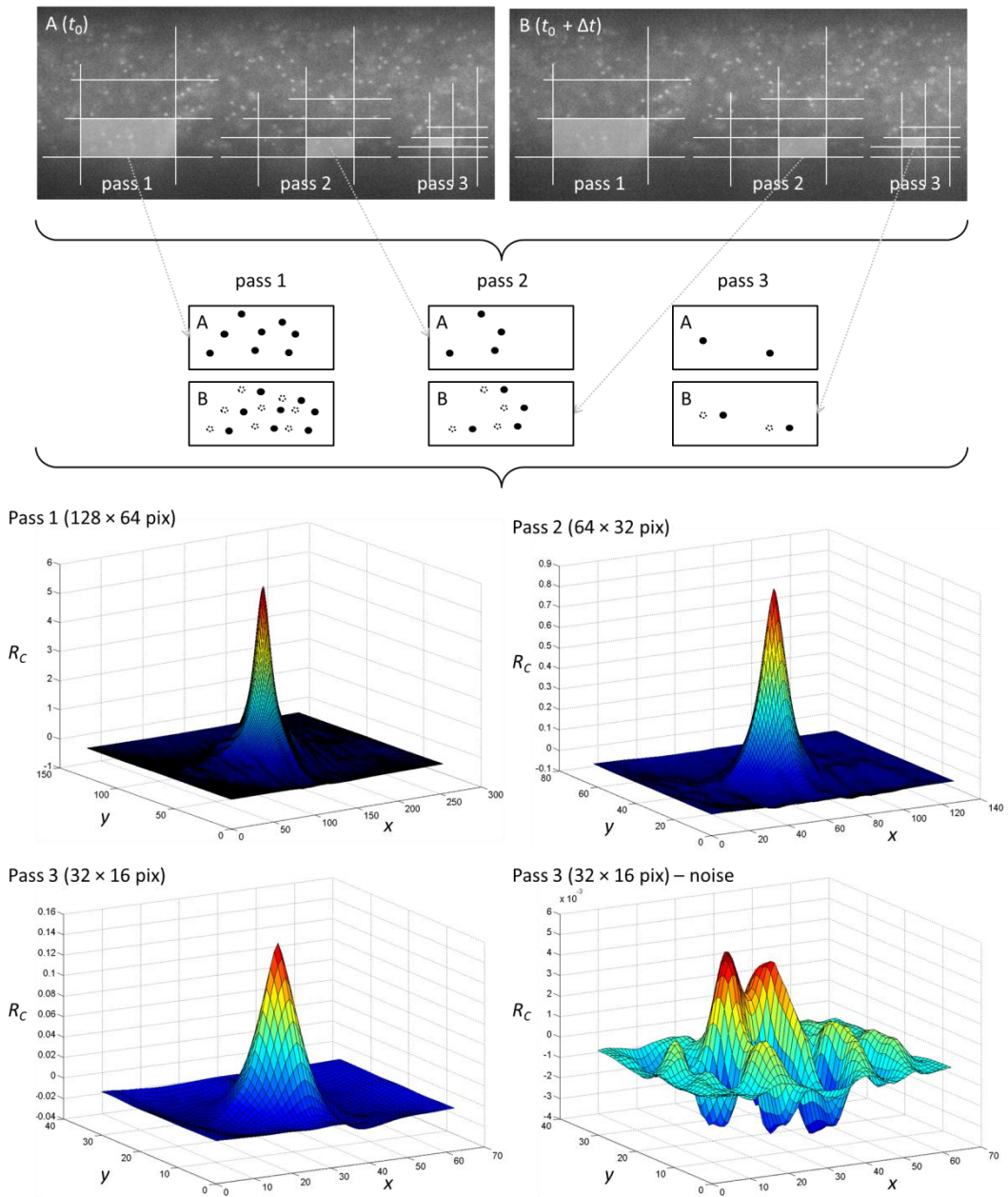


Figure 4.3 Multi-grid ensemble correlation is performed to infer the particle displacements from the particle patterns captured on the images. The interrogation functions correspond to the velocity vectors indicated with a rectangular in Figure 4.4, where the location for the invalid peak detection is (lower right interrogation function) shown in red.

Figure 4.3 shows some typical interrogation results. For each pass in the image interrogation procedure, the correlation functions R_C for a particular interrogation window are shown in Figure 4.3. The location of this IW, which is similar for all correlation functions, is indicated by the rectangle in the vector fields in Figure 4.4. Because the interrogation window size becomes smaller with each interrogation pass, the signal-to-noise ratio decreases. Still, there is a large displacement-correlation peak for the third pass. This is also expected from the high image densities as listed in Table 4.1. The large peak for the third pass is a clear indica-

tion that the effective image density is sufficiently large for an interrogation window size of only 32×16 pix, even though these interrogation peaks are calculated from particle patterns close to the lower wall of the channel, where the particle concentration is relatively low [14]. Comparison of the two interrogation functions presented in Figure 4.3 for the third pass verifies the reliability of the calculated velocity vectors close to the bubble surface of the microchannel. One of the interrogation functions corresponds to an interrogation window located outside the microfluidic channel, where no particles are present (indicated by the red rectangle in Figure 4.4). Consequently only noise is correlated in that IW, resulting in a very low value of R_C . This finally results in an invalid vector due to invalid peak detection.

4.6 Vector fields

From the displacement-correlation peaks in each interrogation window, with the known time delay Δt between image A and B, the vector field is obtained. The vector fields for all three passes are provided in Figure 4.4. The first pass vector field is superimposed on a raw μ PIV image, and for the third pass the velocity field is laid over a bright field reference image. The vector fields clearly show that for $y > 300$ pix the number of spurious vectors increases when the interrogation window size is decreased. However, all spurious vectors are located outside the microfluidic channel stem from detection of invalid correlation peaks. The fact that no spurious vectors are present inside the channels indicates a valid vector field is obtained, even for a IW size of 32×16 pix. The spatial resolution of the vector fields obtained in the third pass is then $5.2 \times 2.6 \times 3.1 \mu\text{m}^3$ with a vector-to-vector distance of $2.6 \mu\text{m}$ in the x -direction, and $1.3 \mu\text{m}$ in the y -direction.

The vector fields in Figure 4.4 show that the liquid flow close to the slip wall is following the bubble mattress pattern. This is a result of the large protrusion angle of $\vartheta_{PR} = 38 \pm 3^\circ$. For experiments with lower protrusion angles, the bubble pattern is less visible in the vector field. Nevertheless the vector fields in Figure 4.4 show that the presence of a bubble mattress does influence the hydrodynamics in the liquid channel.

The average liquid velocities u_{av} calculated from the vector fields are provided in Table 4.2, together with the dimensions and porosities of the three chips used in the experiments. These experimentally measured liquid velocities are considerably higher than the average velocity of 0.15 m/s (calculated from a set flow rate of $45 \mu\text{L}/\text{min}$ for a channel cross section of $50 \times 100 \mu\text{m}$). However, the flow in the channels of the device is 3-dimensional, i.e. there is also a velocity profile in the z -direction. When taking this third dimension into account, the maximum velocity in the middle of the channel is estimated at 0.3 m/s (following the Hagen-Poiseuille equation). This corresponds to the maximum velocities observed in the 2-dimensional vector fields, which are also measured in the middle of the channel. Correspondingly, these maximum velocities give an average liquid velocity of 0.2 m/s (for 2-dimensional parabolic velocity profiles $u_{max} = 1.5u_{av}$). This estimated average velocity is in reasonable agreement with the values given in Table 4.2.

However, the velocities given in Table 4.2 show that u_{av} for chip 2 is considerably larger than the average velocities measured for chip 1 and 3, even though the channel dimensions are similar for all three chips. The variation in the average liquid velocity can arise from various possible error sources.

Table 4.2 Measured geometry characteristics of the chip used in the μ PIV experiments.

Chip	ε [-]	W [-]	H [μm]		L_g [μm]		L_s [μm]		u_{av} [m/s]	
	Value	Value	Value	s_H	Value	s_{L_g}	Value	s_{L_s}	Value	$s_{u_{av}}$
1	0.38	1.64	48.7	0.4	18.9	0.2	30.9	0.4	0.182	0.004
2	0.54	0.85	51.4	0.4	21.6	0.2	18.3	0.2	0.204	0.004
3	0.72	0.38	51.5	0.4	21.6	0.2	8.25	0.15	0.187	0.003

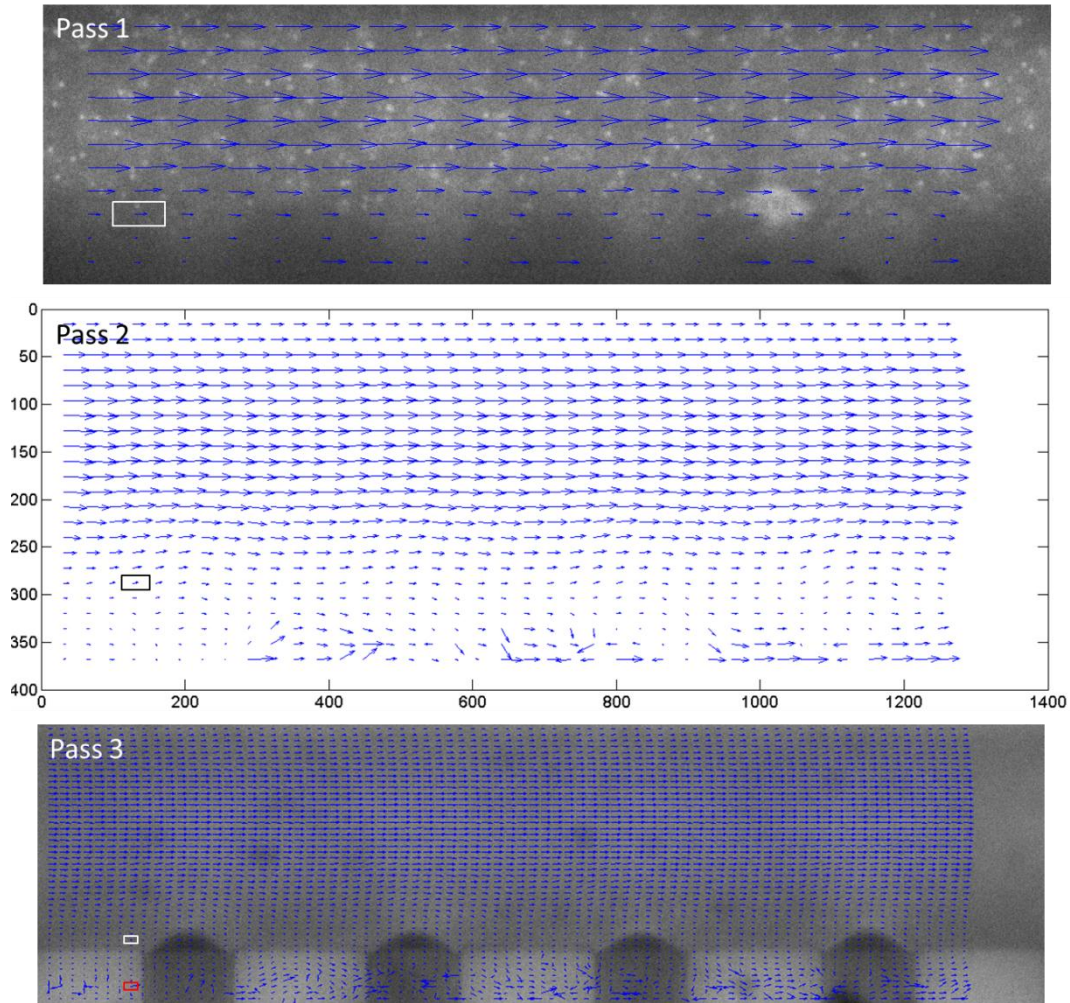


Figure 4.4 Typical vector fields obtained by ensemble correlation of 194 image pairs following the multigrid approach. In each interrogation pass, the size of the interrogation window is decreased, thereby increasing the spatial resolution of the velocity field. The vectors indicated with rectangles correspond to the interrogation functions in Figure 4.3.

The error in the velocity fields due to Brownian motion can be neglected, as in our μ PIV experiments the particle size is larger than $0.5 \mu\text{m}$ and our liquid velocity is in the order of 10^{-1} m/s [30]. However, there may be an error in the time delay Δt . First of all, there exists an uncertainty in the time difference between laser flash 1/2 and Q-switch 1/2, which is

about $0.2 \mu\text{s}$ for both $\Delta t_{QS1-LF1}$ and $\Delta t_{QS2-LF2}$. Second, significant jitter is observed in the triggering of the laser flashes and Q-switches. The error in Δt is therefore estimated to be $0.4 \mu\text{s}$, which is approximately 6% of the time delay.

From SEM-images of the wafers it is observed that the actual channel dimensions may deviate significantly from the specified dimensions. Furthermore, because of the high channel depth the etching is not perfect for chip 2 and 3. A deviating chip geometry can affect the ultimate cross-section of the channel, and consequently also the average liquid velocity.

Finally, in the calculation of u_{av} the confinement in cross-sectional area in the flow direction, as a result of bubbles protruding into the liquid, is not taken into account. In particular for large protrusion angles this may significantly change the effective cross-sectional area. For an angle of $\vartheta_{PR} = 55^\circ$ the bubble protrusion depth may go up to $5 \mu\text{m}$. This confinement also could result in a deviation from the expected flow rate by a few per cents.

By averaging the x -directional velocity u over the length of the device for all y -coordinates, an average $u_x(y)$ -profile is obtained. The $u_x(y)$ -profile for the pass 3 vector field in Figure 4.4 is plotted in Figure 4.5 (black circles), together with two $u_x(y)$ -profiles for a lower protrusion angle. All vectors outside the liquid channel or inside the bubble are deleted before calculation of these average velocity profiles. As expected, the largest deviations in the average velocity are observed at the right side of the maximum, which corresponds to the bubble mattress side. Especially near the bottom ($y = H = 48.7 \mu\text{m}$), the presence of the bubble mattress causes fluctuations in the liquid velocity (compare this with Figure 4.6B, where u is plotted for a given y as function of the x -position). The standard deviation values for the $u_x(y)$ -velocities, and the comparison of u_{av} with the other average liquid velocities in a set of experiments are utilised for assessing the validity of the vector fields.

All velocity profiles in Figure 4.5 show flattening of the profiles when approaching the bubble mattress wall at $y \approx 50 \mu\text{m}$. The amount of flattening is different however, as the profile for $\vartheta_{PR} = 38^\circ$ is flattening for $y > 40 \mu\text{m}$, while for $\vartheta_{PR} = 5^\circ$ flattening is observed for only the last 3 data points. And although this observation is somewhat affected by considering the average liquid velocity over both bubble and solid wall, it is in agreement with numerically obtained velocity profiles (the numerical profiles for chip 1 are provided in Figure C.5).

The first 7 data points of all $u(y)$ -velocity profiles above the bubble mattress wall are plotted in Figure 4.6 along the x -axis. These profiles show that the effect of local slip is visible only for the first 4 y -values, corresponding to a height of about $5 \mu\text{m}$ above the slip wall. And although this is visible for this particular experiment, for other experiments the influence of local slip is only visible for the first 2 y -values above the slip wall at $y = H$. That fact that the effect of local slip can only be observed very close to the slip wall is also observed by others (although there $(H - y) < 10 \mu\text{m}$ [14]). However, our experiments are performed with very high liquid flow rates, which may reduce the visibility of local slip in the velocity profiles even further. The flow profiles for larger y -values cannot be related anymore to local (slip) conditions, and are therefore a function of the global hydrodynamic conditions.

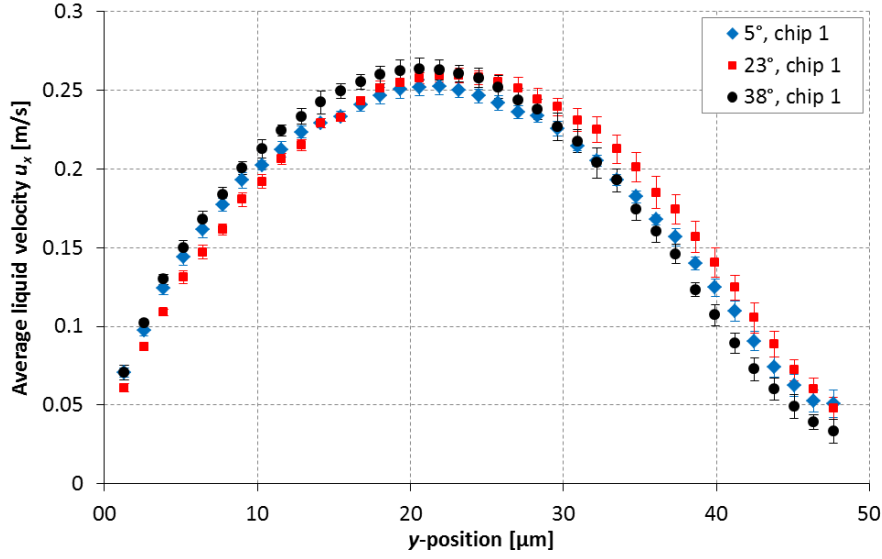


Figure 4.5 x -directional average velocity profiles for chip 1 for three different bubble protrusion angles ϑ_{PR} : $5 \pm 2^\circ$ (blue diamond); $23 \pm 5^\circ$ (red square); $38 \pm 3^\circ$ (black circle). The standard deviations in average velocity for each y in indicated by the error bars.

As a result, the experimentally obtained vector fields have not been used for assessing local slip conditions, but only for the extraction of average or effective slip lengths. For evaluation of local slip conditions, a further increase of the spatial resolution above the bubble mattress wall is necessary. This, in turn, will require adjustment of the experimental setup and conditions.

4.7 Slip length calculation

The obtained vector fields by μ PIV are used to investigate the dependency of slip on the protrusion angle. Calculation of the effective slip length from a vector field is performed by extrapolation of the velocity profile for each vector column (for each x -position) to obtain the distance b below the surface where the liquid velocity again equals zero, i.e. where $u = 0$. For each vector column, this velocity profile is obtained either by fitting a second-order polynomial through the $u(y)$ -velocities, or by fitting a straight line through the last 5 data points located $\sim 5 \mu\text{m}$ above the bubble surface.

The slip length extraction procedure is schematically shown in Figure 4.6. The first step is the deletion of all vectors that are located outside the channel, i.e. all vectors for which $y > H (= 303 \text{ pix})$ (Figure 4.6A). Because the positions of the side channels are known from the reference images, and the average bubble protrusion angle is obtained by measuring ϑ_{PR} for at least 8 side channels, the position of the lower surface y_H can be calculated for each x -position. This position is indicated by the black dots in Figure 4.6B. Because of the relatively high protrusion angle for this experiment ($\vartheta_{PR} = 38 \pm 3^\circ$), some of the velocity vectors at $y = 296 \text{ pix}$ and $y = 288 \text{ pix}$ correspond to a location inside the bubble, and thus are deleted from the vector field.

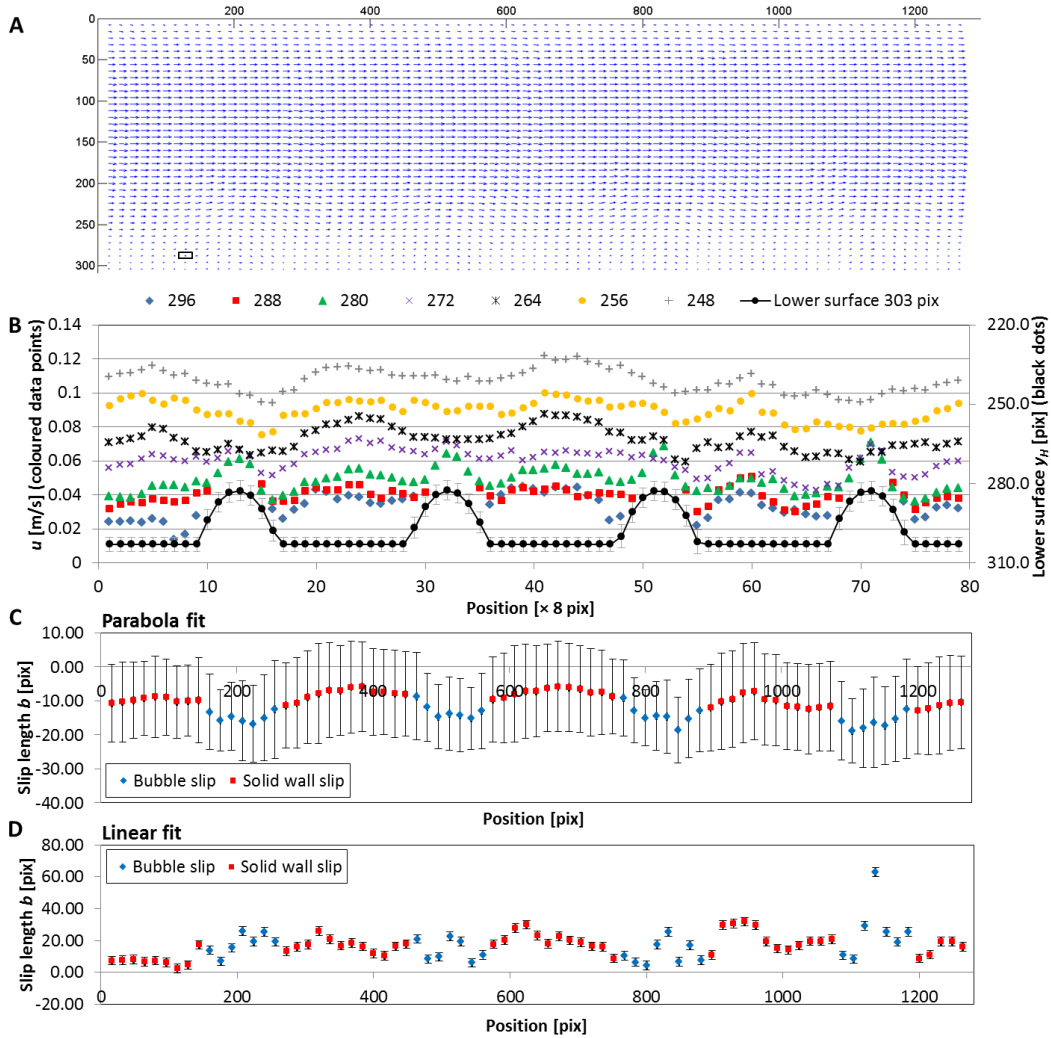


Figure 4.6 This figure illustrates the various steps required to extract the slip length from a vector field as shown in (A). First, the location of the slip wall is calculated for each x -position (B); $\vartheta_{PR} = 38 \pm 3^\circ$. Vectors that are located outside the channel or inside the bubble are deleted (B). The slip length is then calculated using two approaches: either a parabola is fitted to all velocity vectors in a column (C), or a straight line is fitted through the first 5 data points above the slip wall (D). It should be noted that for figure (B), the location coloured data points (the u -values) cannot be deduced from the right axis. The location of the data points is given in the legend above figure (B).

Subsequently an expression for (a part of) the velocity profile is obtained by fitting a first- or second-order polynomial through the experimentally determined $u(y)$ -profiles. Extrapolation of the tangent line at y_H for these fitted velocity profiles quantifies the slip length b at that x -position. This is described in more detail in section 2.3.3.5. The slip lengths as obtained following the parabola (using equation (42)) and linear approach (using equation (40)) are plotted as function of the x -position in respectively Figure 4.6C and Figure 4.6D.

The first difference that is observed when comparing the slip lengths in Figure 4.6C and Figure 4.6D is a difference between the values of b . Those obtained from the parabola approach are considerably smaller than the slip lengths calculated using the linear approach. For this experiment, the slip lengths in Figure 4.6C are even negative.

The large difference in b is a result of the calculation method. As is readily understood from the velocity profiles above the bubbles and above the wall (see also Figure C.5), calculating the slip length by using the parabola approach may result in an underestimation of the local slip length, as this does not always represent the tail of the velocity profiles properly, especially for low protrusion angles. Therefore this method is more suitable for straight channels with non-alternating slip conditions [46]. On the other hand, the slip length obtained using the linear approach may result in an overestimation of the effective slip length. The point at which the parabolic velocity profile is approximated by a straight line directly influences the obtained slip length (see also the numerically obtained slip lengths using the linear approach in Figure C.3). The closer this point is located to the slip wall, the better the returned slip length is in agreement with the actual slip length. But as the profiles in Figure 4.5 suggest, flattened velocity profiles likely limit the overestimation of the slip lengths obtained using the linear approach.

Second, the slip lengths in Figure 4.6C shows a difference between solid wall and bubble surface, whereas for the slip lengths in Figure 4.6D no distinction can be made between solid wall and bubble slip. However, the results for other experiments (not shown here) do not reveal any correlation between location (solid wall or bubble) and slip length value.

Finally, the slip length errors displayed in Figure 4.6C are much larger than the errors in Figure 4.6D (all errors being standard deviations resulting from the fitting of the velocity profiles). This also originates from the approach used to calculate the slip for each vector column. As revealed by the velocity profiles in Figure 4.5, a parabola may not describe the experimentally obtained profiles sufficiently well at all positions, especially near the lower slip wall. This results in relatively large errors in the coefficients (mainly in A and B) of the parabola (see equation (41)). The errors in these coefficients then propagate through equation (42) in the calculated slip length b . However, because of the large number of individual slip lengths (in total there are 79 vector columns), the standard deviation $s_{b,av}$ in the average slip length is much smaller ($s_{b,av} = s_{b_n}/\sqrt{n}$).

The standard deviations in the coefficients R and S describing the straight line through the last 5 data points of each vector column are considerably smaller, and hence also the slip lengths errors given in Figure 4.6D are very small.

The possible error in the determination of the slip wall location from a reference image is estimated to be 2 pix. Furthermore, the SEM-images of some silicon wafers reveal a slight tilting of the channel walls, while the precise z -position of the measurement plane is not known. The possible error resulting from this uncertainty is also estimated to be 2 pix. This adds up to a total possible error in the location of the slip wall location of 4 pix, which corresponds to 0.64 μm . This possible error is not averaged out when calculating the effective slip length. After converting this possible error in wall slip location into a statistical error, it turns out that for both approaches this error is the major source of uncertainty in the calculated effective slip length (as also in other studies after slip lengths using μPIV [10]).

4.8 Effective slip length

For all μPIV experiments with chip 1, 2, and 3, the dimensionless effective slip length is calculated using both the parabola and linear approach. The results are plotted in Figure 4.7 as function of the bubble protrusion angle ϑ_{PR} , together with the corresponding numerical dimensionless effective slip length profiles for each chip.

Irrespective of which method is used to extract the slip length from the vector fields, all experimental results show a decreasing effective slip length b with increasing protrusion angles. Closer inspection of the experimental results also reveals that this decrease is not linear, but that the dependency of slip on ϑ_{PR} is stronger for larger protrusion angles. This is in particular the case for chip 2 and 3.

In order to compare the experimental results with the predicted slip length profiles obtained from our numerical model, for all three chips the hydrodynamics are simulated for $1^\circ \leq \vartheta_{PR} \leq 67^\circ$ using the dimensions and flow rates as provided in Table 4.2. Slip length profiles have been determined using the fluid flux method/parabola approach, and the shear rate method/linear approach. The resulting profiles are also plotted in Figure 4.7.

Comparison of the numerically obtained slip length profiles with the experimental data points shows that they are in good qualitative agreement, for both parabola and linear approach. Also the numerical $b(\vartheta_{PR})$ -profiles show a non-linear decreasing slip length for $\vartheta_{PR} > 9^\circ$.

When comparing the experimental results with the numerical profiles for the linear approach, for chip 1 and 2 the slip lengths are also in quantitative agreement. The numerical profiles lie only slightly above the experimentally determined slip lengths. However, this is a result of the somewhat higher position above the slip wall at which the numerical profiles are computed. Where the experimentally determined slip lengths are found by fitting a straight line through the first 5 data points that are located at on average $5 \mu\text{m}$ above the lower wall H ($1.1 - 6.3 \mu\text{m}$ above $y = H$ for the solid wall, and at $2.4 - 8.6 \mu\text{m}$ above $y = H$ for the bubble surface), the numerical profiles are calculated at $7.5 \mu\text{m}$ above the slip wall.

Regarding the parabola approach, the experimentally found slip lengths are significantly smaller than the numerical $b(\vartheta_{PR})$ -profiles, in particular for chip 1 and 2. This suggests that close to the slip wall of the channel, the $u(y)$ -velocity profiles are not very well described by the fitted parabolas. This is supported by the observation that in Figure 4.7 the slip lengths obtained using the two approaches generally show opposite behaviour: in the imaginary line dividing the two data series the slip lengths for a certain angle form the mirror image of each other. In case a tail in the parabolic $u(y)$ -velocity profiles is present, this is likely well described by the linear approach. However, the fitted parabola is unable to represent this tail properly, by which b is underestimated. As a result, the two found slip lengths show opposite behaviour. The parabola approach gives a significant underestimation of the slip length.

Based on these considerations, the linear approach is regarded as the best method for calculating the slip length from experimentally obtained velocity profiles. Fitting a straight line through a number of data points close to the slip surface in order to calculate the slip length was also used by others [14].

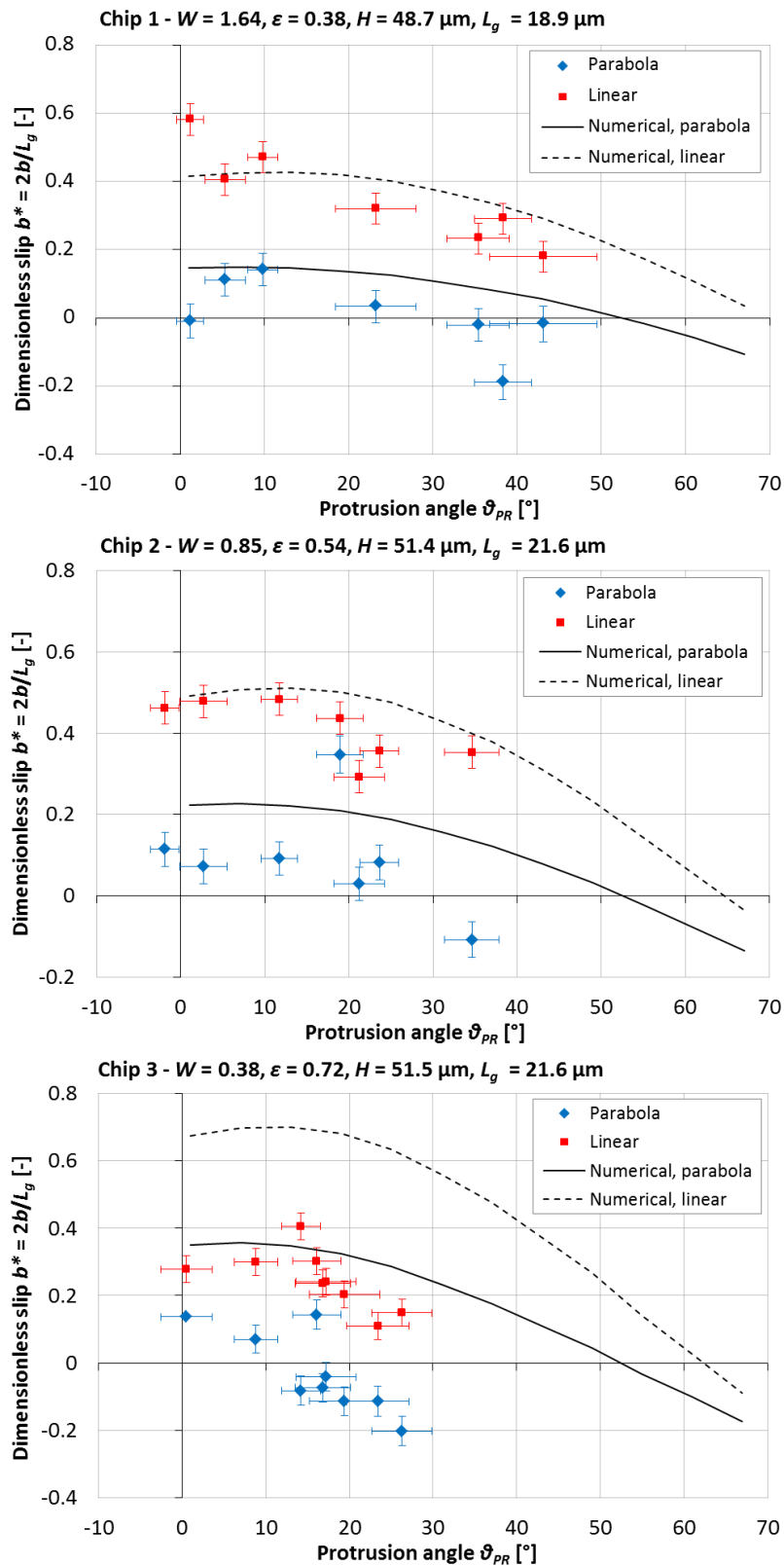


Figure 4.7 The experimentally determined dimensionless slip lengths $b^* = 2b/L_g$ are plotted as function of the protrusion angle ϑ_{PR} for all three chips. For comparison of the experimental results with the numerical model, for each chip also the computed slip length profiles are displayed.

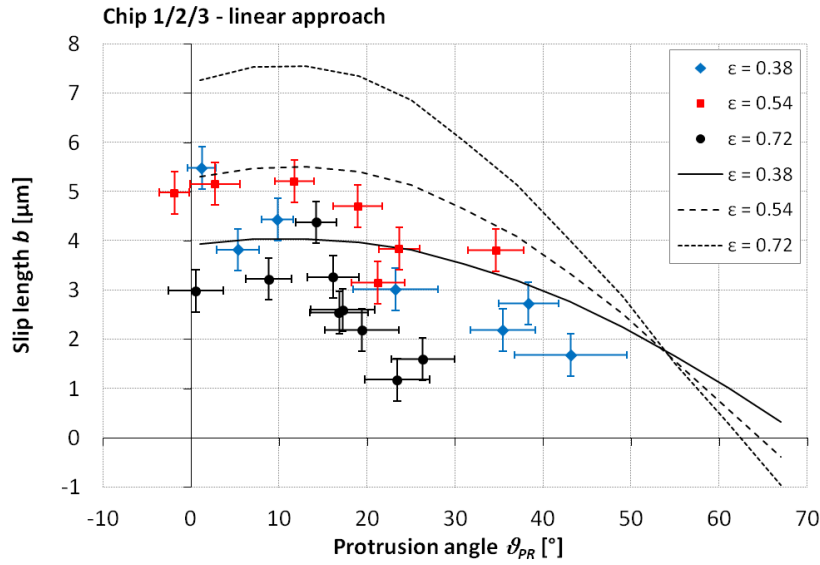


Figure 4.8 For all three chips, the experimentally found slip lengths b (in μm , calculated by the linear approach) are plotted as function of the protrusion angle ϑ_{PR} . To ease the comparison with the numerical model, also the simulated slip length profiles are given.

Compared to chip 1 and 2, the experimental results for chip 3 are in quantitative disagreement with the numerical profiles. At this point, it is unclear what is causing this dissimilarity. Possibly this is caused by an imperfect channel geometry, as observations during the experiments suggested close to the (silicon) bottom the side channel walls are not at right angles with the main channels as a result of deficient etching. Obviously this will affect both gas/liquid interface and liquid hydrodynamics, and consequently also the slip conditions in this device.

Finally, a comparison is made between the experimental results obtained for the three chips, characterised by different porosities, for the linear approach. In Figure 4.8 the non-dimensionalised slip lengths b (in μm) are plotted as function of the protrusion angle for all three chips, together with the numerically obtained profiles.

The experimental data for chip 1 and 2 (respectively $\varepsilon = 0.38$ and $\varepsilon = 0.54$) in Figure 4.8 shows a consistent dependency of the slip length on the porosity of the device. This is in agreement with the numerically calculated profiles, and with the analytical model of Davis and Lauga [4], both showing that the slip length is directly proportional to the porosity. Only for chip 3, with $\varepsilon = 0.72$, the experimental data is deviating. As discussed before, this is possibly caused by defective channel geometry.

For $-5^\circ < \vartheta_{PR} < 45^\circ$ the measured slip lengths are in the range of $1 - 6 \mu\text{m}$. For slip over (alternating) gas/liquid interfaces, the order of these values is in agreement with those found in other experimental studies [6, 14]. As expected, also the absolute slip lengths are slightly smaller than the slip lengths obtained numerically (about $1 \mu\text{m}$).

Inspection of the numerical slip length profiles in Figure 4.8 shows that they cross each other at $\vartheta_{PR} = 53^\circ$ where $b = 1.8 \mu\text{m}$. However, in the numerical data presented in Figure 3.3 (and also for the slip length profiles for the parabola approach given in Figure E.1), the point at which the profiles cross each other essentially corresponds the critical protrusion angle

where $b = 0$. This is also predicted by the analytical Davis-model given in equations (2) and (3). This suggests that the slip lengths indicated by the profiles in Figure 4.8 are $1.8 \mu\text{m}$ too long. Shifting the numerical $b(\vartheta_{PR})$ -profile $1.8 \mu\text{m}$ downwards would imply that (considering only chip 1 and 2) the linear approach gives an overprediction of the actual slip length of about $1 \mu\text{m}$.

In summary, all results from the μPIV experiments are in qualitative agreement with both numerically calculated slip length profiles, and with analytical models [4, 19]. They all show a decreasing slip length with increasing bubble protrusion angle. Furthermore, the experimental results prove that there exists a relationship between the amount of slip and the porosity of the device. For two of the three chips (chip 1 and 2), the experimentally found slip lengths are in quantitative agreement with numerical predictions.

5 CONCLUSIONS

The aim of this study was to investigate numerically and experimentally the influence of the gas/liquid interface geometry on both momentum and mass transport over bubble mattresses by quantification of effective slip length and mass transport enhancement.

In the numerical part of this study, both effective slip and mass transfer enhancement for fluid flow over a bubble mattress are considered. A computational fluid dynamics model has been developed that resembles the microfluidic bubble mattress devices used in the μ PIV experiments. Multiple simulations are performed to examine the influence of bubble mattress geometry, operating conditions, and chip dimensions on the slip and mass transfer characteristics. In each simulation, the slip length is determined for protrusion angles ϑ_{PR} ranging from -90° to 90° .

In order to quantify the effective slip length b for pressure-driven fluid flow, an analytical expression is derived that provides the effective slip length as function of the macroscopic fluid flux and pressure gradient over the bubble mattress. To the best of our knowledge, this type of equation has not been used before in other numerical studies.

The numerical results show that the effective slip length is a function of the gas/liquid interface geometry, i.e. the bubble protrusion angle, and the bubble mattress porosity. The effective slip is found to be independent of the bubble mattress length, liquid channel height, bubble unit length, and operating conditions.

The slip length profiles show a critical protrusion angle of $\vartheta_c = 55^\circ$. For $\vartheta_{PR} < \vartheta_c$ the slip length is positive, i.e. friction towards fluid flow is reduced. For $\vartheta_{PR} > \vartheta_c$ slip lengths are negative, i.e. increased friction towards fluid flow. This indicates that for $\vartheta_{PR} > \vartheta_c$ the additional resistance created by geometric obstruction of the liquid flow exceeds the reduction in friction by the full-slip bubble surface.

The slip length profiles for various surface porosities ε show that the effective slip length becomes larger with increasing porosity. For all porosities, the maximum slip length is obtained at a protrusion angle of 9° . All profiles cross each other at $\vartheta_{PR} = 57^\circ$, where b is slightly negative. Quantitatively, the simulated profiles are in good agreement with analytical models. Qualitatively, the simulated profiles are somewhat deviating from both analytical models and from profiles obtained in other studies. Our slip length profiles display a lower critical protrusion angle (55° versus 62° to 69°), and hence show a stronger dependency of the effective slip on protrusion angle. However, these differences are a result of the parabolic velocity profile in our simulations, where Couette flow is used in other studies.

Mass transfer enhancements are quantified in two ways in this study: by the solute flux enhancement E^ψ , and by the flow-averaged solute concentration enhancement E^c . By calculating the enhancement with respect to three different reference models, it is found that the rate of mass transfer in bubble mattresses is determined by the surface porosity, the gas/liquid interface geometry, and the slip conditions on the bubble surface.

For low protrusion angles (roughly $-20^\circ < \vartheta_{PR} < 20^\circ$), the concentration enhancement E^c mainly originates from the fluid slip at the bubble surface. For all other protrusion angles ($\vartheta_{PR} < -20^\circ$ and $\vartheta_{PR} > 20^\circ$), the enhancement is mainly a result of the position of the gas/liquid interface, i.e. the bubble protrusion angle. For $-20^\circ < \vartheta_{PR} < 55^\circ$, both outlet solute concentration and fluid flow are enhanced.

The solute flux enhancement E^ψ is a function of both slip conditions and solute concentration enhancement above the bubble surface. However, from the enhancement profiles it can be concluded that E^ψ is predominantly a result of the slip conditions, i.e. of the fluid flux over the bubble mattress. For low porosities ($\varepsilon \lesssim 0.4$) and $\vartheta_{PR} > 30^\circ$, E^ψ is strongly influenced by the position of the gas/liquid interface. For $-30^\circ < \vartheta_{PR} < 30^\circ$, the slip BC dominates. Irrespective of porosity, the enhancement for protrusion angles smaller than -30° is mainly determined by the bubble surface geometry. For high porosities ($\varepsilon \gtrsim 0.4$) and protrusion angles larger than -30° , the slippery gas/liquid interface is the major source of solute flux enhancement. The dominance of the slippery bubble surface becomes stronger with increasing porosity, as porosity scales directly with the effective slip and hence fluid flux over the bubble mattress. For the same applied pressure gradient (pumping power), solute flux enhancements up to 25% can be achieved.

To investigate the slip properties of bubble mattresses experimentally, micro-particle image velocimetry (μ PIV) is used. Vector fields are obtained with a spatial resolution of $5.2 \times 2.6 \times 3.1 \mu\text{m}^3$. From the various vector fields, the effective slip length is quantified by either by fitting a second-order polynomial through the velocity vectors, or by fitting a straight line through the data points at about $5 \mu\text{m}$ above the bubble surface. By comparison of experimental and numerical data, it is concluded that the linear approach is most suitable to calculate the slip from a vector field. Measured slip lengths are in the range of $1 - 6 \mu\text{m}$.

All experimentally obtained effective slip lengths are in qualitative agreement with numerically calculated slip length profiles, and with analytical models, showing a decreasing slip length with increasing bubble protrusion angle. Furthermore, the experimental results prove that there exists a relationship between the amount of slip and the porosity of the device. For two of the three chips used in the μ PIV experiments, the experimentally determined effective slip lengths are also in quantitative agreement with numerical predictions. To our knowledge, this is the first study presenting experimental data on the dependency of slip on the interface geometry for bubble mattresses.

This research is an important step in the development of stable, slippery interfaces. We demonstrated that stable bubble mattresses can be established in microfluidic chips. Contrary to superhydrophobic surfaces in the Cassie state where gas is entrapped within the roughness of the surface, our geometry provides direct control over the precise interface geometry of the slip surface. Moreover, by continuously monitoring the gas pressure, the slippery interface is intrinsically stable. Even for disturbed interfaces where liquid is entering the side channels, the effective slip is positive. These disturbed interfaces are readily re-established by changing the gas pressure. Main applications are in the field where drag reduction is important, like in microfluidics, and where improved heat and mass transport is beneficial for the process, e.g. in gas/liquid microreactors or in liquid cooling of microelectronic devices.

6 RECOMMENDATIONS

6.1 Numerical

Modelling of the experimental devices will become considerably more realistic when using 3-dimensional simulations. Because of the finite depth of the devices, the fluid flow dynamics in the middle of the channels are affected by wall effects. The 2-dimensional studies as performed here are therefore only an approximation of the real flow profile in the devices.

Making a 3-dimensional model will also be useful for investigating how slip and mass transfer changes with depth (the z -direction), as not only the flow field, but also the gas/liquid interface geometry varies along the z -axis. In particular knowledge on the precise shape of the bubble surface, which is shaped by the rectangular channel design in the devices, is valuable, as this can help to determine the location of the measurement plane in the experiments.

Further improvement of the numerical models can be made by incorporating the gas phase in the models. Gas flow in the bubbles does affect the amount of slip on the gas/liquid interface, meaning that the assumption of a perfectly slipping interface is not entirely valid. The ultimate gas flow profile depends on both the flow field of the liquid and the gas bubble/channel geometry. Therefore, also the length of the gas channels should be considered when modelling gas flow.

Finally, it is valuable to investigate whether for pressure-driven fluid flow over a bubble mattress, where very high shear rates are present at the bubble surface, various flow regimes are observed for which the pinning/depinning characteristics of the gas/liquid interface geometry are fundamentally different. The results can be compared to the various flow regimes as defined by Gao and Feng [5]. However, this requires the incorporation of moving interfaces and/or a moving mesh in the numerical models, since the assumption of a rigid bubble interface will not be valid anymore. Gaining more insight in the influence of high shear fluid flow on bubble mattress geometry can be a first step in setting up experiments to demonstrate the existence of various flow regimes.

6.2 Experimental

To improve the stability and homogeneity of a bubble mattress in a chip, an adjusted design of the microfluidic devices is proposed. Compared to the current geometry, this design is characterised by a lower number of side channels that are both smaller and shorter. Cylindrical side channels are even more desirable. The benefits of this adjusted chip design are manifold. First, the lower number of shorter side channels improves the hydrophobisation. This ameliorates the formation of a homogeneous hydrophobic layer on the silicon surface. Second, the smaller dimensions promote the formation of stable gas/liquid interfaces. Finally, the lower number of side channels improves the homogeneity of the protrusion angle over the length of the device, as the difference between gas and liquid pressure will be smaller in a shorter bubble mattress.

In the micro-particle image velocimetry (μ PIV) experiments performed for this study, particles with a diameter of $1\ \mu\text{m}$ are used. This size already exceeds the commonly used maximum diameter of 1% of the characteristic dimension, for example the channel height. As a result, only the overall flow profiles in the microfluidic channels have been determined. The resulting vector fields allow the calculation of effective slip lengths. However, for assessing local slip the resolution of the vector fields near the slip wall needs to be increased significantly. In fact, the determination of local slip is the first step to be taken in order to obtain a deeper understanding of the slip characteristics of bubble-mattress like geometries.

Therefore, it is highly desirable to decrease the particle size. Preliminary experiments with smaller particle sizes resulted in images on which the particles were either barely visible ($d_p = 0.5\ \mu\text{m}$), or not visible at all ($d_p \leq 0.3\ \mu\text{m}$). This is very likely a result of the short laser pulse duration, and of the fact that for particles with a diameter smaller than the laser light wavelength the intensity decreases extremely fast with particles size ($I \sim d_p^{4 \dots 6}$) [27]. Although these experiments can be repeated using an $100\times$ oil immersion lens instead of a $40\times$ air immersion lens, other equipment may be required, in particular a laser system with a longer pulse duration.

Using a piezoelectric objective-lens positioning system is recommended for a more accurate positioning of the focal place in the middle of the channel. After use in the μ PIV experiments, a SEM image can be taken from the devices in order to determine the exact chip geometry, in particular the depth of the channels. A known geometry reduces the uncertainty in the location of the channel walls. Furthermore, in combination with the calculation of the 3-dimensional shape of the bubble, a proper experimental method needs to be developed that enables a more precise determination of the bubble protrusion angle.

In this study, no systematic validation of the calculated vector fields is performed. Even though the vector fields appear to be free of invalid/spurious vectors in the region of interest, a validation procedure needs to be implemented that mathematically judges the validity of a vector. A commonly used method for outlier detection is the median test, in which the validity of a vector is judged by comparison of the vector with the median value of the eight nearest neighbour vectors [29, 47].

6.3 Future applications

The demonstrated formation of a stable bubble mattress in a chip is a first step in the development of stable, slippery interfaces. Such superhydrophobic interfaces have a highly potential applicability, as they have considerable impact on both surface- and bulk-transport phenomena [21]. Possible applications that make use of both the drag-reducing ability and the improved transport above these surfaces include devices with enhanced mixing under laminar, microscale flow conditions [48], the design of more efficient gas/liquid microreactors, and liquid cooling of microelectronic devices [10]. The reduced friction towards fluid flow is not only important in micro- and nanofluidics, but is also promising for large-scale flows. Slippery surfaces may be used to in marine applications to reduce fuel consumption, or in continuous flow algae growth systems to make the feeding of nutrients more efficient.

7 REFERENCES

1. Choi, C.H., K.J.A. Westin, and K.S. Breuer, *Apparent slip flows in hydrophilic and hydrophobic microchannels*. *Physics of Fluids*, 2003. **15**(10): p. 2897-2902.
2. Tretheway, D.C. and C.D. Meinhart, *Apparent fluid slip at hydrophobic microchannel walls*. *Physics of Fluids*, 2002. **14**(3): p. L9-L12.
3. Lauga, E., M. Brenner, and H. Stone, *Microfluidics: The No-Slip Boundary Condition*. *Springer Handbook of Experimental Fluid Mechanics*, C. Tropea, A.L. Yarin, and J.F. Foss, Editors. 2007, Springer Berlin Heidelberg. p. 1219-1240.
4. Davis, A.M.J. and E. Lauga, *Geometric transition in friction for flow over a bubble mattress*. *Physics of Fluids*, 2009. **21**(1).
5. Gao, P. and J.J. Feng, *Enhanced slip on a patterned substrate due to depinning of contact line*. *Physics of Fluids*, 2009. **21**(10).
6. Ou, J., B. Perot, and J.P. Rothstein, *Laminar drag reduction in microchannels using ultrahydrophobic surfaces*. *Physics of Fluids*, 2004. **16**(12): p. 4635-4643.
7. Choi, C.-H. and C.-J. Kim, *Large Slip of Aqueous Liquid Flow over a Nanoengineered Superhydrophobic Surface*. *Physical Review Letters*, 2006. **96**(6): p. 066001.
8. Chiara, N., R.E. Drew, B. Elmar, B. Hans-Jürgen, and S.J.C. Vincent, *Boundary slip in Newtonian liquids: a review of experimental studies*. *Reports on Progress in Physics*, 2005. **68**(12): p. 2859.
9. Hyväluoma, J. and J. Harting, *Slip Flow Over Structured Surfaces with Entrapped Microbubbles*. *Physical Review Letters*, 2008. **100**(24): p. 246001.
10. Rothstein, J.P., *Slip on Superhydrophobic Surfaces*. *Annual Review of Fluid Mechanics*, 2010. **42**(1): p. 89-109.
11. Bouzigues, C.I., L. Bocquet, E. Charlaix, C. Cottin-Bizonne, B. Cross, L. Joly, A. Steinberger, C. Ybert, and P. Tabeling, *Using surface force apparatus, diffusion and velocimetry to measure slip lengths*. *Philosophical Transactions of the Royal Society A: Mathematical, Physical and Engineering Sciences*, 2008. **366**(1869): p. 1455-1468.
12. Steinberger, A., C. Cottin-Bizonne, P. Kleimann, and E. Charlaix, *High friction on a bubble mattress*. *Nature Materials*, 2007. **6**(9): p. 665-668.
13. Ou, J. and J.P. Rothstein, *Direct velocity measurements of the flow past drag-reducing ultrahydrophobic surfaces*. *Physics of Fluids*, 2005. **17**(10): p. 103606-10.
14. Tsai, P.C., A.M. Peters, C. Pirat, M. Wessling, R.G.H. Lammertink, and D. Lohse, *Quantifying effective slip length over micropatterned hydrophobic surfaces*. *Physics of Fluids*, 2009. **21**(11).
15. Hyväluoma, J., C. Kunert, and J. Harting, *Simulations of slip flow on nanobubble-laden surfaces*. *Journal of Physics-Condensed Matter*, 2011. **23**(18): p. 11.
16. Lauga, E. and H.A. Stone, *Effective slip in pressure-driven Stokes flow*. *Journal of Fluid Mechanics*, 2003. **489**: p. 55-77.
17. Philip, J.R., *Flows satisfying mixed no-slip and no-shear conditions*. *Zeitschrift für Angewandte Mathematik und Physik (ZAMP)*, 1972. **23**(3): p. 353-372.
18. Schmieschek, S., A.V. Belyaev, J. Harting, and O.I. Vinogradova, *Tensorial slip of superhydrophobic channels*. *Physical Review E*, 2012. **85**(1): p. 016324.
19. Ng, C.-O. and C.Y. Wang, *Effective slip for Stokes flow over a surface patterned with two- or three-dimensional protrusions*. *Fluid Dynamics Research*, 2011. **43**(6): p. 065504.
20. Bocquet, L. and J.-L. Barrat, *Flow boundary conditions from nano- to micro-scales*. *Soft Matter*, 2007. **3**(6).

21. Bocquet, L. and E. Lauga, *A smooth future?* Nature Materials, 2011. **10**(5): p. 334-337.
22. Joly, L., C. Ybert, E. Trizac, and L. Bocquet, *Hydrodynamics within the Electric Double Layer on Slipping Surfaces*. Physical Review Letters, 2004. **93**(25): p. 257805.
23. Biswal, L., S. Som, and S. Chakraborty, *Thin film evaporation in microchannels with interfacial slip*. Microfluidics and Nanofluidics, 2011. **10**(1): p. 155-163.
24. Maynes, D., B.W. Webb, and J. Davies, *Thermal Transport in a Microchannel Exhibiting Ultrahydrophobic Microribs Maintained at Constant Temperature*. Journal of Heat Transfer, 2008. **130**(2): p. 022402.
25. De Gennes, P.-G., F. Brochard-Wyart, and D. Quéré, *Capillary and wetting phenomena: drops, bubbles, pearls, waves*2004, New York: Springer Science+Business Media.
26. Aran, H.C., *Porous ceramic and metallic microreactors. Tuning interfaces for multiphase processes*, in *Faculty of Science and Technology*2011, University of Twente: Enschede.
27. Lindken, R., M. Rossi, Gro, and J. Westerweel, *Micro-Particle Image Velocimetry ([small micro]PIV): Recent developments, applications, and guidelines*. Lab on a Chip, 2009. **9**(17): p. 2551-2567.
28. Wereley, S.T. and C.D. Meinhart, *Recent Advances in Micro-Particle Image Velocimetry*. Annual Review of Fluid Mechanics, 2010. **42**(1): p. 557-576.
29. Adrian, R.J. and J. Westerweel, *Particle Image Velocimetry*2011, New York: Cambridge University Press.
30. Raffel, M., C.E. Willert, S.T. Wereley, J. Kompenhans, C. Willert, and S. Wereley, *Micro-PIV*, in *Particle Image Velocimetry*2007, Springer Berlin Heidelberg. p. 241-258.
31. LaVision GmbH. *PIV Image Evaluation*. [cited 2012, 10 May]; Available from: http://www.piv.de/piv/measurement_principle/page_1.php.
32. Tu, J., G.H. Yeoh, and C. Liu, *Computational Fluid Dynamics: a practical approach*. 1st ed2008, Oxford: Butterworth-Heinemann.
33. Mulder, M., *Basic Principles of Membrane Technology*. 2nd ed2003, Dordrecht: Kluwer Academic Publishers.
34. Haase, A.S., *Effective slip length and mass transfer enhancement for fluid flow over a bubble mattress. A numerical study using COMSOL Multiphysics*.2012, Enschede: Faculty of Science and Technology, University of Twente.
35. Maboudian, R., W.R. Ashurst, and C. Carraro, *Self-assembled monolayers as anti-stiction coatings for MEMS: characteristics and recent developments*. Sensors and Actuators A: Physical, 2000. **82**(1-3): p. 219-223.
36. Geerken, M.J., T.S. van Zanten, R.G.H. Lammertink, Z. Borneman, W. Nijdam, C.J.M. van Rijn, and M. Wessling, *Chemical and Thermal Stability of Alkylsilane Based Coatings for Membrane Emulsification*. Advanced Engineering Materials, 2004. **6**(9): p. 749-754.
37. Srinivasan, U., M.R. Houston, R.T. Howe, and R. Maboudian, *Alkyltrichlorosilane-based self-assembled monolayer films for stiction reduction in silicon micromachines*. Microelectromechanical Systems, Journal of, 1998. **7**(2): p. 252-260.
38. Prakash, S., M.B. Karacor, and S. Banerjee, *Surface modification in microsystems and nanosystems*. Surface Science Reports, 2009. **64**(7): p. 233-254.
39. Stalder, A.F., G. Kulik, D. Sage, L. Barbieri, and P. Hoffmann, *A snake-based approach to accurate determination of both contact points and contact angles*. Colloids and Surfaces A: Physicochemical and Engineering Aspects, 2006. **286**(1-3): p. 92-103.
40. Abramoff, M.D., P.J. Magelhaes, and S.J. Ram, *Image Processing with ImageJ*. Biophotonics International, 2004. **11**(7): p. 36-42.
41. Deen, N., P. Willems, M. van Sint Annaland, J. Kuipers, R. Lammertink, A. Kemperman, M. Wessling, and W. van der Meer, *On image pre-processing for PIV of*

- single- and two-phase flows over reflecting objects*. Experiments in Fluids, 2010. **49**(2): p. 525-530.
42. Meunier, P. and T. Leweke, *Analysis and treatment of errors due to high velocity gradients in particle image velocimetry*. Experiments in Fluids, 2003. **35**(5): p. 408-421.
43. Pipe, C.J. and G.H. McKinley, *Microfluidic rheometry*. Mechanics Research Communications, 2009. **36**(1): p. 110-120.
44. Jähnisch, K., V. Hessel, H. Löwe, and M. Baerns, *Chemistry in Microstructured Reactors*. Angewandte Chemie International Edition, 2004. **43**(4): p. 406-446.
45. Devasenathipathy, S., J.G. Santiago, S.T. Wereley, C.D. Meinhart, and K. Takehara, *Particle imaging techniques for microfabricated fluidic systems*. Experiments in Fluids, 2003. **34**(4): p. 504-514.
46. Joseph, P. and P. Tabeling, *Direct measurement of the apparent slip length*. Physical Review E, 2005. **71**(3): p. 035303.
47. Westerweel, J. and F. Scarano, *Universal outlier detection for PIV data*. Experiments in Fluids, 2005. **39**(6): p. 1096-1100.
48. Ou, J., G.R. Moss, and J.P. Rothstein, *Enhanced mixing in laminar flows using ultrahydrophobic surfaces*. Physical Review E, 2007. **76**(1): p. 016304.

ACKNOWLEDGEMENTS

I would like to express my gratitude to a number of people. In the first place to Rob Lammer-tink for providing me this master assignment in the Soft matter, Fluidics and Interfaces group, and for the many discussions we had on all aspects of this study. Second, I am very thankful to Chao Sun for his useful advices on the μ PIV experiments, but also for his lessons and advices on the processing of the μ PIV data. Furthermore, I would like to thank Amy Tsai for her help with assessing the experimental results, and for her advices on the calculation of the slip lengths. I am also thankful to Claas-Willem Visser for all his assistance and advices regarding the μ PIV experiments, but even more for all his efforts in developing the correlation algorithm. Finally, I kindly thank Elif Karatay for her willingness to supervise me in this project, for her all efforts regarding chip fabrication, for introducing me in the experimental world of microfluidics, and for her help and support during this assignment, in particular in the last phase of this project.

A DERIVATION OF SLIP LENGTH EQUATIONS

A.1 From average shear rate

The slip length is defined as the point where the fluid velocity equals zero by extrapolation of the velocity profile with the velocity gradient at $y = 0$:

$$u_s = b \left. \frac{\partial u}{\partial y} \right|_{y=0} \quad (47)$$

The effective slip length can be calculated in two ways. For Couette flow (linear velocity profiles), this is commonly done by calculating the shear rate γ from the velocity profile.

In Couette flow the velocity gradient is approximately constant, and hence this equation can be used to calculate the effective slip length by computing the average shear rate γ and liquid velocity u at a certain line or boundary $y = h$ [1, 15]:

$$\gamma = \left. \frac{du}{dy} \right|_{y=h} \quad (48)$$

$$\left. \frac{du}{dy} \right|_{y=h} = \gamma = \frac{u|_{y=h}}{h + b} \quad (49)$$

$$b = \left. \frac{dy}{du} u \right|_{y=h} - h \quad (50)$$

A.2 From fluid flux

For pressure driven flow also a correlation between b and ϕ can be derived. The following assumptions are made:

- there is stationary flow;
- fluid flows only in the x -direction (i.e. no profile disturbance by the protruding bubbles);
- fluid flow is pressure driven;
- to obtain the effective slip length, slip flow is assumed everywhere at $y = 0$.

The resulting Navier-Stokes equation in the x -direction (see equation (15)) is the following:

$$\frac{\partial P}{\partial x} = \mu \frac{\partial^2 u}{\partial y^2} \quad (51)$$

Integration of above equation yields the following:

$$u(y) = \frac{1}{2\mu} \frac{\partial P}{\partial x} y^2 + C_1 y + C_2 \quad (52)$$

The following boundary conditions are valid in this situation:

$$u = 0 \text{ at } y = H \quad (53)$$

$$u = u_s = b \left. \frac{\partial u}{\partial y} \right|_{y=0} \text{ at } y = 0 \quad (54)$$

Using these boundary conditions, the following velocity profile is obtained:

$$u(y) = \frac{K}{2} y^2 - \left(\frac{KH}{2} + \frac{u_s}{H} \right) y + u_s \quad (55)$$

where

$$K = \frac{1}{\mu} \frac{\partial P}{\partial x} \quad (56)$$

For flow in the positive x -direction, the pressure gradient is negative. Now, for obtaining the relationship between b and fluid flux ϕ , integration of the velocity profile is required in order to find an expression for ϕ :

$$\phi = \frac{\iint_0^H u(y) dy dz}{\iint_0^H dy dz} = \frac{1}{H} \int_0^H \left[\frac{K}{2} y^2 - \left(\frac{KH}{2} + \frac{u_s}{H} \right) y + u_s \right] dy = -\frac{KH^2}{2} + \frac{u_s}{2} \quad (57)$$

To eliminate u_s in above equation, the definition of slip length as given in equation (1) is used. For this, the derivative of the velocity profile is required:

$$\frac{\partial u}{\partial y} = Ky - \frac{KH}{2} - \frac{u_s}{H} \quad (58)$$

Now an expression for the slip velocity u_s is found which contains the slip length b :

$$u_s = b \left. \frac{\partial u}{\partial y} \right|_{y=0} = -b \left(\frac{KH}{2} + \frac{u_s}{H} \right) \quad (59)$$

Rewriting gives

$$u_s = -\frac{bKH}{2} \left(1 + \frac{b}{H}\right)^{-1} \quad (60)$$

Substitution of equation (60) in equation (57) and subsequent rearranging gives the following expression for b as function of fluid flux, pressure gradient, and channel height:

$$b = \frac{-\phi - \frac{H^2}{12\mu} \frac{\partial P}{\partial x}}{\frac{\phi}{H} + \frac{H}{3\mu} \frac{\partial P}{\partial x}} \quad (61)$$

Obviously, equation (61) gives the effective slip length, as no account is made for the regions where the no-slip boundary condition is valid, namely on the solid walls between the bubbles. When this is taken into consideration by using the porosity $\varepsilon = L_g/L$ (then at $y = 0$, $u = \varepsilon u_s$), the following expression can be derived in order to calculate the bubble or porosity-corrected slip length b_b :

$$b_b = \frac{1 - \phi - \frac{H^2}{12\mu} \frac{\partial P}{\partial x}}{\varepsilon \left(\frac{\phi}{H} + \frac{H}{3\mu} \frac{\partial P}{\partial x} \right)} \quad (62)$$

For a parabolic velocity profile between two flat plates with on both sides a no-slip BC, it is easily derived that (starting from equation (55) with $u_s = 0$)

$$\frac{\partial P}{\partial x} = \frac{12\mu u_{av}}{H^2} \quad (63)$$

B COMSOL MODEL

B.1 Parameterisation of bubble surface

To facilitate evaluation of the effective slip length and mass transfer enhancement for different protrusion angles ϑ_{PR} , the model geometry is parameterised. This is based on the drawing provided in Figure B.1.

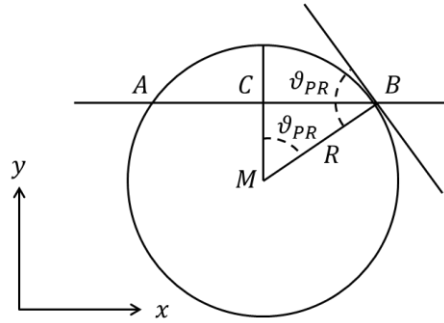


Figure B.1 Schematic drawing of a bubble surface (the circle) to parameterise the arc AB as function of the length AB and the angle ϑ_{PR} .

Without further clarification, the derivation of expressions describing the arc AB is shown below ($x_A = 0, y_C = 0$). Note that (x_M, y_M) and R are fixed for a given ϑ_{PR} .

$$\text{length}(AB) = 2 \times \text{length}(BC) = L_b \quad (64)$$

$$R = \frac{L_b}{2 \sin \vartheta_{PR}} \quad (65)$$

$$x_M = \frac{L_b}{2} \quad (66)$$

$$y_M = -\frac{L_b \cos \vartheta_{PR}}{2 \sin \vartheta_{PR}} \quad (67)$$

The arc AB is described by the following equations, where the domain of these functions (in radians) is defined by the protrusion angle under investigation.

$$x = x_M + R \cos s \quad (68)$$

$$y = y_M + R \sin s \quad (69)$$

$$s = \left[\frac{\pi}{2} - \vartheta_{PR}, \frac{\pi}{2} + \vartheta_{PR} \right] \quad (70)$$

Obviously, in the models for evaluating fluid flow over ‘negative’ bubbles, equations (67) and (69) need to be multiplied by -1 .

B.2 Entrance/outlet domain length

For parabolic Poiseuille flow, the length required for obtaining a developed velocity profile can be approximated by the following correlation¹:

$$\frac{L_{ent}}{d_h} \approx 0.06Re \quad (71)$$

For an entrance length of $2L$, and with $d_h = 100 \mu\text{m}$, the maximum Reynolds number is $Re = 13$. In our simulations however, the maximum Reynolds number is approximately $Re = 1$, so the flow will be developed after a length of $2L$.

¹ The Engineering Toolbox, *Entrance Length and Developed Flow*. [cited 2012, 8 March]; Available from: http://www.engineeringtoolbox.com/entrance-length-flow-d_615.html.

C SUPPORTING NUMERICAL DATA

C.1 Meshing

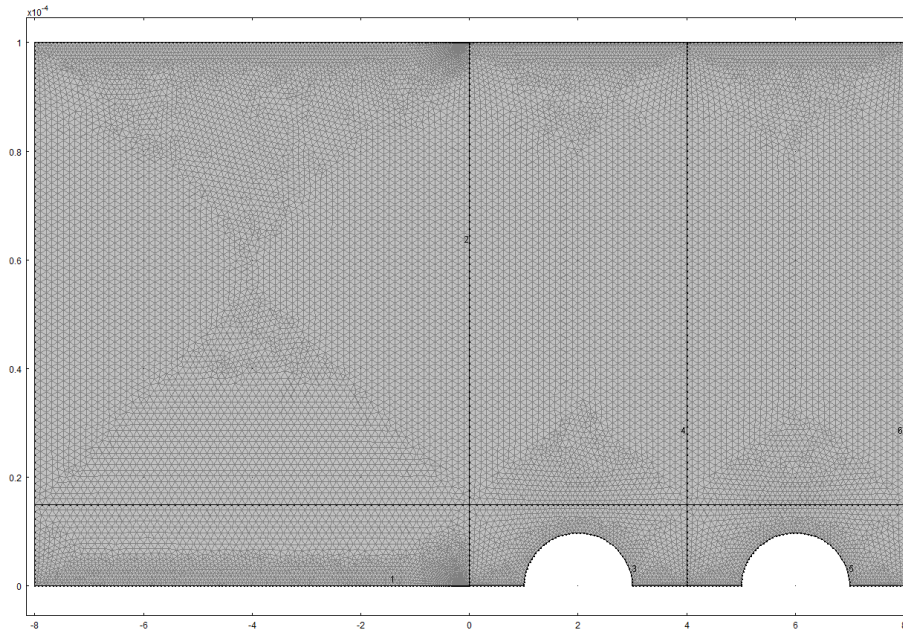


Figure C.1 Mesh for non-periodic pressure-driven flow, standard specifications (see Table 2.1). The mesh size is calibrated for fluid dynamics, with global element size of *extra fine*. Close to all upper and lower boundaries, the element size is set to *extremely fine*.

C.2 Model development

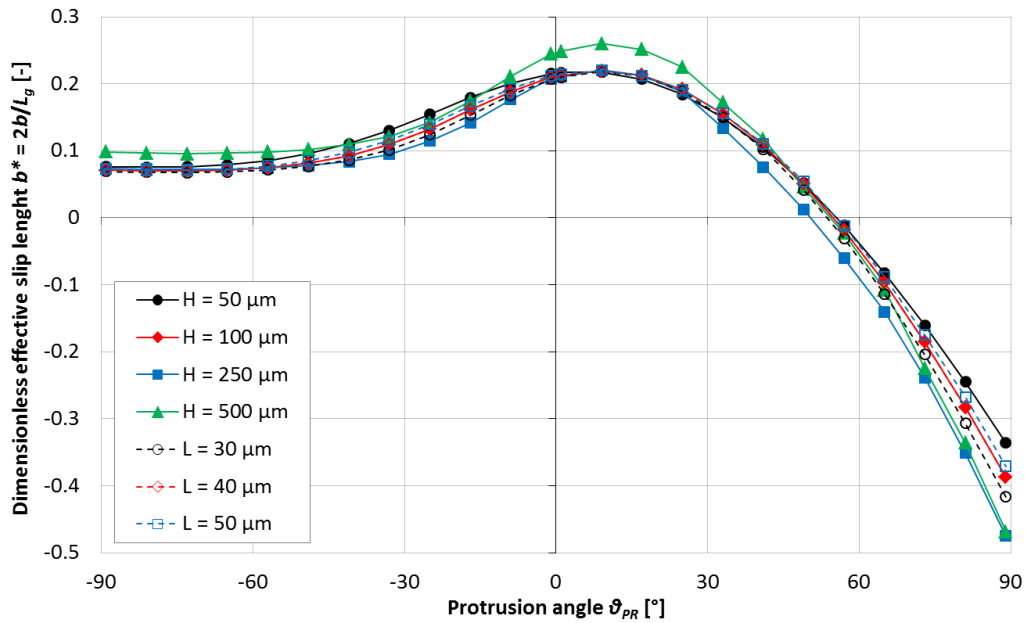


Figure C.2 Effective slip length as calculated from the fluid flux ϕ for different channel heights H and bubble unit lengths L .

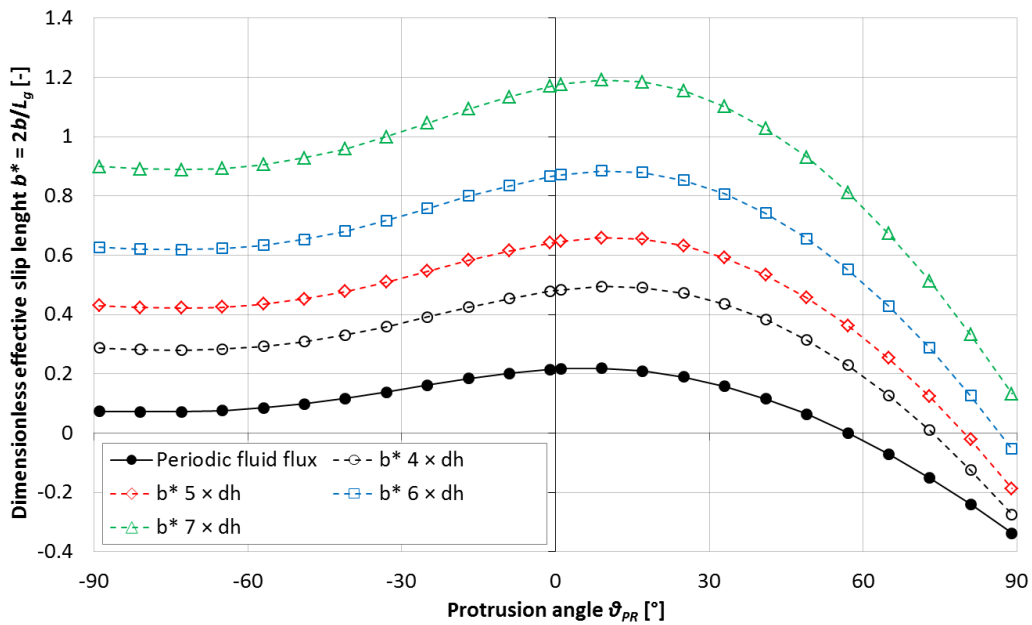


Figure C.3 Periodic pressure-driven fluid flow model: effective slip lengths as calculated from the shear rate at different heights.

C.3 Concentration and velocity profiles

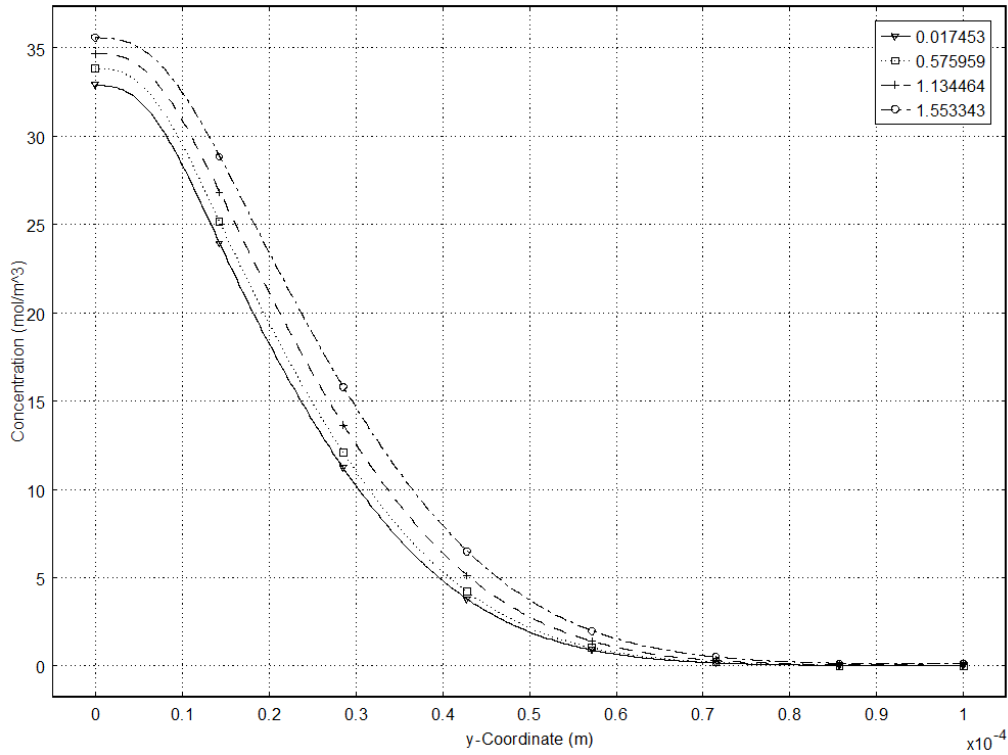


Figure C.4 Concentration profiles for non-periodic pressure-driven flow, $\Delta P/\Delta x = -1800$ Pa/m, at bubble unit boundary 17 (see also Figure 3.2) ($\nabla = 1^\circ$; $\square = 33^\circ$; $+= 65^\circ$; $\circ = 89^\circ$).

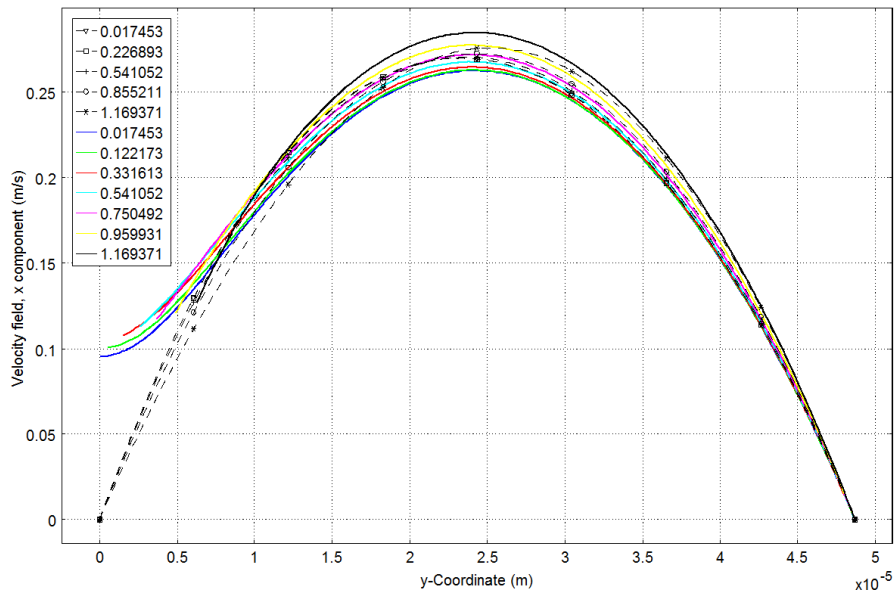


Figure C.5 $u(y)$ -velocity profiles for a number of protrusion angles (in radians) above the middle of the bubble (coloured lines), and between the bubbles (dashed black lines).

C.4 Surface porosity

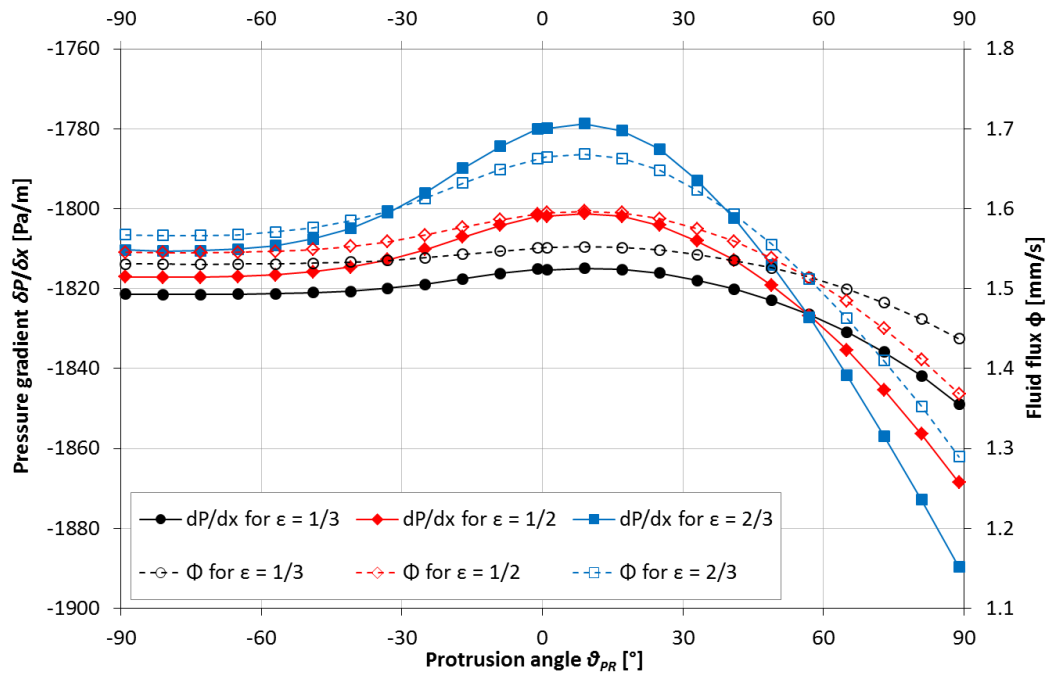


Figure C.6 Average pressure gradient over the middle 11 bubble units (solid lines) and the fluid flux (dashed lines) as function of the protrusion angle for 3 different porosities.

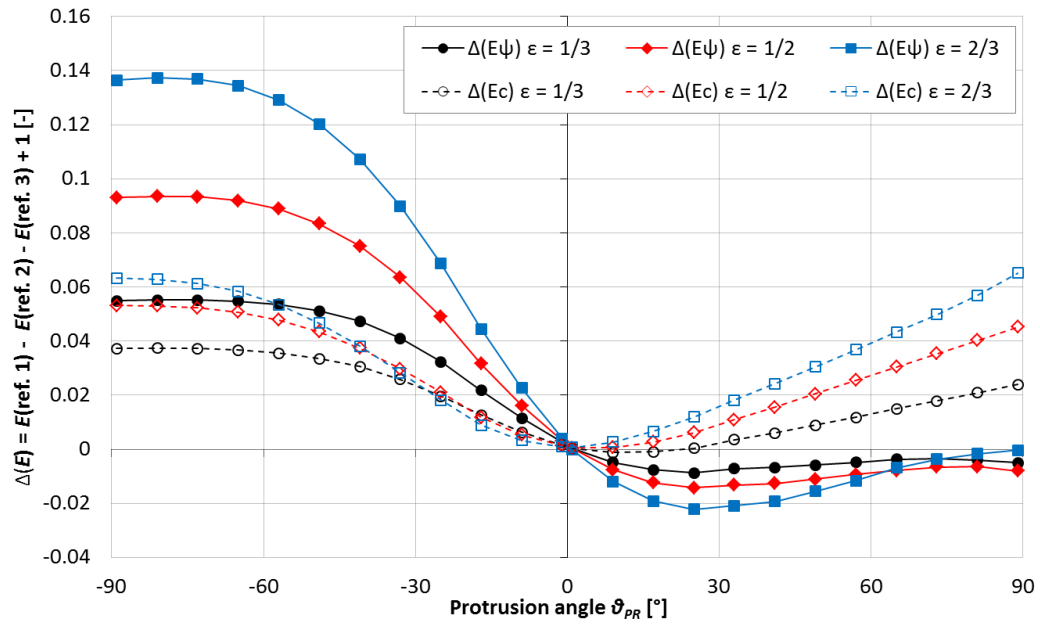


Figure C.7 The mass transfer enhancement profiles are calculated according to the following equation: $\Delta(E) = E(\text{ref. 1}) - E(\text{ref. 2}) - E(\text{ref. 3}) + 1$.

D ERROR ANALYSIS

For calculating the uncertainty in a quantity u , where $u = f(x_1, x_2, x_3, \dots)$, the methods of moments can be used². The most commonly used form for uncertainty analysis is the first-order second-moment method, in which the spread (the second moment) is estimated based on a first-order approximation of f :

$$s_u^2 = \sum_{j=1}^m \left(s_{x_j} \frac{\partial u}{\partial x_j} \right)^2 + 2 \sum_{j=1}^m \sum_{k=j+1}^m r_{x_j x_k} \left(s_{x_j} \frac{\partial u}{\partial x_j} \right) \left(s_{x_k} \frac{\partial u}{\partial x_k} \right) \quad (72)$$

Here, s_u is the standard error of u . In case the variables x_1, x_2, x_3 , etc. are independent of each other, i.e. uncorrelated, the method of moments simplifies to the Gaussian propagation error rule³:

$$s_u^2 = s_{x_1}^2 \left(\frac{\partial u}{\partial x_1} \right)^2 + s_{x_2}^2 \left(\frac{\partial u}{\partial x_2} \right)^2 + s_{x_3}^2 \left(\frac{\partial u}{\partial x_3} \right)^2 + \dots \quad (73)$$

This Gaussian error propagation rule is utilised for calculating

- the error in the location of the lower slip wall s_{y_H} , where the location of the lower wall can be written as $y_H = f(H, R, \vartheta_{PR}, x_H)$ (based on equation (37));
- the error in the slip length s_{b_n} as obtained by the parabola approach (equation (42)), where the slip length can be written $b_n = f(A, B, C, y_H, H)$. For a parabola, it is said that the coefficients A, B , and C are uncorrelated with each other⁴. As such, the Gaussian propagation can be used for calculating the error in b_n .

However, when using the linear approach for calculating the slip length (equation (40)), the coefficients R and S are correlated²: $r_{RS} = -\sqrt{r_{RS}^2}$. Then, according to equation (72), the error s_{b_n} in the slip length b_n can be calculated as follows:

$$s_b^2 = s_R^2 \left(\frac{\partial b_n}{\partial R} \right)^2 + s_S^2 \left(\frac{\partial b_n}{\partial S} \right)^2 + s_H^2 \left(\frac{\partial b_n}{\partial H} \right)^2 + 2r_{RS} \left(s_R \frac{\partial b_n}{\partial R} \right) \left(s_S \frac{\partial b_n}{\partial S} \right) \quad (74)$$

² Kirchner, J., *Data Analysis Toolkit #5: Uncertainty Analysis and Error Propagation*. [cited 2012, 14 May]; Available from: http://seismo.berkeley.edu/~kirchner/eps_120/EPSToolkits.htm.

³ Derissen, J.L., P.H. van Roon, P.S. Peijzel, and R.J. Baars, *Foutenleer. Omgaan met onderzoeksgegevens in de chemie*. 2008, Utrecht: Faculteit Bètawetenschappen, Departement Scheikunde, Universiteit Utrecht.

⁴ Freeman, W.H. and Company, *Covariance and correlation*. [cited 2012, 14 May]; Available from: <http://www.ncbi.nlm.nih.gov/books/NBK21288/>.

Then, the error in the average or effective slip length $b_{n,av}$ from all local slip lengths b_n for each vector column is given by the following expression:

$$s_{b,av} = \frac{1}{n} [s_{b_1}^2 + s_{b_2}^2 + \dots + s_{b_n}^2]^{1/2} \quad (75)$$

However, in this error $s_{b,av}$ the possible error in the position of the wall ΔH is not included, as this possible error is not averaged out when calculating the effective slip length. For converting a possible error ΔH into a standard error s_H , the following approach is utilised⁵:

$$s_H = \frac{2}{3} \Delta H \quad (76)$$

Now, the error s_b in the effective slip length b becomes:

$$s_b = [s_{b,av}^2 + s_H^2]^{1/2} \quad (77)$$

⁵ Meulen, J. van der, B.M. Tel, and P.P. Veugelers, *Algemene practicumhandleiding*. 2006, Enschede: Faculteit der Technische Natuurwetenschappen, Universiteit Twente.

E SUPPORTING EXPERIMENTAL DATA

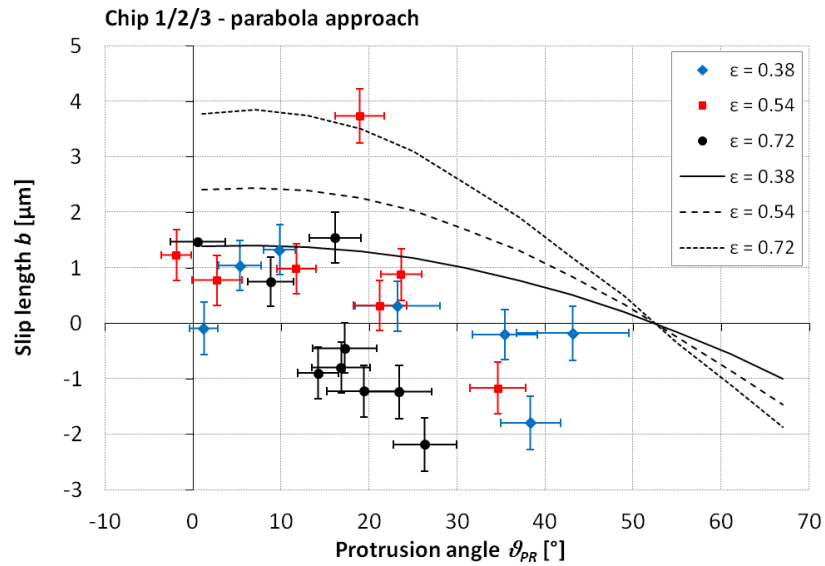


Figure E.1 For all three chips, the experimentally found slip lengths b (in μm , using the parabola approach) are plotted as function of the protrusion angle ϑ_{PR} . To ease the comparison with the numerical model, also the simulated slip length profiles are given.